Optic Nerve Characterization using Magnetic Resonance Imaging: The Search for Biomarkers

By

Robert Louis Harrigan

Dissertation

Submitted to the Faculty of the

Graduate School of Vanderbilt University

in partial fulfillment of the requirements

for the degree of

DOCTOR OF PHILOSOPHY

in

Electrical Engineering

May, 2017

Nashville, Tennessee

Approved:

Bennett A. Landman, Ph.D.

Seth A. Smith, Ph.D.

Richard Alan Peters, Ph.D.

David J. Calkins, Ph.D.

Jack H. Noble, Ph.D

Acknowledgments

My time as a graduate student has been an adventure and I am grateful for all of the opportunities which have been afforded me and for all the people who have helped to make this possible. Most of all I am grateful to my wife Alisha, her patience and support has been unwavering. Without her loving support I would not be where I am today. I would like to thank my beautiful daughter Natalie for teaching me things I cannot learn from any book or journal article. I am grateful for my son, Canaan, as he brings joy to every day and he inspires me to be a better man. I am grateful for both of my advisors for being so flexible and allowing me to spend time with my family and their understanding of my commitment to fatherhood.

I want to thank my parents for supporting me through all my many years of school and endeavors. They have always believed in me and supported me, even if I do flush a tennis ball down the toilet. I would like to thank Penny and Lee for all that they do for Alisha and I, both of you are a tremendous help and none of this would be possible without you. Grandma Langevin and Grandma Harrigan thank you for your love and support. Popop you will always be with us in spirit, may you rest in peace. Nanny and Pepaw, thank you for your constant love and generous spirit.

I am grateful for all of the people at Vanderbilt who have helped to guide my journey and teach me. I would like to thank both of my advisors, Seth Smith and Bennett Landman, thank you for your guidance and thoughtful insight, without the two of you this would never have been possible. The two of you have showed me how researchers can work together, have fun and do good science. I am honored to be a member of the MASI lab and share my time with so many great members. Andrew Plassard – Thank you for always pushing me to be better and for being a great friend. Steve Damon – Thanks for all the hard work you do behind the scenes, none of the research in our lab would be possible without you. Zhoubing Xu – Thank you for all of your help in writing and your design expertise. I would like to thank everyone in VUIIS and especially the Neuroimaging Outside the Brain group for all of the help that was provided every week. Alex Smith – for guiding me to the promised land of MT. Siddharama Pawate –

Your dedication to research is inspiring, thank you for all that you for our work and the amazing knowledge you provide. Louise Mawn – Thanks for all that you do to help move our work in the right direction. Francesca Bagnato – Your clinical perspectives are immensely helpful and your commitment of valuable time to bettering our work is tremendous. For all the other members of the MASI lab, Yuankai, Cam, Prasanna, Gaile, Shikha, Vish, Shunxing, Josh, Justin and all of the undergraduates, Gabriella, Yifu, Lizzy, Xia, and Natalie I am grateful and thank you for your hard work.

Table of Contents

Page

List of Tables

List of Figure

Chapter I. Imaging of the Optic Nerve

1. Human Visual System Anatomy

The human visual system is an elegant processing pipeline with tremendous capabilities which are invaluable in our everyday lives. Our visual system has the ability to concurrently process color, shape, motion and spatial information in meaningful ways which is necessary for the execution of everyday tasks. This processing involves multiple steps at varying degrees of complexity operating on larger and larger spatial fields throughout the brain. However, all of the visual information originates as light entering the eye globe where it is focused onto the retina into an image and is transmitted through the optic nerve (ON) and lateral geniculate nucleus to primary visual cortex. The ON serves as the single conduit for communicating light from the outside world throughout the brain for processing and response.

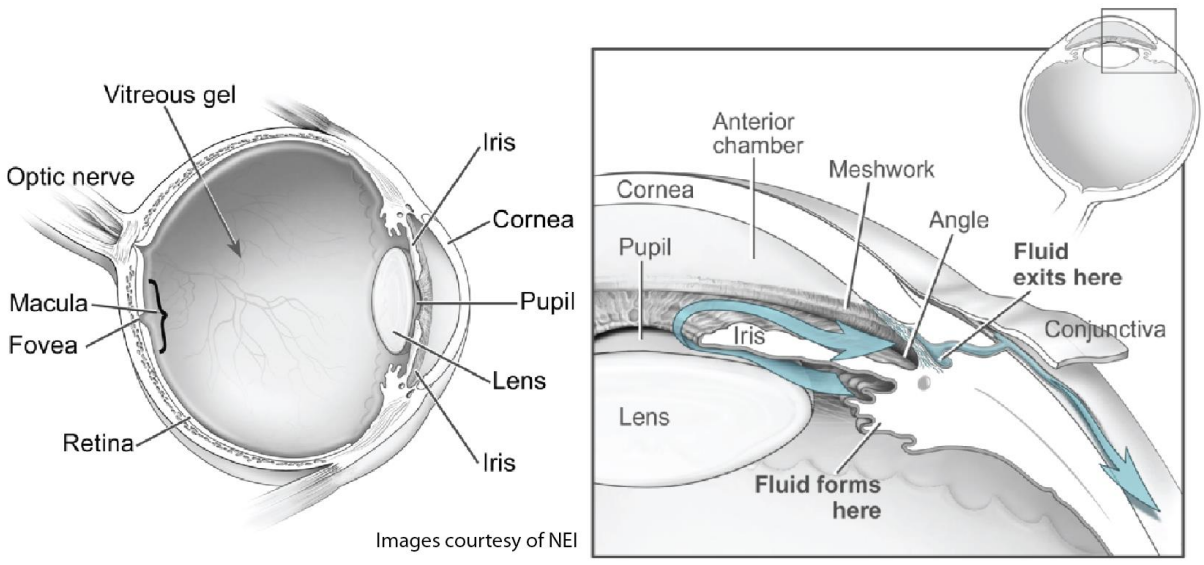

Figure I.1. Eye globe anatomy (left) illustrating the path of light through the cornea, lens and vitreous gel onto the retina. Right image is a close up of the mechanics of glaucomatous increased intraocular pressure. Fluid exits the eye globe and we see where fluid buildup can decrease outflow which raises intraocular pressure.

1.1. Eye globes

The eye globes serve to focus incoming light such that it presents a focused image on the retina. The eye has two focusing apparatus, the cornea and the lens. The cornea creates the interface between the air and the anterior chamber filled with aqueous humor. The light then passes through the lens which, through small muscle contractions, can change shape to adjust the focal length of the system. The lens is controlled by the ciliary muscle which is attached to the lens by the zonule fibers. The light next passes through the vitreous humor where it can be recorded by the retina (Figure I.1 left). The retina consists of two types of photoreceptors, rods and cones, which are sensitive to different light intensities and wavelengths. Cones are used for color vision and there are three types of cones which are sensitive to long (red), medium (green) and short (blue) wavelength light (Figure I.2 left). Cones are densely packed near the center of the visual field or fovea and are used for daytime vision. Rods are more sensitive to incoming light and have a spectral response profile centered between the medium and short cones, or blue and green light (Figure I.1 left). Rods are used mostly for night vision and are distributed further away

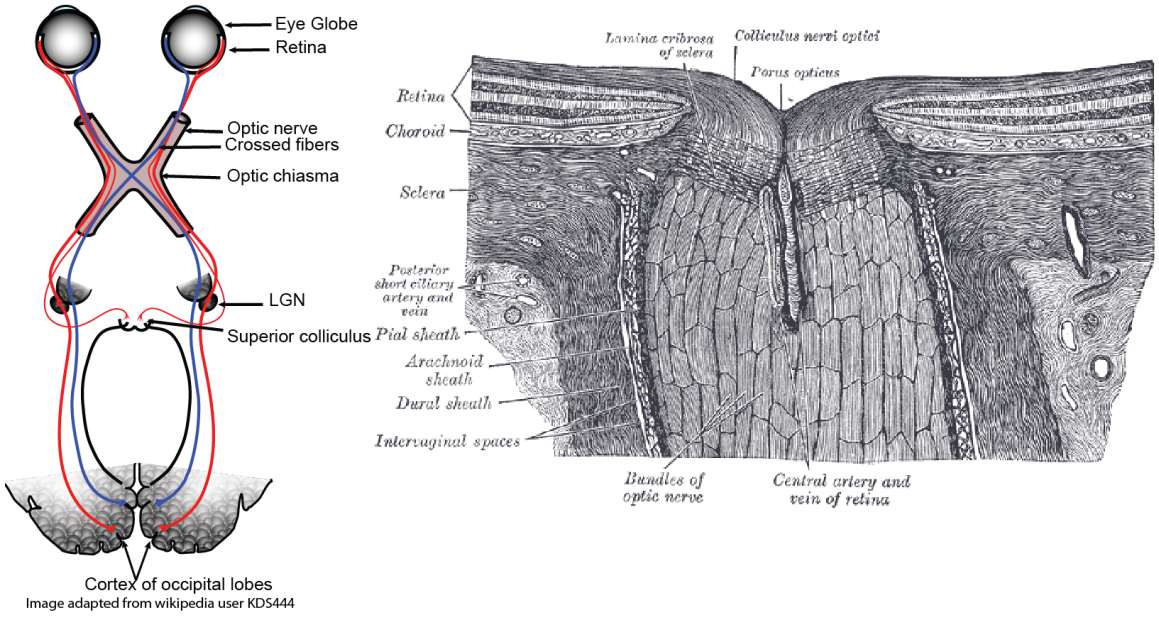

Figure I.2. Visual pathway anatomy (left) illustrating the decussation of fibers at the optic chiasm such that each side of visual cortex receives information from one visual hemi-field. An illustration of the meningeal layers of the ON (right).

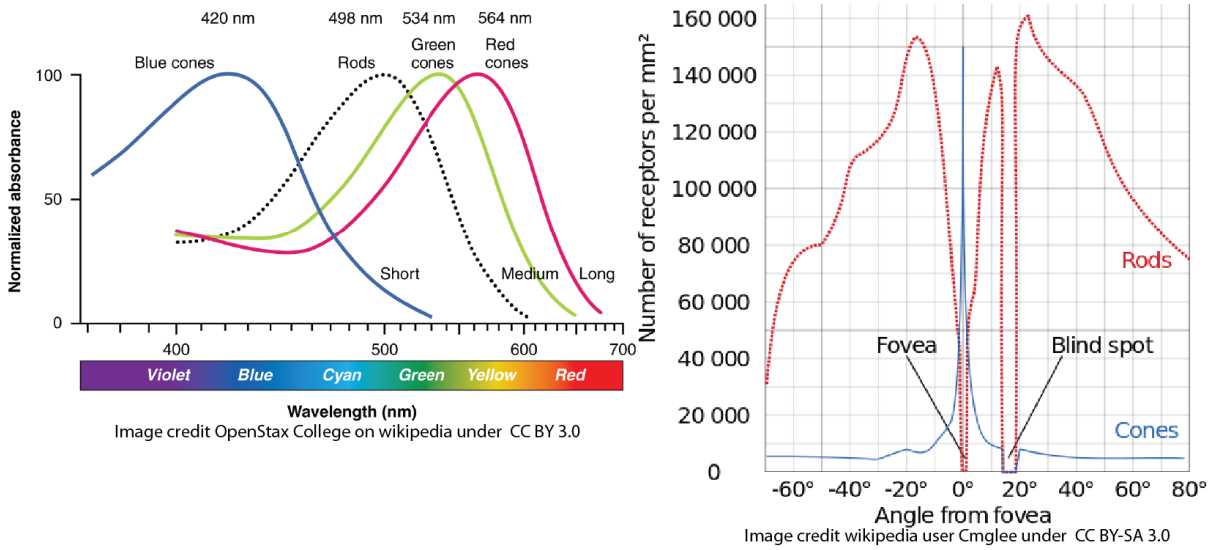

Figure I.3. Spectral response curves (left) of short (blue), medium (green), long (red) cones and rods. Rod and cone density (right) as a function of foveal angle. Note that the blind spot at 20° is due to the optic disk.

from the fovea. The optic disk is a region approximately 15 degrees nasal from the fovea where the ON exits the retina where no photoreceptors are present (Figure I.2 right). The optic disk has been shown to be an important indicator of ON health or atrophy, especially optic disk swelling and crowding [1]. The photoreceptors convert incoming photons to action potentials which are transmitted through retinal ganglion cell axons through the ON.

1.2. Optic Nerve

The ON is a critical structure for vision and transports all visual information generated in the retina posterior through the optic chiasm. The ON consists of myelinated retinal ganglion cell axons as well as glial cells and leaves the orbit via the optic canal at the optic disk. The ON is a central nervous system structure, not a peripheral nerve, and is therefore ensheathed in three meningeal layers. The outermost layer is the thick dura mater, followed by the arachnoid mater. The subarachnoid space contains cerebrospinal fluid (CSF) while the thin pia layer surrounds the ON. (Figure I.3 right) The majority of ON fibers terminate in the lateral geniculate nucleus (LGN) which relays the information

through the optic radiation to primary visual cortex for processing. Some ON fibers also terminate in the pretectal nucleus where they influence reflexive eye movements such as the pupillary light reflex and optokinetic reflex. Yet other fibers terminate in the suprachiasmatic nucleus for regulation of circadian rhythms.

1.3. Optic Chiasm

The optic chiasm is an x-shaped structure near the hypothalamus which separates the anterior visual pathway into the optic nerves anterior and the optic tracts posterior. ON fibers for the nasal visual field cross at the optic chiasm such that information from the left and right visual hemi-fields are transferred into the right and left LGN respectively (Figure I.3 left). The purpose of this crossing is for binocular processing. Left primary visual cortex will receive information from the left visual field from both the left and right eyes. Processing for each point in visual space is then localized to a single spot in visual cortex. If these fibers were not crossed it would lead to a spatial separation of the information for the left and right visual fields coming from the left and right eyes.

1.4. Lateral Geniculate Nucleus

Visual information travels posterior to the chiasm through the optic tracts to the LGN. The LGN acts as a gate receiving feedback signals from areas of visual processing such as the suprachiasmatic nucleus and visual cortex. These signals help to suppress incoming information which is unnecessary to most effectively use the limited bandwidth for transfer of data from the LGN back to visual cortex.

1.5. Diseases Affecting the Optic Nerve

There are many conditions which affect the ON including glaucoma, optic neuritis, optic gliomas, and optic neuropathies [2]. It is important to remember that the location of damage to the visual system will affect the type of visual deficit due to the nature of the fibers crossing at the optic chiasm. ON damage which is anterior to the optic chiasm will degrade vision in the eye on the same side. Damage

posterior to the optic chiasm will degrade vision in the contra-lateral visual hemi-field. Damage to the optic chiasm will result in bilateral degradation.

1.5.1. Glaucoma

Glaucoma is the second leading cause of blindness worldwide and disproportionately affects women and Asians [3]. The two main types of glaucoma are open-angle and closed-angle glaucoma. Open-angle glaucoma is the more prevalent of the two, accounting for 90% of the cases in the United States. Open-angle glaucoma develops slowly and painlessly presenting as gradually progressive visual field loss. This visual field loss begins in the periphery and slowly approaches the center of the visual field. Many patients do not notice the deficit until the disease has progressed significantly. Closed-angle glaucoma is sudden onset and painful and is treated as a medical emergency. The biological basis of glaucoma is not fully understood, yet increased intraocular pressure (IOP) is the only proven treatable risk factor [4]. ON degradation in glaucoma is a well-documented effect and has been shown to precede visual field loss [5, 6]. ON atrophy is more severe at the superior and inferior portions as observed on the optic disk and this atrophy is notably different from ON atrophy from other diseases with its distinctive hourglass pattern [5]. The most common course of treatment is to increase aqueous humor outflow using eye drops. In many cases surgical intervention by opening the trabecular meshwork using a laser or a shunt is necessary (Figure I.1 right). More recent works show the promise of neuroprotective drugs for the reduction of IOP and treatment of glaucoma [4].

1.5.2. Multiple Sclerosis and Optic Neuritis

Optic neuritis is an acute inflammation of the optic nerve and may be associated with a variety of autoimmune disorders or infection. The most common form is acute demyelinating optic neuritis and is closely linked with multiple sclerosis (MS). Approximately 15% to 20% of MS patients have been shown to have optic neuritis as the seminal event in the MS course, and over 50% of MS cases develop optic neuritis at some point [1, 7, 8]. Furthermore, the likelihood of developing MS within 5 years of an optic neuritis event is approximately 25%. Optic neuritis recurrence happens in approximately 30% of patients within 10 years and recurrence is more common in patients who have clinically definite MS [9].

Clinically, optic neuritis presents as a sudden onset of loss of vision and pain of eye movement. Most patients with a single episode of optic neuritis will often recover their vision. The administration of corticosteroids has been shown to expedite visual recovery but has no beneficial effects on long-term outcome [7].

1.5.3. Anterior Ischemic Optic Neuropathy

The term optic neuropathy is used generically to describe damage to the ON, usually atrophy, from any cause. Anterior ischemic optic neuropathy (AION) is a condition whereby the optic nerve head becomes ischemic. AION generally presents suddenly upon awakening and is characterized by reduced visual performance unilaterally without any pain during eye movement. There are two main types of AION, arteritic AION (AAION) and nonarteritic AION (NAION). AAION is due to giant cell arteritis while NAION is often idiopathic and can have numerous causes. AAION is a medical emergency because it has the potential to cause rapid bilateral blindness and must be treated immediately with corticosteroids [10]. NAION is generally thought to be caused by a combination of two factors, optic disk crowding and traditional cardiovascular risk factors. Optic disk crowding is characterized by an optic canal which is not significantly larger than the optic nerve head. This leads to a crowded fiber bundle within the optic disk. Patients who have cardiovascular risk factors, such as diabetes, hypertension or high cholesterol, can develop ischemia to a portion of the optic nerve head. This will cause swelling which leads to compression because of the crowded disk and worsens ischemia [11, 12]. Treatment with corticosteroids has been shown to also improve visual acuity in NAION [13]. A wide range of other treatment options have been presented although none have been proven [14].

1.5.4. Optic Glioma

Optic glioma is a form of glioma, or glial cell tumor, which forms in the ON or optic chiasm. Optic gliomas can cause visual loss depending on the size, location, and involvement of the nerve. Smaller tumors will often not require treatment. Larger gliomas can cause further complications such as raised intracranial pressure (ICP) and proptosis. Treatment of large gliomas is generally through radiation or chemotherapy as surgical resection can be very difficult. Optic gliomas are also closely linked to

Neurofibromatosis type 1, a tumor disorder caused by a genetic mutation [15, 16].

2. Optical Coherence Tomography Imaging

Optical coherence tomography (OCT) imaging has become an invaluable tool for investigation of diseases affecting the retina. OCT creates in vivo sub-micrometer resolution sub-surface images through the plane of the retina and thus is useful for visualizing the layers of the retina and the posterior segment of the eye (Figure I.4). OCT has been shown to be a useful tool in monitoring the progression of both MS and glaucoma. There are many advantages to OCT imaging including that it is non-invasive, non-contact, painless and fast. OCT imaging is fast enough that it can create a real time feed of images as the probe is moved due to this feature intraoperative OCT during ophthalmic microsurgery is under investigation [17, 18]. The sub-micrometer resolution possible with OCT make histological level evaluation of retinal structures viable. OCT also does not impart any ionizing radiation to the patient.

2.1. Background and Techniques

There are multiple approaches to creating OCT images but they all work on the basis of low coherence interferometry. Low-coherence interferometry was first applied to the eye to measure axial length [19] and has since been extended to create 2D and 3D images. The basic principle is that a low-coherence light source projects light onto a beam splitter which splits the beam into a reference arm and a

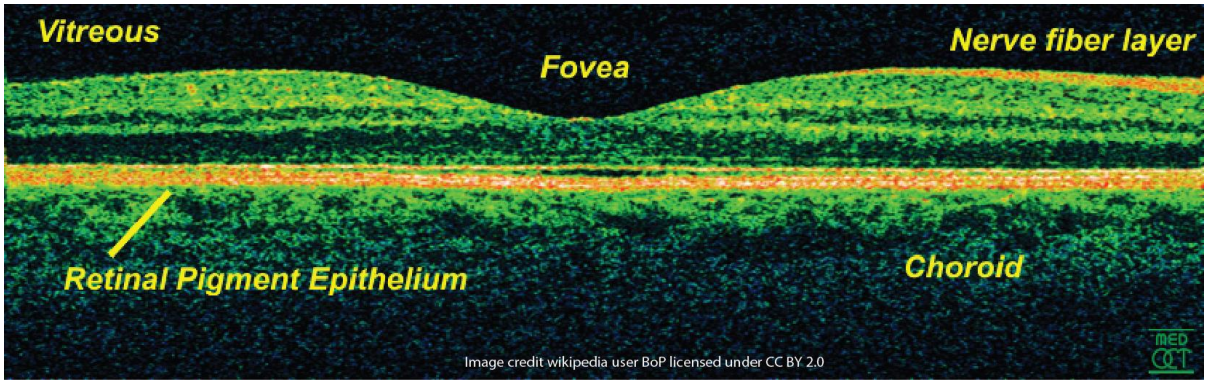

Figure I.4. An 800 nm OCT image with 3 micron in plane resolution showing layers of the retina. The high resolution of OCT allows for investigation and measurement of each layer of the retina.

sample arm. The reference arm reflects off an internal reference mirror. The sample arm reflects light off the target, in this case the eye. The reflections of the two arms meet back at the beam splitter where they interfere. This interference can then be interpreted into axial information about the sample at the target point. The path length of the reference arm can be swept in time with recordings of the interference at each reference arm length being taken to acquire data at different depths. This will produce an A-scan which contains reflective and scattering properties as a function of depth at a single location. Collecting a set of neighboring A-scans constitutes a B-scan which is a single slice through the target. B-scans will contain information as a function of depth and position along the direction of data acquisition which can be visualized as an image of a planar slice. B-scans do not have to be taken in a straight line and are also frequently acquired following a circular path. Multiple B-scans can be combined to form a volumetric image. Volumetric images can be formed using any desired combination of B-scans. Circular B-scans are commonly used to form radial volumetric images. Further improvements in OCT hardware have been introduced building on this principle including the use of broadband light sources to improve axial resolution and by detecting backscattered depth information in the frequency domain which eliminates the need for movement of the reference mirror and improves scan speed [20].

2.2. Applications

2.2.1. Glaucoma

The relationship between retinal nerve fiber layer thickness (RNFL) (Figure I.4) and glaucoma has long been known to exist [21] but OCT has recently allowed for the development of more sophisticated tools for the study of RNFL [22]. OCT has been shown to be a useful tool for measuring RNFL thickness which has been shown to be related to glaucomatous damage [23, 24] and to correlate with glaucoma progression [25]. Software has now been developed to automatically characterize RNFL thickness as well as optic nerve head properties which are visible in OCT. Commercial software is currently available to characterize RNFL thickness measurements as compared to a population of thickness measurements. The current focus of research is on techniques such as registration [26, 27] to

incorporate longitudinal data from different formats which could reveal subtle trends which are not apparent when comparing against a healthy population [28].

2.2.2. Multiple Sclerosis

Multiple sclerosis (MS) is a neurodegenerative disease which is closely linked to optic neuritis. RNFL loss has also been shown in MS patients both with and without a history of optic neuritis although loss is much more extreme in patients with a history of optic neuritis [29]. This supports the hypothesis that RNFL loss associated with MS may be minimal but detectable and can be masked by the severe RNFL thinning associated with optic neuritis. RNFL thinning has been found even in MS patients with a history of optic neuritis with good visual recovery in both affected and healthy eyes [30, 31]. RNFL thinning in eyes without a history of optic neuritis is hypothesized to be due to neurodegenerative retinal ganglion cell degeneration. The use of OCT to measure RNFL thinning has been correlated with brain atrophy in MS and has been proposed as an outcome measure in clinical trials of neuroprotective drugs [32]. The amount of RNFL thinning has been shown to correlate with measures of visual acuity and to be different between MS subtypes [33]. All of these results suggest that OCT and RNFL measurements are useful tools for characterization of MS. The current standard for MS diagnosis is magnetic resonance imaging but OCT represents a promising forefront of MS research as it can provide rapid high resolution reconstructions of retinal anatomy [34].

3. Magnetic Resonance Imaging of the Optic Nerve

Magnetic resonance imaging (MRI) is a critical part of the modern healthcare system and is used routinely for imaging a multitude of anatomies. MRI of the ON however is in its infancy and new techniques are currently under investigation for accurately imaging the anatomy and microstructure of the ON. Creating imaging which is sensitive to ON anatomy is challenging for many reasons including its small size (~3mm), the relatively large amount of motion related to saccadic eye movements, the surrounding orbital fat and the magnetic susceptibility differences resulting from air-tissue interfaces from the sinuses. As optic nerve atrophy is a hallmark of the multiple conditions presented above, there is a

need to develop tools to assess the health of the ON in all 3 dimensions with resolutions high enough to derive indices reflective of recovery and disease evolution. As MRI is also non-invasive, the application to all diseases of the visual pathway can be considered a target for implementation.

3.1. MRI Background

3.1.1. Physical Basis for Imaging

A fundamental principle of protons is that they have a quantum spin number. This property also means that these nucleons have a non-zero magnetic moment. If we place protons in an external magnetic field they will absorb energy and then re-emit energy when they relax back to their original state, known as nuclear magnetic resonance [35, 36]. There are two possible discrete energy states which can be obtained, a low energy state which corresponds to protons which are aligned parallel to the external magnetic field and a high energy state which corresponds to protons which are anti-parallel. The energy spacing between the high and low energy states is given by:

$$\Delta E = \gamma \hbar \vec{B} \tag{I.1}$$

where $\vec{B}$ is the external magnetic field and γ is the gyromagnetic ratio (4258 Hz/G for hydrogen). It is also known that these nucleons will experience a torque on their magnetic moment from the external magnetic field given by,

$$\vec{\Gamma} = \vec{\mu} \times \vec{B} \tag{I.2}$$

where $\vec{\mu}$ is the magnetic moment and $\vec{\Gamma}$ is the torque creating the precession. If this torque is not parallel to the magnetic field it causes the magnetic moment to precess at a frequency ω, known as the Larmor frequency which is proportional to the external magnetic field as,

$$\omega = -\gamma B \tag{I.3}$$

The fraction of the spins parallel and anti-parallel depends on temperature and magnetic field strength and is governed by the Boltzmann distribution. The Boltzmann distribution yields that within a large external

magnetic field, such as within an MRI, at body temperature very few spins (about 1 in 1 million) will be anti-parallel. For a large collection of protons the time evolution of the net magnetization vector can be characterized by the Bloch equation,

$$\frac{dM}{dt} = \gamma \vec{M} \times \vec{B} \tag{I.4}$$

where $\vec{M}$ is the net magnetization vector and $\vec{B}$ is the external magnetic field. The net magnetization vector is a construct which represents the spins of a collection of protons, for a voxel for instance. The net magnetization vector is canonically the sum of all parallel magnetization vectors not cancelled by an anti-parallel magnetization vector.

When this net magnetization vector is perturbed it will relax back to equilibrium through two processes. The longitudinal component, which is parallel to the external magnetic field, will relax exponentially with a time constant T1 while the in-plane component, perpendicular to the external magnetic field, will lose phase coherence exponentially with a decay constant T2 due to interactions with surrounding molecules. The apparent relaxation rate is much faster than this decay constant, T2, due mostly to field inhomogeneities in the main magnetic field. This accelerated relaxation rate is denoted as T_2^* (T2-star) and is always less than or equal to T2 since the apparent relaxation (T_2^*) is the sum of the relaxation rates of molecular interactions and field inhomogeneities as in,

$$\frac{1}{T_2^*} = \frac{1}{T_2} + \frac{1}{T_2'} \tag{I.5}$$

where $T_2^{'}$ is inversely proportional to the magnetic field inhomogeneities while T_2 is a property of the tissue. From this it is clear to see that in the absence of magnetic field inhomogeneities the apparent T2 is the actual T2. We can then utilize the fact that different tissues within the body have different T1 and T2 relaxation times as a means of contrast. T1 and T2 are intrinsic properties of a material and thus different tissues will have different relaxation times. This also means that pathology changes can also change these relaxation rates which allows for visualization of pathology and diagnosis. For example, an inflamed tissue will contain more interstitial fluid from increased vascular permeability and therefore an increased T1 relaxation rate and a decreased T2 relaxation rate. In order to form a meaningful image however we need to extract spatial information.

3.1.2. Image Formation

To form an image we need three magnetic fields all working in unison in a time-varying dynamic manner. The first is the main magnetic field, B_0, which works to align the spins of all protons and produces a net magnetization vector according to the Boltzmann distribution. The second field, commonly denoted B_1, is used to perturb the net magnetization vector created by the main magnetic field. As the protons relax we then need to measure the signal and we can leverage the fact that each proton precesses at the local Larmor frequency as a means of encoding spatial location. If we introduce a spatially varying magnetic field gradient the frequency of precession of the spins will vary based on the magnitude of the applied magnetic field and therefore also on spatial position. This relationship between frequency and location allows us to then reconstruct the image by taking the Fourier transform of the collected signal since each frequency will correspond to a spatial location in physical space [37].

3.1.3. The Spin-Echo Sequence

The art of manipulating the three magnetic fields in an MRI experiment to generate the desired contrast in an image is known as pulse sequence design. One of the most basic pulse sequences is the spin-echo (SE) sequence [38]. This sequence is versatile and changing the timing of the sequence can produce T1-weighted, T2-weighted or proton density contrast [39]. The signal in a SE sequence is generically described by two parameters, the repetition time (TR) and the echo time (TE),

$$S = M_0\left(1 - 2e^{-\frac{\frac{TR-TE}{2}}{T_1}} + e^{-TR/T_1}\right)e^{-TE/T_2} \tag{I.6}$$

Where M_0 is the equilibrium longitudinal magnetization and S is the signal. To understand each component of this equation we look at the structure of the pulse sequence. This sequence employs a 90° excitation pulse to tip the net magnetization vector into the transverse plane. As the spins begin to dephase a 180° refocusing pulse is applied to reverse the direction of the dephasing, so that the spins are rephased which is called an echo. Note that this refocusing also refocuses any magnetic field inhomogeneities such that the apparent T2 (T_2^*) is the actual T2. An image is then read out at a time t (t = TE for maximum signal) after the excitation pulse using the gradients as discussed above. The process

can be repeated at a time TR after the original excitation pulse. Referring back to the signal equation, (0.1), we see that the first term with $\frac{TR-TE}{2}$ is due to the longitudinal relaxation between the refocusing pulse and the readout while the second longitudinal relaxation term is due to residual longitudinal magnetization from the previous TR. Finally the entire equation is weighted by the transverse magnetization signal for the prescribed echo time. From this equation we can see how different forms of contrast can be imaged with just this single sequence. A long TR and long TE will result in T2-weighting while a short TR and short TE will result in a T1-weighting. A long TR and short TE yields a proton density weighted image. The SE pulse sequence has a number of advantages, most notably for application to ON imaging is that the 180° refocusing pulse off-resonance effects making the spin echo sequence more robust to field inhomogeneities and susceptibility artifacts as compared to other pulse sequences.

3.2. Challenges

MRI of the ON presents a multitude of challenges including:

- The small size of the ON presents a challenge as high-resolution sequences are necessary to avoid partial volume effects.
- The obfuscation of signal from the surrounding adipose tissue makes creating contrast in the ON challenging. The T2 relaxation time of the ON is similar to that of orbital fat making fat suppression difficult. Robust fat suppression is also necessary as the olifenic orbital fat can resonate at different frequencies and therefore will not be suppressed by traditional fat suppression techniques.
- The location of the ON directly superior to the maxillary sinuses causes significant susceptibility artifacts. The maxillary sinuses are a bony structure filled with air. This combination of air and bone creates local magnetic field gradients due to the different magnetic susceptibility of each material which must be accounted for.
- The mobility of the ON due to eye movement causes blurring and motion artifacts. Any

sequence optimized for the ON should act to minimize these artifacts.

MRI is often focused on imaging the brain with fields of view on the order of 20 cm and resolutions on the order of 0.1-0.3 cm. The ON however is approximately only 0.3 cm in diameter. This means that conventional MRI methods targeting the brain do not have sufficient resolution to accurately characterize the ON (voxel size ~ structure size) and would result in severe partial volume effects for all voxels imaged. To accurately resolve the ON high resolution (> 1mm) imaging sequences will be required.

The orbit contains the ON and surrounding CSF traversing posterior-medially as well as the ocular muscles, the rest of the space is occupied by orbital fat (Figure I.5A). Orbital fat (T2~68ms [40]) has a similar T2 relaxation time as the ON (T2~78ms [41]) and can obfuscate signal and make imaging difficult on conventional T2-weighted MRI. The suppression of orbital fat signal needs to be carefully considered when using T2 imaging of the ON.

Magnetic susceptibility can be summarized by a proportionality constant χ, which describes the amount of magnetization in a material in the presence of a given external magnetic field.

$$\vec{M} = \chi \vec{B} \tag{I.7}$$

Magnetic susceptibility generally reflects the properties of a material. Tissue is diamagnetic and thus has a very small (on the order of 10^{-6}) and negative magnetic susceptibility. Air is made up of mostly nitrogen, which is diamagnetic ($\chi = -12 \times 10^{-6}$), and also about 21% oxygen, which is paramagnetic ($\chi = 34.5 \times 10^{-4}$) [42]. Two areas with different susceptibility within the same external magnetic field will have different magnetization and thus a magnetic field gradient exists between any two areas with different susceptibility. These magnetic field gradients accelerate dephasing between protons on either side of the boundary which can lead to T2 signal attenuation as well as image distortion [43, 44]. These effects are especially detrimental for ON imaging since the ON sits directly superior to the air pocket and bone of the maxillary sinuses (Figure I.5B) [45].

Another problem which must be addressed is the motion of the ON (Figure I.5C). Saccadic eye movements cause rapid movement, the peak angular speed of the eye can exceed 900°/s for large

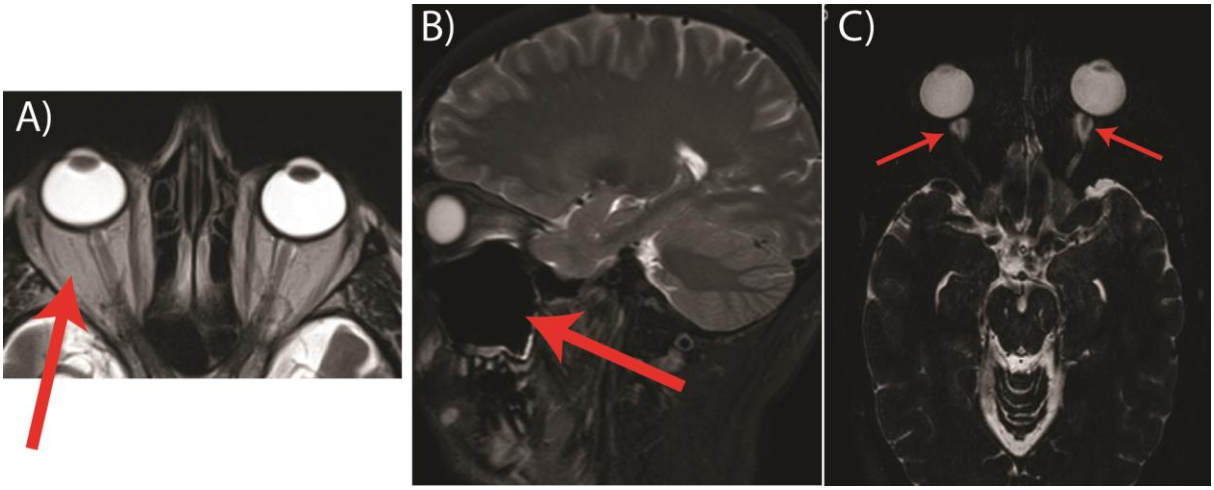

Figure I.5. Illustration of challenges in MRI of the ON which includes orbital fat obfuscation of ON signal due to similar T2 (A). The proximity the of the maxillary sinuses which leads to susceptibility (B) and ON motion immediately posterior to the eye globes due to eye movement during acquisition (C).

saccades while smaller saccades (<1°) typically result in peak angular velocity of ~80°/s [46]. This rapid motion also causes significant motion of the ON immediately posterior to the globe. During longer imaging acquisitions, participants may also fall asleep. If the participant enters REM sleep the movement of the ON becomes saccadic and eye movement can exceed 30°/s [47]. One technique to reduce this motion is to have the participant fixate on a target to minimize saccadic eye movements. This technique will reduce larger motion artifacts but motion cannot be completely eliminated. Thus, motion of the ON can cause blurring of the ON signal and must be accounted for when designing ON imaging.

3.3. Applications

MRI has been used as a method to study the ON since at least 1984 [48] and specifically atrophy in MS and optic neuritis patients since at least 1988 [49]. The size of the ON has been measured in patients using manual measurements of cross-sectional area at predefined locations along the ON with MS and optic neuritis with findings indicating measurable atrophy [50]. Patients at onset had inflammation which led to larger mean ON cross sectional area of 16.1 mm^2 compared to healthy controls at 13.4 mm^2. After 52 weeks inflammation had turned to atrophy with mean patient ON measurements at

11.3 mm^2 [51, 52]. MRI in these studies did not fully address the previously raised concerns and required time consuming manual segmentation. For these reasons the focus has been mostly on the use of OCT imaging for evaluation of MS and optic neuritis [53]. MRI does however provide the advantage of being able to characterize ON atrophy along the entire length of the nerve and if reliable imaging and automated segmentation techniques were readily available could be used for more accurate characterization of ON atrophy.

MRI has also been proposed to differentiate optic neuritis and NAION [54]. Optic neuritis and NAION often present very similarly in the clinic although the ON is ischemic and enlarged for NAION after a period of time ON atrophy will become apparent in patients with acute optic neuritis leading to MS. NAION patients will have their ON size return to normal. MRI has been shown to be a possible differential diagnosis between these two conditions [54]. Robust imaging and automated segmentation tools would lead to a useful clinical tool for identifying and quantifying ON atrophy to differentiate cases of acute optic neuritis and NAION.

3.4. Imaging History

Anatomical MRI of the ON has been attempted as early as the mid-1980s [55] to evaluate ON gliomas [56] and optic neuritis [49]. These early studies used 0.5T scanners with a resolution of 1.0x1.0x10.0 mm^3 [55]. The acceptance of 1.5T scanners yielded higher resolution sequences at 0.8x0.8x5.0 mm^3 by 1996 [57]. By the year 2000 the problem was well characterized as a challenging one and qualitative assessment was possible while the future looked bright for quantitative MRI in the ON [58]. The move to 3T MRI allowed for still higher resolution sequences, 0.45x0.49x3.0 mm, but still lacked robust fat suppression and motion compensation. The thick slices confounded the problem of partial volume effects since slice thicknesses were approximately as large as the diameter of the ON [59]. In 2007 Hickman noted that imaging of the ON was advancing and there was an emerging need for automated segmentation tools as well as the need for better imaging techniques [60]. His point is well founded; the literature for segmentation of the ON is almost exclusively for manual segmentation

techniques [51, 52, 54, 61] and semi-automated methods [62]. Only recently have automated segmentation methods been applied to the ON [63].

4. Magnetization Transfer Imaging

One fundamental limitation of the traditional MRI techniques from Section 3 is that they inherently measure the relaxation of free water Hydrogen protons. The precession frequency of any hydrogen protons bound to a macromolecule is too high and therefore the relaxation is too short (<10ms) to be measured with traditional MRI pulse sequences such as the spin-echo sequence presented in Section 3.1.3. Probing of macromolecular structure within a voxel is of interest though as this could lend information on important biological structures, such as myelin, which are present within the voxel. With the clever use of pulse sequences however we can probe these hydrogen protons bound to the edges of macromolecules, henceforth the bound pool, and their interactions with the free water hydrogen protons, henceforth the free pool. Experimental designs aiming at measuring this phenomenon were seen as early as 1963 [64] while some of the first measurements in NMR date back to 1989 [65].

4.1. Magnetization Transfer Contrast

Generation of magnetization transfer (MT) contrast is achieved by irradiating the bound pool protons with a radiofrequency saturation pulse and the measurement of the nonirradiated free pool. Irradiation of the bound pool is achieved by applying a radiofrequency pulse off-resonance as the bound pool spins have a much broader absorption lineshape than the free pool spins. If the exchange rate between the two pools is slow enough, as it is in tissue, a traditional imaging experiment can then be performed after saturation to measure the decrease in signal of the free pool which is a result of the transfer of saturated protons from the bound pool [66]. It was not long before it was discovered that MT contrast had the benefit of being able to detect biophysical tissue changes in MS [67]. By 1996 there were efforts for deployment of MT imaging for clinical use but it was marred with difficulties [68]. These types of experiments utilized the magnetization transfer ratio (MTR) for quantification of the MT effect.

$$MTR = \frac{M_0 - M_s}{M_0} \tag{I.8}$$

MTR is defined as the difference in signal between images acquired with (M_s) and without (M_0) the application of a saturation pulse, scaled by the signal without a saturation pulse. By 1999 there was a multi-site study for characterization of MTR in normal white matter [69]. While this technique has proven useful we also now understand the limitations of modeling such a complex process so simplistically. Modern methods have moved on to quantitative modeling of the exchange process to more accurately characterize the underlying macromolecular content of the voxel. One key development which allowed for the spread of MT imaging and paved the way for quantitative modeling methods was the development of pulsed MT methods allowing for more measurements to be taken within SAR limitations [70]. The reduction of the MT phenomenon to a single measure, MTR, was known to be an oversimplification and although MTR is a useful construct, even being used in clinical trials, by 2001 a quantitative formulation of MT (qMT) exchange had emerged [71].

5. Image Processing

Image processing is the extraction of meaningful information about the subject of an image using manual or automated techniques. Medical image processing is a broad topic and here we will attempt to provide a framework which is relevant to this work. We discuss segmentation of medical images, non-convex fitting through conjugate gradient descent and non-linear regression using random forests.

5.1. Segmentation

The process of identifying meaningful anatomical structures within an image is known as segmentation. Segmentation problems vary widely based on the anatomy of interest and special considerations with each individual application. Segmentation has many applications including surgical planning, post-surgical assessment and abnormality detection [72]. Abnormality detection is of particular interest for this work and can include finding abnormal tissue (e.g. tumors) or detecting abnormal image

features whether they be structural, textural or intensity in nature. Segmentation is key to all of these tasks as the anatomy of interest must be localized to be analyzed.

Medical image segmentation has been applied to a wide variety of anatomies but the classic anatomy of interest in segmentation of the brain. The brain was one of the first structures to be segmented due to the relative regularity across subjects, the rigid container of the skull and the attractive applications. Moving to other anatomies, such as the ON which is surrounded by compressible fat and has a shape that varies widely between subjects, these constraints do not hold and complicate the problem. Despite these challenges recent advances have been made in applying segmentation to a variety of anatomies [73].

Image segmentation has traditionally been performed manually by trained observers such as a radiologist. In the late 1990's computer-assisted segmentation methods were developed. These methods increased the accuracy and speed by which an observer could segment images by utilizing image context information to inform the final segmentation [74, 75]. While these methods were a step in the right direction the ultimate goal was to develop robust automated methods to replace the human intervention. This task proved difficult and to this day computer assisted segmentation is the *de facto* standard for many difficult to segment anatomies, including the ON [51, 60].

Automation of segmentation tasks yields large benefits in the scale at which data can be analyzed. Computer assisted segmentation decreases the number of man hours required for each segmented volume while automated segmentation reduces it almost completely. This reduction in time facilitates the analysis of large data sets previously unreachable. Automated segmentation also has the benefit of reducing any bias introduced by human intervention, yielding more reliable segmentation results. Initial attempts at automated segmentation were focused on pattern recognition [76, 77]. Intensity models have also been used to segment images and correct for global inhomogeneities [78]. Today, there are many methods to automated segmentation including thresholding, region growing, clustering, neural networks, Markov Random Field models, deformable models and atlas-based approaches [79]. Atlas-based approaches including multi-atlas segmentation have had success in a variety of anatomies [73]. Canonical multi-atlas

segmentation involves registering a set of multiple atlas images to the target image to be segmented. In this context an atlas image is a previously labeled example. With all of the atlas images registered to the target space the segmentation of each atlas is propagated to the target through a process referred to as label fusion.

5.2. Conjugate Gradient Descent

There exists a multitude of methods for solutions to non-linear optimization problems [80]. If the gradient of the function to be optimized can be solved for analytically, that is the derivative of the objective function with respect to each parameter to be optimized, then gradient descent methods can be employed [81, 82]. Conjugate gradient methods are a good solution for unconstrained energy minimization problems iteratively when more direct solutions are prohibitive to implement. This method has the benefit of defining a search direction as the negative gradient direction of the objective function. This ensures that the objective function should always be decreasing until a minimum is reached. The conjugate of this method denotes that descent directions at subsequent iterations be conjugate to each other. This has been shown to ensure faster convergence, derivation of this is beyond the scope of this document.

5.3. Random Forest Regression

Random forest regression and classification has gained popularity in medical imaging applications in recent years [83, 84]. Random forests are an ensemble learning method, meaning they use multiple models to learn a better solution than any one model, using an ensemble of decision trees. Decision trees predict some output, either classification or a value for regression, based on a set of higher dimensional input. The root of the tree splits into multiple interior nodes, each of which contains a decision based on one of the input features. The nodes on the tree can be learned by repeatedly splitting the training data into subsets. This splitting procedure continues until the entire subset at a node contains the same output value. At this point a leaf node, or end node, is created which contains the output value.

Once a decision tree is learned, application is simple as an input data point can traverse each decision node until it reaches an end node which will contain the desired output value. Random forests are learned by training multiple decision trees on random subsets of the input features [85]. Training of a random forest intrinsically minimizes the error of regression of the training data. Validation of this error, to avoid overfitting, is important with the use of a yet unseen testing data set. The accuracy of the forest can then be evaluated on the testing data which was not used to train the model and should correspond to the generalization error of applying the model to any other yet unseen data.

6. Contributions

The primary contributions of this dissertation are as follows. In **Chapter II** we present a fully automated multi-atlas segmentation technique optimized for the structures of the eye orbit. In **Chapter III** we present a novel MRI sequence optimized to provide superior contrast of the ON and sub-arachnoid CSF for accurate characterization ON morphology. We also propose an intensity-model fitting based technique for automatically estimating the radius of ON and surrounding CSF utilizing this novel MRI contrast. In **Chapter IV** we evaluate the reproducibility of this technique as well as demonstrate the creation of a normative statistical atlas using healthy controls. **Chapter V** presents improvements which build upon the limitations of the slice-wise intensity model fitting technique from **Chapter III** by proposing an iterative method which enforces 3-dimensional consistency of radius estimations. Again this technique is evaluated for reproducibility and we present the first long-term reproducibility results demonstrating stability of this technique and optic nerve morphology in subjects scanned one year apart. In **Chapter VI** this technique is applied to a clinical population to compare differences between patients with MS and a history of optic neuritis as well as patients with MS with no history of optic neuritis. We find that global atrophy is detected using our automated method in patients with MS and a history of optic neuritis. **Chapter VII** presents a multi-modal short- and long-term reproducibility data set which is released as an open resource for future development of eye orbit analysis pipelines. We also present morphological normative values from MRI and retinal layer thicknesses from OCT. **Chapter VIII**

presents analysis of a large-scale retrospective population of clinically acquired scans utilizing the techniques presented in **Chapter II**. In **Chapter IX** we use simulation to optimize sampling of quantitative magnetization transfer modeling to reduce scan times and increase clinical viability. Finally, we conclude in **Chapter X** by summarizing contributions and discussing possibilities for future work. More specifically we:

- We designed and implemented a **robust automatic multi-atlas segmentation pipeline** of the ON, eye globes and muscles for use on clinically acquired data sets utilizing multiple sets of atlases to account for various MRI pulse sequences. Multi-atlas segmentation has been applied to many anatomies successfully but was never optimized for segmentation of eye orbital structures. Optimization of this technique builds the foundation for large-scale retrospective analysis of clinical imaging populations. To increase the amount of data which can be included in these investigations we employ multiple sets of atlas images to segment various contrast mechanisms derived from various MRI pulse sequences.
- We optimized a **high-contrast, high-resolution 3-dimensionally acquired MRI pulse sequence** for contrast in the challenging ON. MRI of the ON is challenging because of size, motion, orbital fat and susceptibility artifacts. We account for all of these challenges by utilizing a 3-dimensionally acquired, radial readout pattern on a Cartesian grid to account for motion. We use robust spectral pre-saturation inversion recovery fat suppression to suppress orbital fat. We utilize an extended echo-train T2W turbo spin-echo sequence to refocus susceptibility artifacts and we use high-resolution isotropic acquisition to ensure accurate visualization despite the small size of the structure.
- We designed a tool for **automatic measurement of the ON and surrounding CSF** by fitting an intensity model in the coronal plane. Taking advantage of the novel contrast created with the previous contribution we created an intensity-fitting based algorithm for estimating the radii of the ON and CSF from these images. This model takes into account

the nonlinear relationship between its parameters and the physical radius measurements using a random forest regression and is validated against manual measurements and for reproducibility.

- We defined **a normative distribution of the ON and surrounding CSF size in young healthy controls** which will be useful for comparing patient populations to identify structural changes due to ON diseases. By applying these tools to a large number of young healthy subjects we were able to define a statistical model of a normal human ON. This model can now be utilized for comparisons against patient populations to evaluate group effect changes in ON morphology.
- We improve upon the automatic measurement tool using **iterative 3-dimensional constraints** to enforce anatomical consistency. The initial proposal of this algorithm utilized a naïve slice-wise estimation of each ON and CSF radius. This method was sufficient as a first step but ignores valuable information from neighboring slices. By positing this model into an iteratively constrained framework we enforce measurements to be more anatomically viable while still maintaining validation through short-term reproducibility.
- We apply this improved technique to a **population of patients with MS and find differences** between patients with MS and a history of optic neuritis as compared to healthy controls and no difference in patients with MS and no history of optic neuritis as compared to healthy controls. This experiment showcases the utility of the development of these algorithms for increasing our understanding of underlying disease processes and morphological changes which have yet been inaccessible to researchers non-invasively.
- We evaluate the **long-term reproducibility of ON radius and various other eye orbital MRI morphological metrics**. As these new tools are developed they must be validated for reproducibility. We have acquired a short- and long-term reproducibility data set

which is being released for standardized evaluation and comparison of new eye orbital analysis methods.

- We apply these techniques to a **large-scale retrospective clinical MRI population to evaluate structural-functional relationships** and to detect latent features which may be crucial to visual function not yet being utilized in clinical MRI. We show that quantification of clinical quality structural MRI through automated analysis explains variance in visual function across subjects. This work showcases the benefits of developing algorithms useful in evaluating clinical imaging allowing for research into large amounts of clinical data.
- We develop a **framework for numerically optimizing qMT sampling** to reduce scan times and improve clinical viability. MT has been clinically applicable but the extension to qMT has been hampered by long scan times. We utilize a simulation framework to optimize qMT sampling allowing for more clinically viable sequences to be developed.

6.1. Previous Publications

Many contributions of this dissertation have been previously published. A robust pipeline for segmentation of ON, eye globes and muscles on clinically acquired data is proposed [86]. A method for automatic measurement of the radius of the ON and surrounding CSF by fitting an intensity model [87]. An application of the previous two methods to healthy controls to develop a normative population useful for analyzing patient populations [88]. Short-term reproducibility analysis of ON measures [89]. Three-dimensional consistency improvements to the ON radius estimation algorithm [90]. The application of the improved ON radius estimation tool to MS patients [91]. **Chapter VIII** is an extension of work co-authored with a high-school student I helped mentor as first author showcasing structural-functional relationships from image segmentation metrics [92]. Lastly, the ON imaging reproducibility experiment and results [93].

Chapter II. Robust Optic Nerve Segmentation on Clinically Acquired CT

1. Introduction

The ability to model structural changes of the optic nerve (ON) throughout the progression of disease (e.g., inflammation, atrophy, axonal congestion) is significant to characterization of neuropathic diseases. Hence, accurate and robust segmentation of the ON has the capacity to play an important role in the study of biophysical etiology, progression, and recurrence of these diseases. Considerable work has been done using manual segmentation techniques on computed tomography (CT) for investigating pathology. For example, Chan *et al* developed orbital soft tissue measures to assess and predict thyroid eye disease [94] and Weis *et al* described metrics to thyroid-related optic neuropathy [95]. Bijlsma *et al* highlighted quantitative extraocular muscle volumes as an essential target for objective assessment of therapeutic interventions [96]. Manual delineation of ON structures is time and resource consuming as well as susceptible to inter- and intra-rater variability. Automatic quantification of the location and volumetrics of the ON would allow for larger, more powerful studies and could increase sensitivity and specificity of pathological assessments compared to coarse, manual region of interest (ROI) approaches.

Ideally, automated procedures would result in accurate and robust segmentation of the ON anatomy. However, current segmentation procedures often require manual intervention due to anatomical and imaging variability. Bekes *et al* [97] proposed a geometric model-based method for semi-automatic segmentation of the eye globes, lenses, optic nerves and optic chiasm in computed tomography (CT) images and reported quantitative sensitivity and specificity results from simultaneous truth and performance level estimation (STAPLE)[98] of approximately 77%. Qualitatively, this study reported a lack of consistency with the results they obtain for the nerves and chiasm. Noble and Dawant [99] proposed a tubular structure localization algorithm in which a statistical model and image registration are used to incorporate a priori local intensity and shape information. This study reported mean Dice similarity coefficient (DSC)[100] of 0.8 when compared to manual segmentations over ten test cases. Unfortunately, the success of automated techniques is often dependent upon the application, modality and

image quality.

Atlas-based methods provide a model-free approach to segmentation, which use atlases (pairings of anatomical images with a corresponding label volume) to segment a target volume. Other efforts have developed a single-atlas approach targeting the ON for radiation therapy and reported a mean DSC of 0.4-0.5 [101-103]. Multiple atlases significantly improve the accuracy compared to a single atlas [104, 105]. In a multi-atlas approach, multiple atlases (existing labeled datasets) are separately registered to the target image. Label fusion is used to resolve voxel-wise conflicts between the registered atlases. Although multi-atlas segmentation promises a robust and model-free approach to segment medical images from exemplar brain images, varied and limited success has been seen for segmentation of the ON with DSC ranging from 0.39 to 0.78 [101-103].

We explore the development of a more reliable multi-atlas technique for the segmentation of the ON, eye globe, and muscles on clinically acquired CT images. Our emphasis is on characterizing algorithms that function across a wide variety of clinically acquired images as opposed to less translational algorithmic innovations. This chapter is organized as follows. First, we evaluate three current non-rigid registration algorithms: (1) NiftyReg; (2) Automatic registration Toolbox (ART); (3) ANTS Symmetric Normalization (SyN) deformable registration algorithms. Second, we evaluate six label fusion algorithms: (1) majority Vote (MV); (2) STAPLE; (3) Spatial STAPLE (spSTAPLE); (4) Locally Weighted Vote (LWV); (5) Non-Local STAPLE (NLS); (6) Non-Local Spatial STAPLE (NLSS) and present implementation details of each algorithm. For each method, we present quantitative

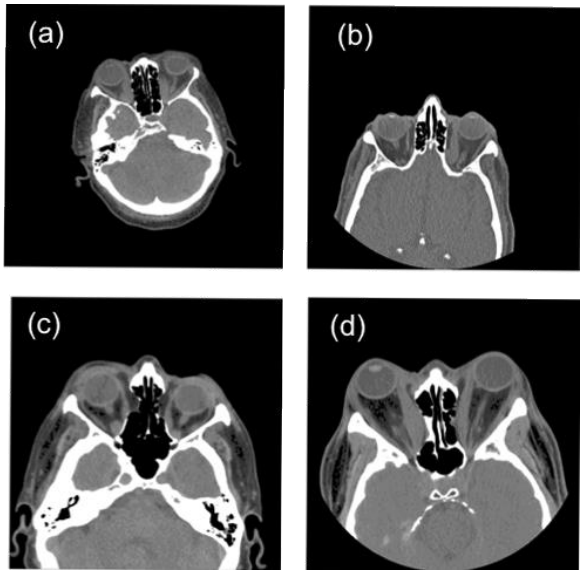

Figure II.1. Clinically acquired CT images are shown for four representative subjects (a-d). Note the variation in field of view and pose.

and qualitative performance characteristics. Finally, we evaluate the performance of the optimal pipeline on a large dataset to demonstrate its robustness.

2. Methods

2.1. Data Set

CT imaging from 183 thyroid eye disease patients was collected for a total of 543 image volumes. Of the patients selected, 81% are females and 70% are Caucasian with ages ranging from 9-83 with an average age of 49. As part of a larger study of thyroid eye disease, CT scan volumes of these patients were clinically collected from 2003 to 2011 using a wide variety of settings and scanners from Philips, GE, Picker and Marconi. The dataset was anonymized during image retrieval from the radiology archives; detailed CT acquisition parameters are not available. An arbitrary subset of 30 scan volumes from 30 distinct patients was selected to guide development and algorithm evaluation.

On the selected scan volumes, "ground truth" segmentations were performed by experienced raters using the Medical Image analysis Processing And Visualization (MIPAV) software package (http://mipav.cit.nih.gov/)[106] for the full length of the left and the right optic nerves, eye globes and two pairs of extraocular muscles on all the subjects. A single rater labeled all CT scan volumes and a second rater labeled an overlapping subset of 15 scan volumes. Raters were graduate students in medical imaging who were trained by radiology faculty and supervised by ophthalmology faculty. Raters worked on Dell T3500 workstations with dual 22 inch high definition displays and Wacom Intuos tablet input devices. Boundary definitions for all structures were obtained according to the signal intensity differences in the images. The remaining scan volumes were used for evaluation of the final algorithm.

Table II-1 Variability in slice thickness for the manually labeled subset of 30 subjects

Slice thickness (mm)	<=0.4	>0.4 & <=0.5	>0.5 & <=1.0	>1.0 & <=2.0	>2.0 & <=2.5	> 2.5 & <=3.0	>3.0
Atlas images	2	8	1	4	12	2	1
All images	3	97	86	101	153	60	43

Clinically acquired CT data for the ON often varies in the target field-of-view (Figure I.1), ranging from whole head to more localized images of the orbit with slice thicknesses ranging from 0.4 to 5 mm (Table II-1**)**.

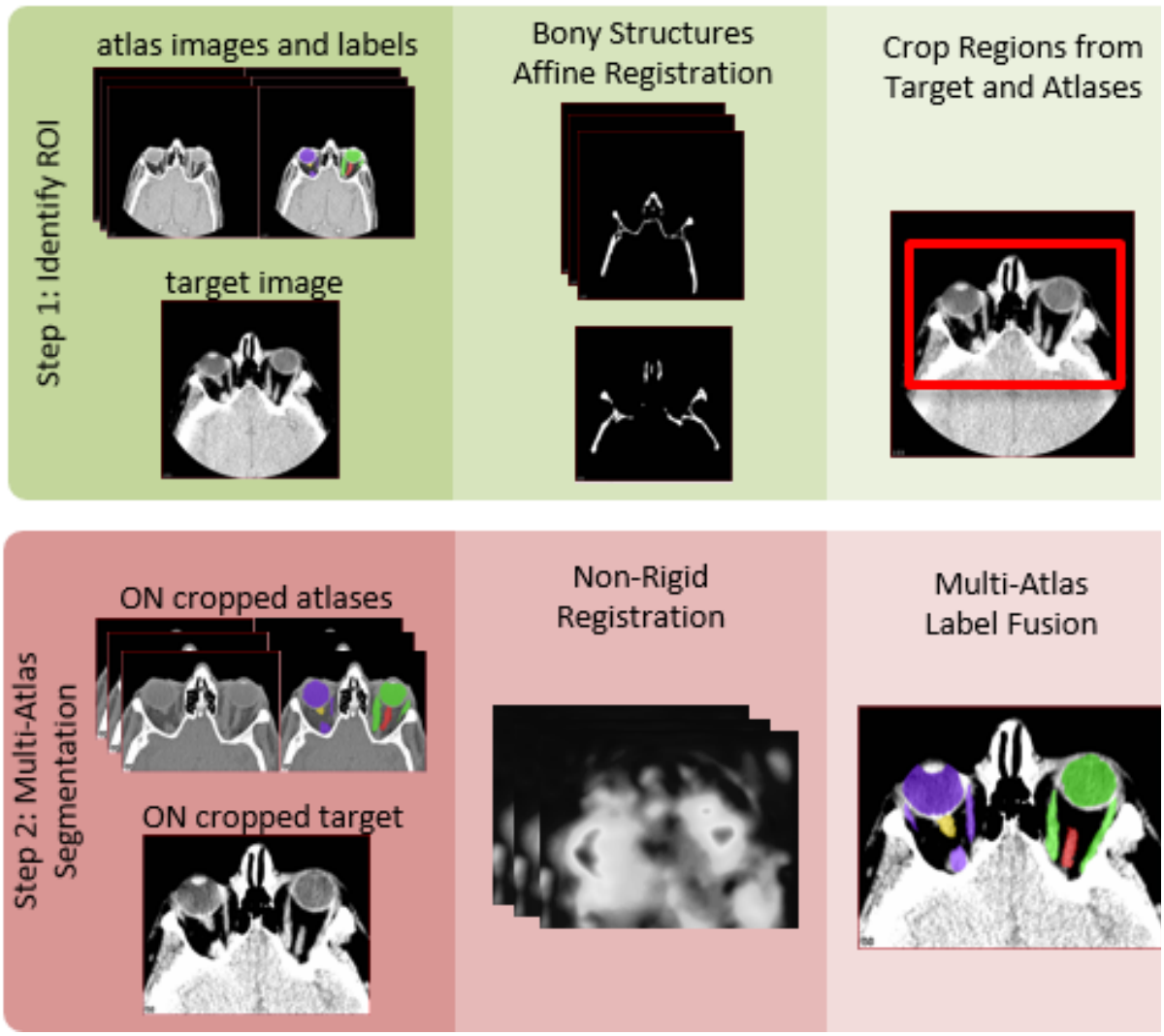

Figure II.2. Flowchart of the ON robust registration and multi-atlas segmentation pipeline. The left (yellow) and right (red) ONs are enclosed within the two pairs of muscles, which connect to the eye globes. The left and right eye globes and muscles are seen in purple and green,

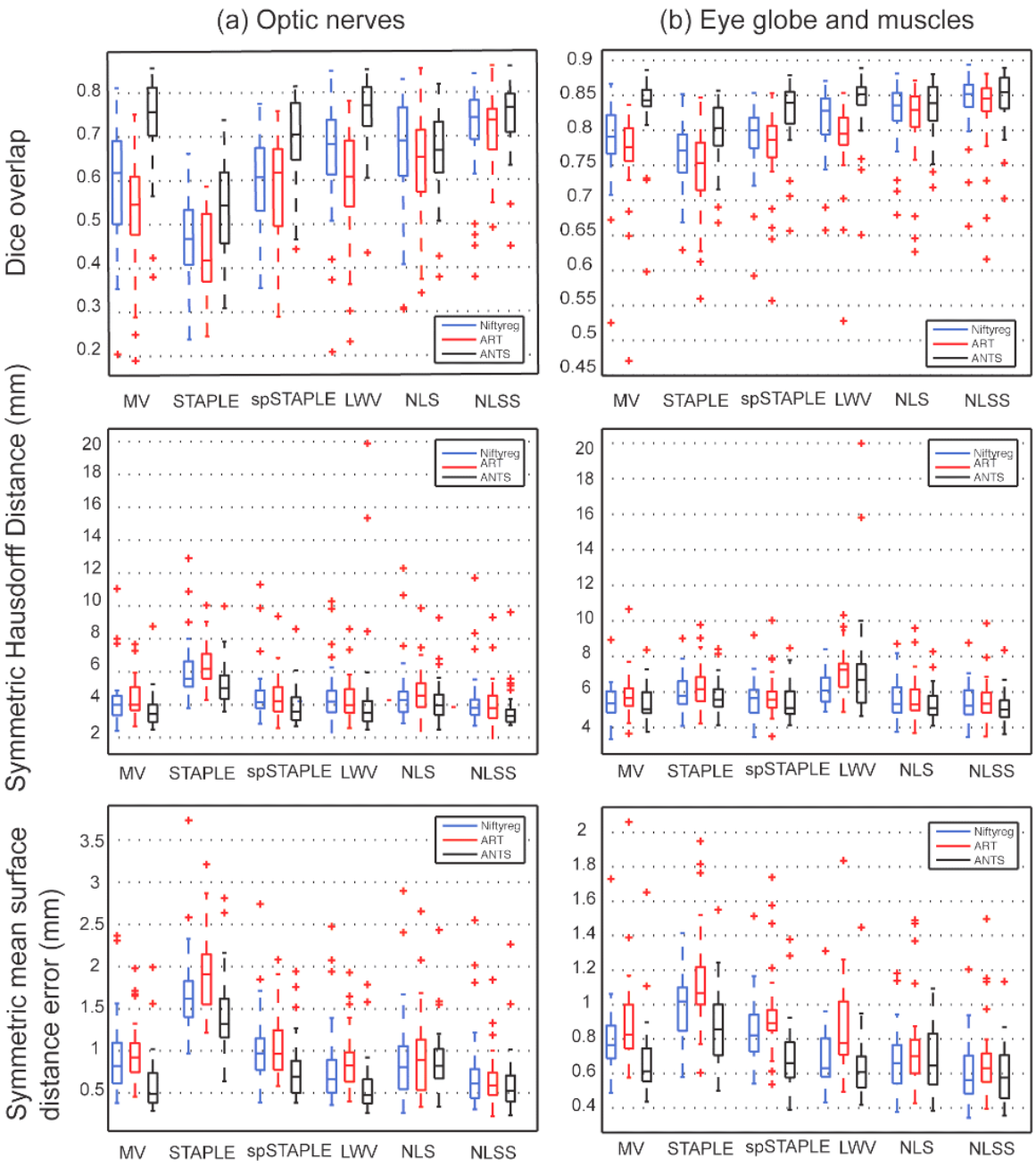

Figure II.3. Quantitative results of the evaluation of non-rigid registration and label fusion algorithms in the ON and globe structure show that SyN diffeomorphic registration followed by NLSS label fusion is the most consistent performer across all 30 subjects.

2.2. Development Methods

An outline of the proposed algorithm can be seen in Figure II.2. Briefly, we localize the ON using an affine registration of the bony structures to define a reduced field of view ROI around these structures. Multi-atlas segmentation is then performed on the reduced field of view image volumes using non-rigid registration and statistical label fusion.

The first step in the multi-atlas pipeline is to identify the general region of the orbits from within any clinically acceptable fields of view. The bone structure for each image is identified using an experimentally determined threshold at the minimum intensity increased by 30% of the range of intensities. Pairwise affine registration is then performed between the bone thresholded images using the Aladin algorithm [107, 108] from the NiftyReg package.

The labels are transformed to the target space using the aforementioned affine registrations. Propagated labels are then averaged over the number of atlases to obtain a probability image for each target. To estimate the approximate centroids of the ocular structures, voxels are identified as those where greater than 90% of the atlases contain ON labels. This set of voxels is then partitioned into 2 groups, the left and right ON regions, using k-means clustering. The centroids of these clusters are extended by 40 mm, a field of view determined experimentally, in all 3 dimensions to obtain the ON ROI.

Final registrations are computed by performing pairwise non-rigid registration deforming the cropped atlas to the cropped target. Note that for all registration steps, the target image (i.e., dataset to be labeled) was considered as fixed. Three non-rigid registration methods were evaluated: (1) NiftyReg with normalized mutual information and the bending energy used to construct the objective function; (2) ART [109] with default parameters; and (3) ANTS SyN deformable registration [110] with cross correlation similarity metric window of radius 2, a Gaussian regularizer with $\sigma = 2$, and max iterations of 30x99x11, 3 resolution levels with max iteration of 30 at the coarse level, 99 at the middle level and 11 at the nest level, and step size 0.5 [111]. Atlas labels are transferred to the target coordinate space using the deformation fields and nearest neighbor interpolation. Finally, label fusion is used to generate the final

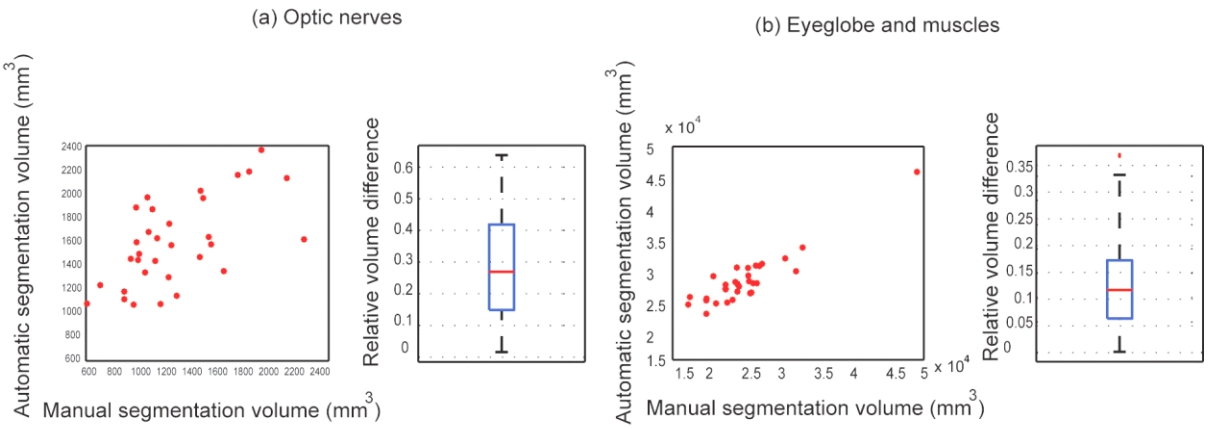

Figure II.4. Quantitative results of the subject-wise volume measurements between manual and automatic segmentation.

segmentation.

The following label fusion algorithms were evaluated: (1) MV [104, 105, 112] with log-odds weighting [113]; (2) STAPLE [98]; (3) spSTAPLE [114]; (4) LWV [113] with a decay coefficient of 1 voxel; MSD similarity metric for the target and atlas intensities; standard deviation of the assumed intensity distribution, σ_i = 0.5; (5) NLS [114]; (6) NLSS, an extension to the NLS framework, allows for the estimation of a smooth spatially varying performance level field. Parameters for all of the STAPLE

Table II-2 Parameter values used for variations of the STAPLE algorithm

Algorithm	**STAPLE**		**Spatial**		**Non-Local**			
	Performance Parameter	Initialization Decay	Half-window size (mm)	Global bias	Search neighborhood (mm)	Patch neighborhood (mm)	σ_i (mm)	σ_d (mm)
STAPLE	0.95	0.5	-	-	-	-	-	-
SpSTAPLE	0.95	0.5	3x3x3	0.25	-	-	-	-
NLS	0.95	0.5	-	-	2x2x2	1x1x1	0.5	1.5
NLSS	0.95	0.5	3x3x3	0.25	2x2x2	1x1x1	0.5	1.5

algorithm variations are shown in Table II-2.

Algorithm comparison was done using leave-one-out cross-validation, which generated 29 label volumes for each target image. The 29 propagated labels were then fused to obtain the segmentation for each structure. Quantitative accuracy was assessed using the DSC [100], Hausdorff distance (HD) [115], and mean surface distance (MSD). The HD metrics were computed symmetrically in terms of distance from the expert labels to the estimated segmentations and vice versa. All the fusion algorithm implementations are available in the Java Image Science Toolkit (JIST)[116, 117].

2.3. Evaluation Methods

The complete thyroid eye disease dataset was loaded into an institutional eXtensible Neuroimaging Toolkit (XNAT) archive [118] and the leading algorithm was executed fully automatically using all 30 manually labeled scan volumes as atlases. Following Figure II.2, each of the 30 manually labeled datasets was registered (warped) to match the unlabeled target image; statistical fusion was used to combine the registered labeled datasets from the atlas subject to form a label estimate for each target image. Out of the total 543 scan volumes there were 12 high-resolution scan volumes (0.3x0.3x0.4 mm) with large ON field of view, which were excluded from consideration due to technical constraints, such as cluster memory and wall-time settings. From the remaining 531 scan volumes, 30 were used for training and algorithm development and were therefore excluded from algorithm evaluation. In total, the algorithm is evaluated on 501 scan volumes. Note that all labeling was performed on 3-D volumes.

The volumes of the automatic segmentations were calculated for the ON and the eye globe structure to identify outliers. To isolate the outliers we plot the label volumes of the 501 automatically segmented volumes and the 30 manually segmented volumes against the slice thickness, which serves as a proxy for image quality.

To further evaluate the accuracy of the results, we performed principal component analysis (PCA)[119] on the images. All 501 test scan volumes and the 30 manually labeled atlases were affine registered to a common quality analysis space (one of the initial scan volumes) for comparison. Using the

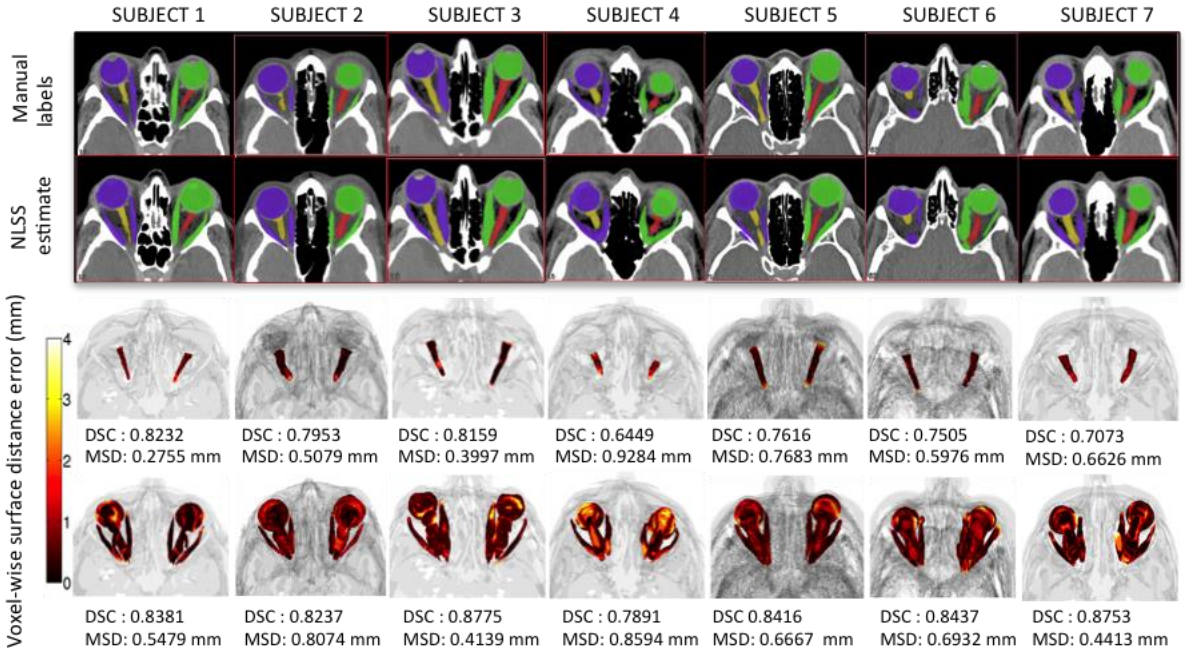

Figure II.5. Qualitative results for the optimal multi-atlas segmentation approach for 7 subjects are shown. For a typical subject, the top rows compare manual and automatic results for a representative 2D slice. The bottom rows show point-wise surface distance error of the label fusion estimate for the ONs and the eye globe structure. The proposed multi-atlas pipeline results are reasonable accurate segmentations. However, slight over segmentations of the ON can be observed in certain cases (subjects 4 and 7) supporting the results in the volumetry section (Figure II.4).

centroid of these labels, all the images were cropped around the ON ROI. PCA was then performed using two approaches. First, PCA was performed on the central two slices of the registered intensity images (i.e., where the ON was present) and the first several modes were visually investigated. Second, the label sets on the registered images were transformed into level sets via Euclidean distance transform on two central slices and PCA was performed on the slice-wise level sets. Finally, all automatic segmentations were manually examined to identify any other segmentation failures.

3. Results

Table II-3 Performance statistics of NLSS fusion and SyN diffeomorphic ANTs registration

Region	DSC			MSD			HD		
	Mean	Median	Range	Mean	Median	Range	Mean	Median	Range
ON	0.74	0.77	0.41	0.64	0.55	2.03	3.75	3.33	6.86
Globes/muscle	0.84	0.86	0.19	0.62	0.58	0.78	5.27	5.04	4.74

3.1. Development Results

The accuracy of various permutations of registration methods followed by label fusion algorithms was evaluated using leave-one-out approach over the 30 ground truth images. Quantitative results of this comparison are presented in Figure II.3 for the three different structures considered (ON, globes, and muscle). SyN ANTS registration followed by NLSS label fusion provided the most consistent results with a median DSC of 0.77 for the ON. Complete results of DSC, HD and MSD can be seen in Table II-3. Detailed statistics characterizing all of the approaches are summarized in Table II-5**.** The optimal combination of registration and label fusion (ANTs SyN + NLSS) can be clearly seen to outperform all other combinations in the last column of Table II-5. The ONs were segmented with approximately ±20% accuracy by volume whereas the globes and muscles were more stable with ±12.5% accuracy by volume

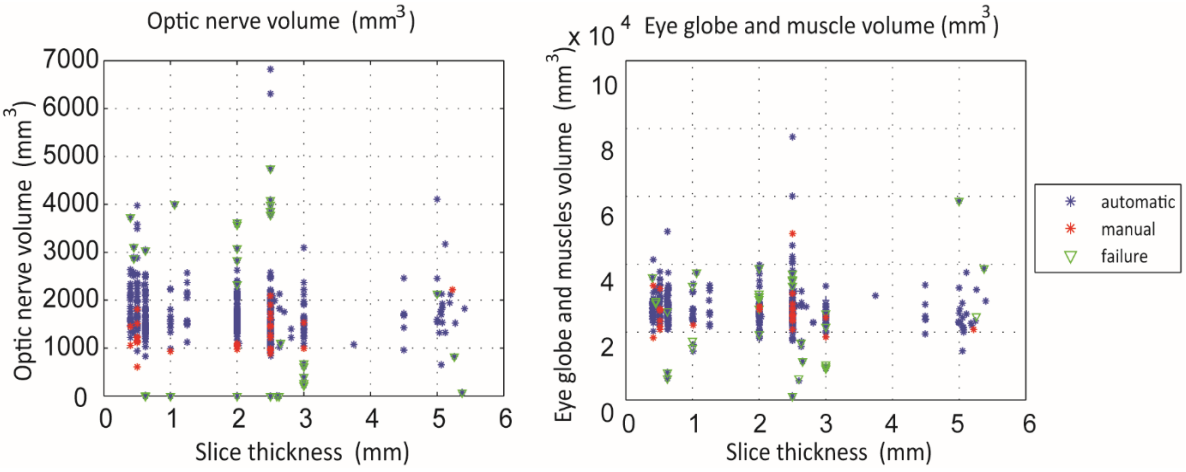

Figure II.6. Scatter plots of the automatic segmentation volumes for ONs and the eye globe structure and label volumes plotted against the slice thickness.

(Figure II.4 and Figure II.5). There was a slight tendency for over-segmentation, as noted by the positive bias in nerve volumes and visibly larger nerve boundaries compared to the manual segmentations in Figure II.4.

3.2. Inter-rater Reproducibility

A subset of 15 images with similar variability in slice thicknesses as in the original dataset was selected from the manually labeled atlas, for assessing inter-rater reproducibility. Each of these scan volumes was labeled by a second experienced rater and the segmentations were compared using DSC, HD, MSD, and relative volume difference. Results can be seen in Table II-4.

3.3. Evaluation Results

The segmentations are evaluated by examining label volumes to identify outliers. Segmentations whose volumes are not similar to that of the rest of the segmentations and that of the manual atlases are likely to be outliers (extreme values) on the volume measurements and PCA maps. Figure II.6 shows failures as a function of ON volume and eye globe and muscle volume. Note that the algorithm was successful for the majority of scan volumes and failures have a tendency to occur at the extremes.

Results from the first PCA analysis, using intensity images, can be seen in Figure II.7a. Results

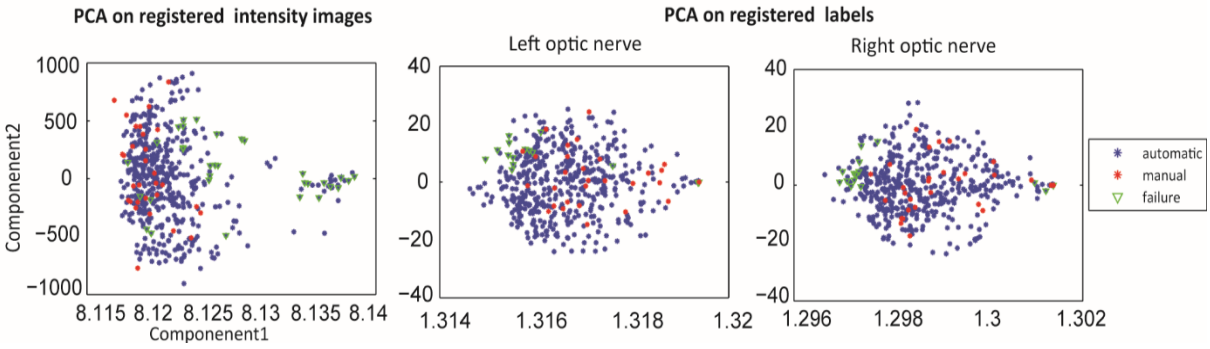

Figure II.7. Principal component analysis after registration to a common space on the intensity values and left and right ON labels.

from the second PCA analysis, using registered labels, can be seen in Figure II.7b and Figure II.7c for the left and right ON labels respectively. Failures, cases in which the segmentation produced undesirable results, are marked in green. Both methods of performing PCA clustered failures as outliers. PCA on the label level sets distinguished more outliers. Note that one of the scan volumes of the initial 30 atlases with >5 mm slice thickness was poorly registered and appeared as an outlier; however, this image resulted in a reasonable segmentation.

All automatic segmentations were manually examined to identify 33 failed segmentations; these failures were also apparent as outliers in the PCA analyses. Two subjects with tumors in the ON region resulted in over-segmentation in 17 of the 33 failure scans. Note that the 183 patients were retrieved by ICD code. The graduate student raters manually reviewed each of the automatically labeled datasets to determine if the algorithm resulted in catastrophic failures. For the failure cases, we reviewed the images with an ophthalmologist to identify the characteristics of the images that led to the failures. Failures could be grouped in one of four ways: (1) Two subjects with tumors in the ON region resulted in over-segmentation in 17 of the 33 failure scan volumes (Figure II.8a); (2) The ROI cropping failed in 2 of the 33 failures due to extreme rotation of the image during acquisition, as our cropping direction was only along the horizontal and vertical axes (Figure II.8b); (3) Scan volumes with excessively large field of view (included the abdomen/pelvis, 12 of the 33 scan volumes) were not properly affine registered to the atlases resulting in incorrect segmentations (Figure II.8c); (4) 2 of the 33 failed datasets were found to be

Table II-4 Inter-rater reliability in terms of DSC, symmetric HD, symmetric MSD and relative volume difference metrics evaluated on 15 datasets with similar variability as in the original dataset

Region	DSC	HD (mm)	MSD (mm)	Relative Volume Difference
ON	0.73±0.042	2.90±0.485	0.49±0.107	0.27±0.205
Globes/muscle	0.85±0.027	4.94±0.613	0.54±0.151	0.11±0.067

missing the ON in the acquired field of view (Figure II.8d).

4. Discussion

The proposed multi-atlas segmentation pipeline provides consistent and accurate segmentations of the ON structure despite variable field of view and slice thickness encountered in clinically acquired data. Segmentation error is comparable to the inter-rater difference observed when different human raters manually label the structures. Human raters achieved a reliability DSC of 0.73 versus 0.77 for ANTS SyN and NLSS. Note that the proposed approach is similar to the best-reported performance of other ON segmentation algorithms on CT (with DSC ranging from 0.39 to 0.788). The primary advantage of this work is the focus on evaluation in the context of a large, retrospective clinical records study in which data acquisition was not standardized. Methods targeting "wild type" data are becoming increasingly important as imaging science seeks to leverage large archives of clinically available data that are individually acquired with standard of care, but have substantive variations in scanner hardware, acquisition configuration, and data reconstruction. This work builds upon previous algorithms by showing that the robust registration framework is able to consistently handle the high variability of clinical data

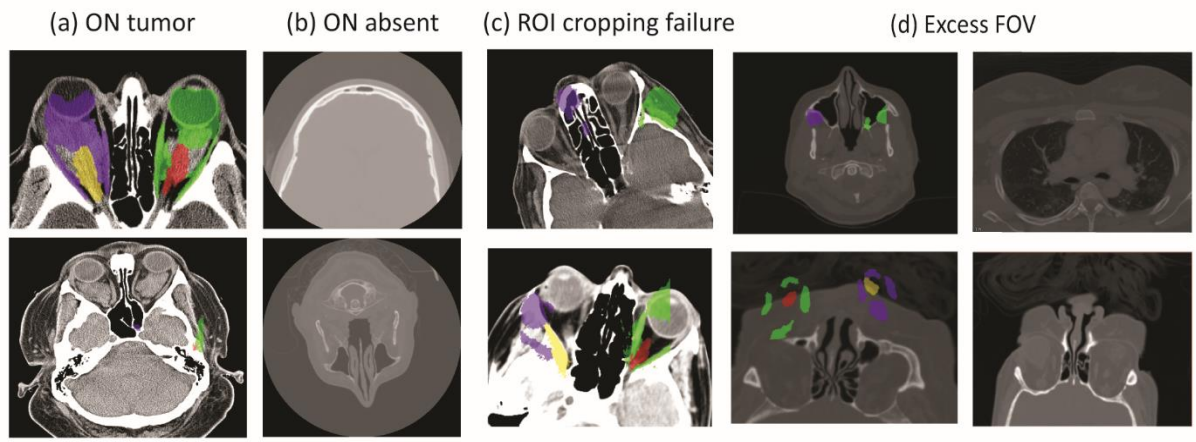

Figure II.8. The 33 outlier scan volumes identified were either due to the presence of a tumor (a), missing ON slices (b), ROI cropping failure in case of extreme rotation of the image during acquisition (c), or excess field of view (including abdominal organs)(d).

acquisition scope in terms of both field-of-view and voxel resolution. The “wild-type” success rate was 93.4% (468 of 501). None of the failure cases are especially worrying as the extremes of field of view (very large and missing the ON) and presence of orbital tumors were beyond the design criteria. The proposed approach could be used to provide analysis context (i.e., navigation), volumetric assessment or enable regional nerve characterization (i.e., localize changes).

There are opportunities for further algorithm refinements using the recent advances in segmentation post-processing such as incorporation of shape priors in the label fusion estimation framework, intensity-based refinement [120], or learning based correction of mislabeled voxels [121]. Other areas that could be improved include increasing algorithm robustness to reduce the number of failures, including a segmentation of the optic chiasm (which is of interest in many applications) and simplifying the pipeline to reduce computation time.

Table II-5 Statistical assessment of the performance of various registration and label fusion algorithms. Significance was assessed by two-sided Wilcoxen Signed Rank Test. Upper quadrant shows DSC. Lower quadrant shows Hausdorff distance for the Optic Nerve.

Blue * symbols show column > row (* p<0.05, ** p<0.01). Green + symbols show row > column. + p<0.05, ++ p<0.01).

	NR_MV	ART_MV	ANTS_MV	NR_STAPLE	ART_STAPLE	ANTS_STAPLE	NR_SPSTAPLE	ART_SPSTAPLE	ANTS_SPSTAPLE	NR_LWV	ART_LWV	ANTS_LWV	NR_NLS	ART_NLS	ANTS_NLS	NR_NLSS	ART_NLSS	ANTS_NLSS
NR_MV		+	**	++	++				**	**		**	*			**	**	**
ART_MV			**	+	++		*	**	**	**	**	**	**	**	**	**	**	**
ANTS_MV	**	**		++	++	++	++	++	++	++	++	**	+	++	++			
NR_STAPLE	++	++	++		++	**	**	**	**	**	**	**	**	**	**	**	**	**
ART_STAPLE	++	++	++			**	**	**	**	**	**	**	**	**	**	**	**	**
ANTS_STAPLE	++	++	++	**	**		**	**	**	**	*	**	**	**	**	**	**	**
NR_SPSTAPLE	+		++	**	**	**			**	**		**	**	*	**	**	**	**
ART_SPSTAPLE			++	**	**	**			**	*		**	**	**	**	**	**	**
ANTS_SPSTAPLE		*		**	**	**	**	**			++	**		+	+			**
NR_LWV			++	**	**	**			**		*	**				**	**	**
ART_LWV		*	++	**	**	**						**	*		*	**	**	**
ANTS_LWV		*		**	**	**	*	*		**	*		++	++	++			
NR_NLS	++		++	**	**	**			++			+				**	**	**
ART_NLS		+	++	**	**	*		+	++		++	++				**	**	**
ANTS_NLS			++	**	**	**			++			+		*		*	**	**
NR_NLSS			+	**	**	**	**			*			**	*				
ART_NLSS		**	+	**	**	**	**	*		*	*		**	**				*
ANTS_NLSS																		

Chapter III. Disambiguating the Optic Nerve and CSF Sheath

1. Introduction

Optic neuritis, from demyelination, is a sudden inflammation of the optic nerve (ON) and is marked by pain upon eye movement, and visual symptoms such as a decrease in visual acuity, color vision, contrast and visual field defects [122]. Demyelinating optic neuritis is closely linked with multiple sclerosis (MS) and many patients who present with optic neuritis will develop MS within 15 years [1]. The optic nerve treatment trial showed that the majority of patients, but not all, recover vision after an episode of unilateral optic neuritis [1]. Despite this, there is no current radiological biomarker of the ON that is well suited to predicting the visual outcome or even the eventual development of MS or can adequately characterize tissue evolution (axonal loss, atrophy) after an event of optic neuritis. Furthermore, therapeutic interventions can potentially help preserve and/or restore visual function if administered before ON axons are lost, i.e., during the 'neuroplasticity' window [4, 123, 124]. It would be beneficial to understand the relationship between ON damage and diseases of the central nervous system, such as MS. However, characterization along the length of the ON still remains challenging. Visually, high-resolution MRI methods have been developed to provide an appreciation of the ON in health (Figure II.2A) and in disease (Figure II.2B). The zoomed, coronal reformatted images in Figure II.2 also show that in patients with remote optic neuritis (Figure II.2B inset), tissue atrophy is noted compared to the healthy nerve (Figure II.2A inset). However, quantification of the degree of atrophy and even the distribution of expected, normal and healthy optic nerve sizes has not been well characterized. Therefore, the goal of this work is to develop an automated tool to measure the size of the ON and the surrounding cerebrospinal fluid (CSF) independently for estimating normal population variation and comparison among patient populations.

Optical computed tomography (OCT) is an important biomarker for visual pathologies; yet, OCT only captures the retinal nerve fiber layer at the back of the retina [125]. In fact, from OCT we understand the magnitude of axonal loss in optic neuritis [126] and the relationship with visual loss [127, 128]. We further hypothesize that gaining information about ON damage along the entire length of the nerve will give insight to "normal" areas of the nerve, and areas that are either at risk or already undergoing atrophy. Thus, 3D imaging techniques may offer a better platform for understanding disease pathology along the length of the ON but high-resolution imaging of the entire ON is challenging due to the small size and propensity for artifacts that arise from eye movement and orbital fat. Thus, data derived from MR and CT are largely used to identify lesions qualitatively (i.e., absence or presence enhancement) or marked with limited quantitative measures (i.e., single-slice cross-sectional area).

Manual segmentation with "computer assistance" has been, and remains, the *de facto* standard process to quantitatively characterize the ON using MRI. Hickman et al. used contouring to identify ON cross-sections in a longitudinal analysis and revealed patterns consistent with acute inflammation followed by long-term atrophy [51, 52]. Combined conventional and magnetization transfer (MT) imaging studies using manual contouring of the ON volume have shown that ON degeneration is associated with persistent functional deficits [129]. These studies have focused on ROIs consisting of the

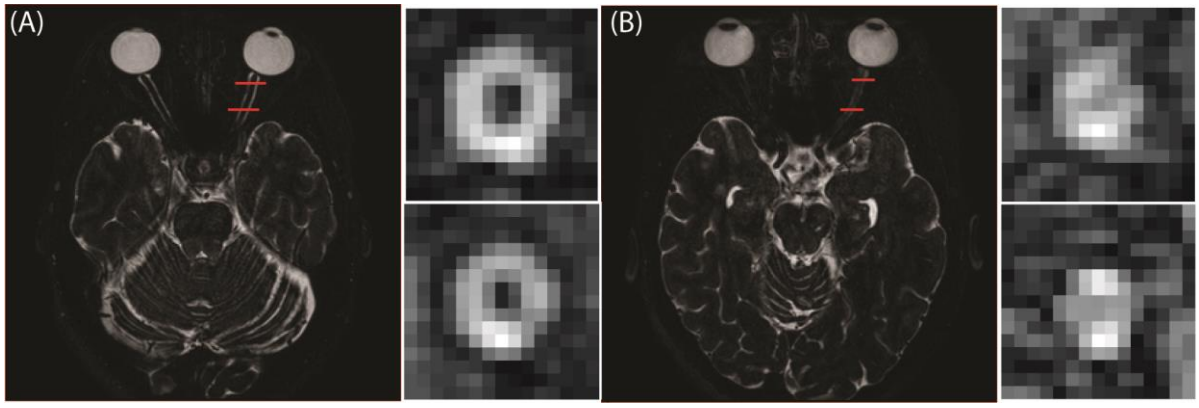

Figure III.1. An example of a healthy nerve (A) and an atrophied nerve (B) from the multi-atlas segmentation atlas subjects. In the coronal view, ON atrophy is apparent. Quantification of these structural difference is the target of the presented algorithm.

whole ON rather than capturing the cross-sectional variation along the entire tract. Shen et al. suggest limiting consideration to a single ON cross-section to limit resource requirements [130]. Meanwhile, work toward automating segmentation of the ON has developed in the context of radiation therapy using CT. Early "atlas–based" techniques [131, 132] were mildly successful for segmenting the ON [100]. To improve sensitivity and specificity, Bekes et al. [133] proposed a geometric method for semi-automatic ON segmentation, but indicated qualitative disagreements with expertly drawn labels. MRI has recently provided images whereby estimates of the ON and the surrounding CSF using manual observers have been accurate [134]; we seek to automate this process. Recent efforts have also attempted to automatically segment the ON in MRI but did not isolate the nerve from the surrounding CSF or study the application in patients with expected ON atrophy [135]. Recently, we have proposed multi-atlas segmentation pipelines for both CT [136] and MRI[137]. The surrounding CSF is not differentiable from the nerve on CT, which is why we choose to focus this effort on high-resolution MRI, which when using a heavily T2-weighted, fat-saturated acquisition can visualize the dark optic nerve and surrounding CSF clearly (Figure II.2). We therefore, optimize and evaluate an MRI imaging sequence to optimize ON-CSF contrast and propose an analysis pipeline that 1) segments both the ON and CSF sheath together from the surrounding tissue, and 2) separates the nerve and CSF into two classes using intensity value information couched in a novel model of ON architecture. Importantly, this model takes into account the orientation of the optic nerve which may be oblique to the actual imaging plane.

2. Imaging

2.1. Sequence Design

We developed and optimized a high-resolution 3-D isotropic turbo spin echo (TSE) with asymmetric k-space sampling (VISTA) with parameters empirically optimized for ON-CSF contrast. This sequence addresses the size of the ON by having sufficiently high resolution in all three planes (≤0.6mm isotropic) and allows for accurate characterization of the ON and CSF. The use of a TSE sequence is

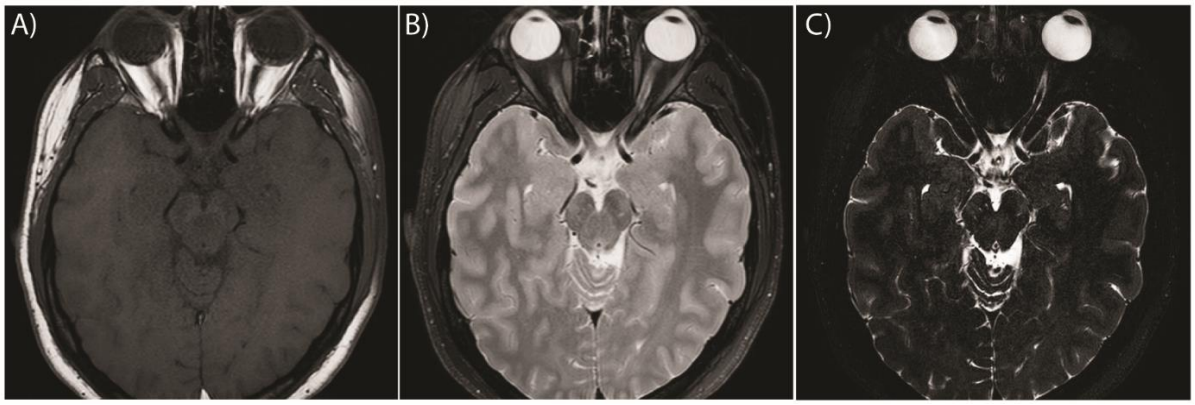

Figure III.2. Comparison of the clinical standard of care (A) T1W image, (B) T2W image and (C) our proposed high-resolution sequence for a single subject. Note that the resolution of the clinical standard of care yields one slice containing the ON, which is shown, while a medial slice was chosen for our proposed method (C)

inherently to B_0 inhomogeneities due to magnetic susceptibility caused by the bone-air interface of the maxillary sinuses, while asymmetrically sampling k-space blurs any ON motion across k-space. The result is a sequence which accurately captures variations in the hostile imaging environment of the ON. This sequence is also optimized for CSF-ON contrast as well as CSF-Fat contrast. We use a SPIR fat suppression technique to minimize fat signal and maximize CSF-Fat contrast. We utilize an extended echo train which leads to a long effective TE and provides good signal in the CSF while suppressing signal within the ON and any remaining fat signal, such as olefinic fat, that has not already been suppressed with the SPIR.

2.2. Validation

To validate the proposed imaging sequence we compare the contrast-to-noise ratio (CNR) of our proposed VISTA sequence and current clinical standard of care for contrast between both ON-CSF and CSF-Fat. We show that our proposed sequence is far superior at achieving ON-CSF contrast to the current clinical standard of care while achieving 11 fold higher resolution.

2.2.1. Data Acquisition

Ten healthy subjects age 24 to 36 years (average: 28.25, median: 27 years, 6 male/4 female) were

enrolled in the imaging study. Imaging was acquired on a 3T Philips Achieva (Philips Medical Systems, Best, The Netherlands) with a 2-channel body coil for transmission and an 8 channel head coil for reception for all sequences. After tri-planar localization, we acquired the all volumes in the axial plane. The VISTA sequence parameters were: 3D TSE TR = 4000ms, TE = 455ms, α = 90°, FOV= 180 x 180 x 20mm^3, acquired resolution = 0.55 x 0.55 x 0.55mm^3, reconstructed resolution = 0.35 x 0.35 x 0.35mm^3, SENSE factor = 2, fat saturation = SPIR, NSA=2 and total scan time = 7:48. For comparison a clinical standard of care T1-weighted (T1W) image was also acquired with parameters: SE TR=400ms, TE=12ms, α = 90°, FOV= 180 x 180 x 33mm^3, acquired resolution = 0.70 x 0.88 x 3.0mm^3, reconstructed resolution = 0.42 x 0.42 x 3.0mm^3, and total scan time = 3:20. A clinical standard of care T2-weighted (T2W) image was also acquired with parameters: TSE TR=3000ms, TE=80ms, α = 90°, FOV= 180 x 180 x 33mm^3, acquired resolution = 0.70 x 0.88 x 3.0mm^3, reconstructed resolution = 0.42 x 0.42 x 3.0mm^3, fat suppression=SPIR and total scan time = 2:48. Subjects were scanned with a baseline scan and again within 30 days of the original scan for short-term reproducibility. Inter-scan time was from 4 to 29 days (average: 19.4 days, median: 23 days). Figure III.2 shows the clinical standard of care T1W image (A), T2W image (B) and our optimized imaging method (C). Note the increased contrast between the CSF and ON in our optimized imaging as compared to the standard of care T2W image. The T1W image shows no contrast between CSF and ON, only the ON-Fat boundary is visible.

2.2.2. Data Analysis

To quantitatively compare the three sequences, contrast-to-noise ratio (CNR) was investigated for each of the three sequences for CSF-ON contrast and CSF-Fat contrast. Note that since the CSF-ON boundary is not visible on the T1W images (Figure III.1A), this comparison was only made for the clinical T2W sequence and our VISTA sequence. CNR is defined as:

$$CNR = \frac{|S_a - S_b|}{\sigma} \quad \text{(III.1)}$$

where S_a is the mean the signal from tissue a, S_b is the mean signal from tissue b and σ is the image noise. Regions of interest (ROIs) were drawn on each scan (T1W, T2W and VISTA) for each of the 10 subjects for both the baseline and short term follow up scans. An ROI was drawn in a homogenous area of white matter in the temporal lobe, and the standard deviation of intensity values within this ROI was taken as an estimate of image noise (σ). ROIs were then drawn such that they encompassed as many pure voxels of each of ON, CSF and orbital fat from a medial ON slice. The mean voxel intensity of each of these ROIs was then taken as the mean signal from that tissue.

2.2.3. Results

Figure III.3 shows the results of the CNR analysis for the CSF-Fat contrast (left) and the ON-CSF contrast (right). We can see that the T1W sequence has significantly higher CNR for the CSF-Fat boundary than the T2W or VISTA sequences (Wilcoxon rank-sum test; $p<0.01$). The T2W and VISTA both have similar but sufficient CNR to distinguish CSF and orbital fat, due to the SPIR fat suppression. The ON-CSF boundary is indistinguishable in the T1W imaging and is therefore excluded from

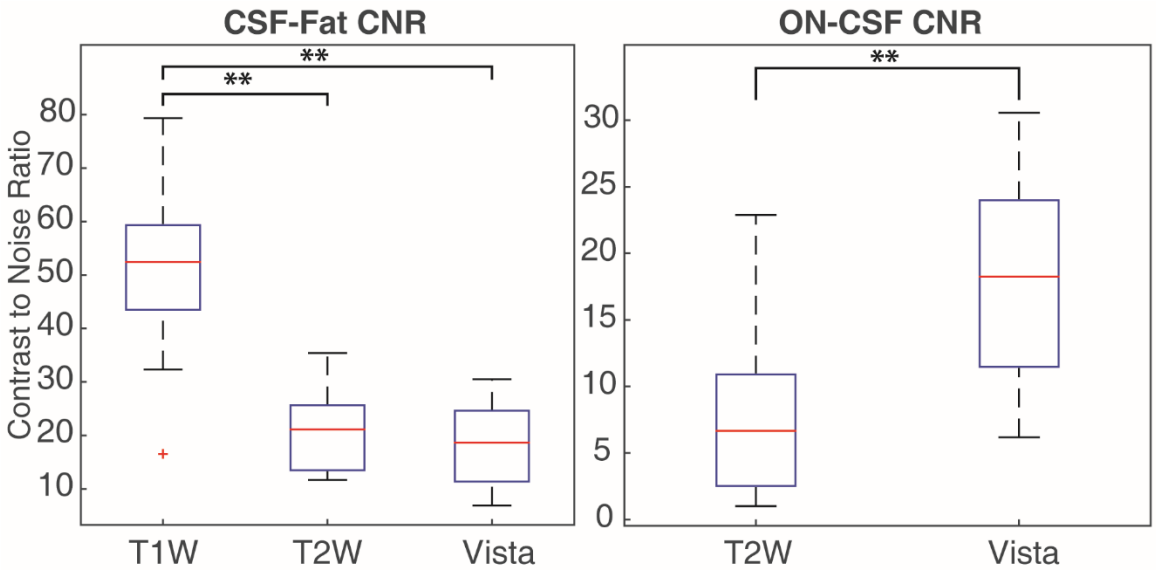

Figure III.3. Contrast-to-noise ratio (CNR) comparison for contrast between CSF-Fat (left) and ON-CSF (right) for the clinical standard of care T1W, T2W and the optimized VISTA sequence. ** indicates the results are significantly different by Wilcoxon rank-sum test at p<0.01.

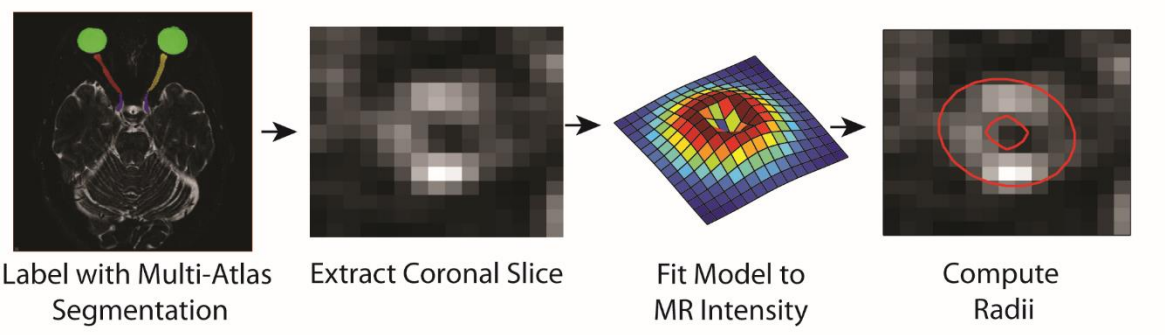

Figure III.4. The proposed algorithm for ON radii extraction. Multi-Atlas segmentation is used to locate the ON and sheath as a single labeled object. Using this result, we use the fact that the data are acquired isotropically to switch to a coronal plane where the proposed model is fit. The parameters are found through this model fitting, and then fed into a nonlinear regression tree to extract the underlying radii.

comparison. The VISTA sequence has significantly superior CNR to the clinical T2W sequence (Wilcoxon rank-sum test; $p<0.01$). The Rose criterion states that if the CNR is below 3-5, two structures become difficult to distinguish [138]. These results suggest the ON-CSF contrast is often difficult to distinguish on clinical T2W while the proposed VISTA CNR is well above this criterion.

2.2.4. Discussion

We have demonstrated the superiority of our proposed VISTA sequence in characterizing the ON and in generating contrast between ON and CSF. This sequence has ON-CSF CNR that is consistently above the Rose criterion and therefore more consistent in accurately visualizing the ON as compared to a current clinical standard of care with 11.1 fold higher volumetric resolution than the clinical sequence. This high contrast in conjunction with the isotropic high resolution of this sequence allows for characterization of the size and shape of the ON along the length of the ON, which was previously not possible. The improved imaging facilitates automated processing and algorithm development.

3. Analysis

3.1. MRI Acquisition and Summary of Analysis Approach

All MRI studies were performed with approval of the Vanderbilt Institutional Review Board and

signed informed consent was obtained prior to data acquisition. Six healthy volunteers and 6 patients with multiple sclerosis concomitant with a noted clinical history of at least unilateral optic neuritis were enrolled in the study. Anatomical T2-weighted VISTA scans were obtained on a 3T Philips Achieva (Philips Medical Systems, Best, The Netherlands) using a 2 channel body coil for transmission and an 8 channel head coil for reception. After tri-planar localization, we acquired the T2-weighted volume in the axial plane. The VISTA sequence parameters were: 3D FSE (TR/TE/α = 4000ms/404ms/90°), FOV= 180 x 180 x 42mm^3, nominal resolution = 0.6 x 0.6 x 0.6mm^3, SENSE factor = 2, fat saturation = SPIR, and total scan time = 5:20. It should be noted that the TE is long due to the nature of the asymmetrically sampled k-space pattern of the VISTA (SPACE on Siemens, and CUBE on GE) acquisition but does provide excellent tissue:CSF contrast. We reformatted the data into the coronal plane and propose a model to fit the ON and surrounding CSF in the reformatted plane. The model is initialized using the

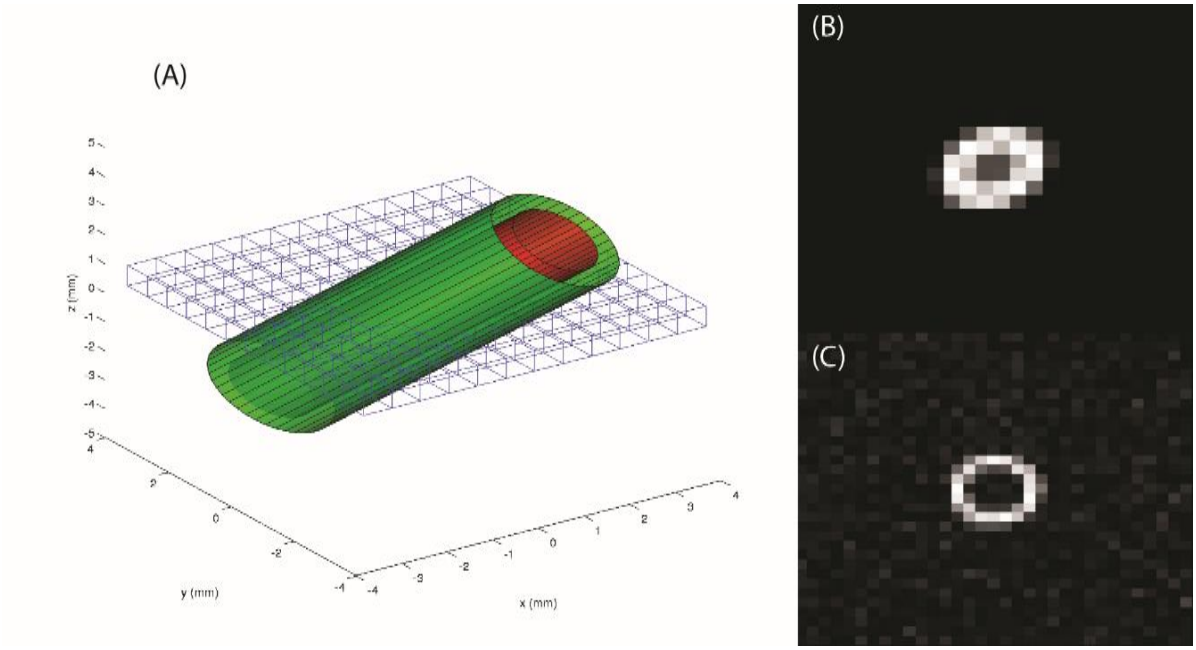

Figure III.5. Some examples of the model used to generate synthetic images. (A) shows a rendering of the model and how the imaging plane crosses the tubular structure creating an elliptical structure in the image. (B) illustrates an example synthetic image with no noise added and slight off axis rotation. (C) presents an example synthetic image which is on axis (with Rician noise).

result of a previously described multi-atlas segmentation protocol [137]. We then fit the model to the ON using a conjugate gradient descent non-convex optimization method. A graphic outline of our proposed pipeline can be seen in Figure III.4.

3.2. Proposed Model

To first approximation, the ON can be thought of as a cylinder (~2-4 mm diameter) inside a cylindrical sheath (~3-6 mm diameter), which is imaged at an oblique angle. On T2-weighted MRI, CSF is brighter than nerve tissue such that the outer cylinder is white and the inner cylinder dark. Even using high-resolution methods as those proposed here with isotropic resolution ~0.6 mm, there are only a handful of voxels that span the ON (4-7) which are significantly partial volumed such that the resulting images appear to be blurred elliptical annuli (Figure III.5).

We propose a difference of two Gaussians model to fit the intensity values of the ON and CSF sheath in the coronal plane.

$$\hat{I}(x,y) = I_0\left[N\left(\vec{\mu},\Sigma_{xy}\right) - e^{\beta}\, N\left(\vec{\mu},\sigma_2\Sigma_{xy}\right)\right] \tag{III.2}$$

where $N\left(\vec{\mu},\Sigma_{xy}\right)$ is a bivariate normal distribution with mean vector $\vec{\mu} = [\mu_x \quad \mu_y]$ and covariance matrix Σ_{xy}:

$$N\left(\vec{\mu},\Sigma_{xy}\right) = \frac{1}{2\pi\left|\Sigma_{xy}\right|}\exp\left[-\frac{1}{2}(X-\mu)^T\Sigma_{xy}^{-1}(X-\mu)\right] \tag{III.3}$$

I_0 is an intensity scaling factor, e^{β} is a scaling factor to control the relative height of the inner Gaussian. Formulating the scaling factor as an exponential constrains the scaling term from becoming negative and forces the model to be a sum of Gaussians (rather than a difference) during optimization. σ_2 scales the covariance matrix to change the relative width of the inner Gaussian. The covariance matrix is comprised of the following components:

$$\Sigma_{xy} = \begin{bmatrix} \sigma_x & \sigma_x\sigma_y\left(\frac{2}{1+e^{-\rho}} - 1\right) \\ \sigma_x\sigma_y\left(\frac{2}{1+e^{-\rho}} - 1\right) & \sigma_y \end{bmatrix} \quad \text{(III.4)}$$

σ_x and σ_y control the width of the model in the x and y direction respectively. $2/(1+e^{-\rho}) - 1$ is a correlation term which allows for ellipticity in the model. This is necessary due to the fact that the ON is not always perpendicular to the imaging plane and thus appears elliptical (Figure III.5A) and heavily partial volumed (Figure III.5B) compared to the true coronal (Figure III.5C). This term is formulated as a sigmoid function such that the correlation is constrained in the range (-1,1), which improves stability during optimization.

In summary, the complete model is composed of eight terms: $\Theta = \left[\sigma_x, \sigma_y, \sigma_2, I_0, \mu_x, \mu_y, \beta, \rho\right]$. Model error is defined as the sum of squared error between the model and the observed image in Equation (III.5). Equation (III.6) is the derivative of the sum of squared error with respect to the set of parameters Θ.

$$\varepsilon = \sum \left(I(x,y) - \hat{I}(x,y)\right)^2 \quad \text{(III.5)}$$

$$\frac{\delta\varepsilon}{\delta\Theta} = 2\sum_{xy}\left(I(x,y) - \hat{\mathrm{I}}(x,y)\right)\frac{-\partial\hat{\mathrm{I}}}{\partial\Theta} \quad \text{(III.6)}$$

For clarity, the partial derivatives for each parameter are shown in equations (III.7) through (III.12) and can then be used in Equation (III.6). The derivatives for σ_y and μ_y are omitted as they are a direct substitutions into equations (III.7) and (III.10), respectively.

$$\frac{\partial\hat{\mathrm{I}}}{\partial\sigma_x} = -\hat{\mathrm{I}}(x,y)\left[\frac{1}{\sigma_x} + \frac{\frac{(x-\mu_x)^2}{\sigma_x^3} + \frac{\rho(x-\mu_x)(y-\mu_y)}{\sigma_x^2\sigma_y}}{(1-\rho)}\right] \quad \text{(III.7)}$$

$$\frac{\partial\hat{\mathrm{I}}}{\partial\sigma_2} = \frac{-N_2}{\sigma_2}\left[2 + \frac{(X-\vec{\mu})^T\Sigma_{xy}^{-1}(X-\vec{\mu})}{(1-\rho)}\right] \quad \text{(III.8)}$$

$$\frac{\partial\hat{\mathrm{I}}}{\partial I_0} = \frac{\hat{\mathrm{I}}(x,y)}{I_0} = N\left(\vec{\mu}, \Sigma_{xy}\right) - e^{\beta}\, N\left(\vec{\mu}, \sigma_2\Sigma_{xy}\right) \quad \text{(III.9)}$$

$$\frac{\partial \hat{\mathrm{I}}}{\partial \mu_x} = \frac{-\hat{\mathrm{I}}(x,y)}{(1-\rho)}\left[\frac{\rho(y-\mu_y)}{\sigma_x\sigma_y} - \frac{(x-\mu_x)}{\sigma_x^2}\right] \tag{III.10}$$

$$\frac{\partial \hat{\mathrm{I}}}{\partial \beta} = -I_0 e^{\beta} N\left(\vec{\mu}, \sigma_2 \Sigma_{xy}\right) \tag{III.11}$$

$$\frac{\partial \hat{\mathrm{I}}}{\partial \rho} = -\hat{\mathrm{I}}(x,y)\left[\frac{\rho}{1-\rho^2}\right] - \left[\frac{(x-\mu_x)(y-\mu_y)}{\rho\sigma_x\sigma_y} - 2\rho(X-\mu)^T\Sigma_{xy}^{-1}(X-\mu)\right] N\left(\vec{\mu}, \Sigma_{xy}\right) + \beta\left[\frac{(x-\mu_x)(y-\mu_y)}{\rho\sigma_x\sigma_y\sigma_2^2} - 2\rho(X-\mu)^T\sigma_2\Sigma_{xy}^{-1}(X-\mu)\right] N\left(\vec{\mu}, \sigma_2\Sigma_{xy}\right) \tag{III.12}$$

3.3. Initialization

The center of the model is initialized at the centroid of the multi-atlas segmentation labels in the coronal plane. To initialize σ_x and σ_y, profiles are taken superiorly and inferiorly across the image and two local peaks around the center of the ON labels are identified and used to estimate the spread in x and y as half the distance between the two peaks. If this fails, both parameters default to an initialization of 2. ρ is initialized by similarly finding intensity peaks along the two diagonals and measuring the width between the two peaks along each diagonal. ρ is then initialized as the difference between these two distances. We initialize σ_2 to the experimentally found value of 0.6. β is initialized such that the scaling term $e^{\beta} = 0.5$. Finally I_0 is found such that the maximum value of the model is equal to the maximum value of the input image.

3.4. Optimization

For every coronal slice that contained ON labels from the initial multi-atlas segmentation, the difference of Gaussian model is fit using an iterative conjugate gradient descent [81]. The input to the conjugate gradient descent algorithm is a patch which is 9x9 mm (15x15 voxels) centered at the centroid of the multi-atlas label. The non-linear optimization routine is a custom implementation in MATLAB R2013a (The MathWorks, Inc., Natick, MA, USA). Specific implementation details follow:

The patch is first normalized to the range (0,1). The gradient of the cost function is computed and its negative is used as the initial descent direction. The descent step size is found using a line search (iterative bracket search using cubic interpolation and bisection every fifth iteration). The line search is run for a total of 25 iterations. The step is taken and the conjugate direction is then chosen as the descent direction. Every eight iterations (because there are eight input parameters) the descent direction is reset to the negative gradient direction. Also, if the chosen direction is found to be an ascent direction, the direction is reset to the negative gradient. Convergence criteria: the magnitude of the gradient is less than 10^{-6}; the change in the cost function is less than 10^{-12} between iterations. (Note that small gradients and non-decreasing function values indicate proximity to function extrema.) Divergence criteria: algorithm exceeds 70 iterations; function values become increasing or undefined. If a divergence criteria is reached the algorithm is restarted (only once) using the last iteration as the initialization of the second attempt. This resets the search direction to the gradient descent direction, which can allow the optimization to bypass local minima.

3.5. Calibration

Synthetic data was generated to calibrate model parameters to the radius of the ON and surrounding CSF in physical space. A model of two concentric tubes was constructed (Figure III.5) and a Monte Carlo simulation is used to simulate partial volume effects. The test images simulate 0.6 mm isotropic voxels, which cover an area 30 mm by 30 mm (50x50 voxels). The model is rotated independently along x and y ranging from zero to 60 degrees rotation in 7.5 degree steps. The inner radius

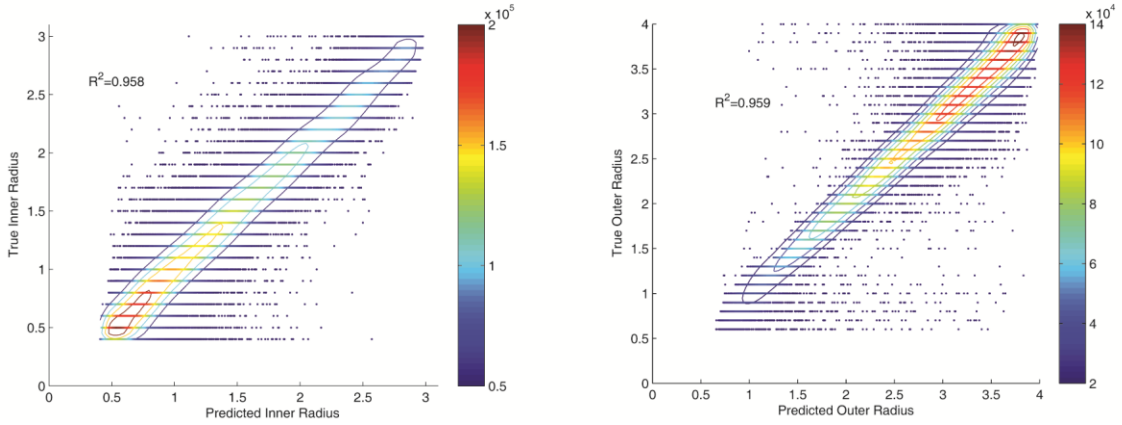

Figure III.6. Calibration results for the random forest regression for the inner and outer radii from one fold of a tenfold cross validation on the 1.2 million synthetic images. The color scale represents data density calculated within a circle of radius 0.1. A five element 2-D moving window median filter was applied for smoothing. The isocontours show lines of constant data density. Note that data density is higher near the lower end for the inner radius and at the higher end for the outer radius, this is due to the width constraint on the synthetic images.

is varied from 0.4 mm to 3 mm in 0.1 mm steps and the outer radius varies from 0.5 mm to 4 mm in 0.1 mm steps. The CSF thickness is constrained to be at least 0.20 mm. Twenty five levels of Rician noise [139] were simulated which were experimentally determined to be visually similar to those observed in ON images we have acquired. These combinations produced a training set of 1,250,964 images. Six model parameters $[\sigma_x, \sigma_y, \sigma_2, I_0, \beta, \rho]$ are correlated to surrounding CSF and ON radius measurements through a random forest regression [85]. The centroids are omitted as they are assumed to depend on field of view placement only.

3.6. Validation

To validate that the results obtained from the automatic segmentation match manual measurements, we acquired a higher resolution scan of a healthy control. We acquired a short-inversion time inversion recovery (STIR) scan with TR/TI/TE = 5000ms/200ms/33ms and 2 signal averages at 0.5 x 0.5mm^2 with 2 mm slice thickness. The image was reconstructed at 0.15 x 0.15 mm^2 for the measurements. This image was then down sampled to 0.6 mm isotropic and smoothed with a 5x5 voxel

Gaussian filter with standard deviation of 0.25 voxels. Our algorithm is then applied to the down sampled version to obtain an automatic measurement which can be compared to manual measurements made on the higher resolution scans.

3.7. Clinical Application

A small pilot study was conducted to evaluate the viability of this tool in differentiating diseased and healthy ONs. Six controls were chosen at random from a population of 47 and six patients with MS who have a concomitant clinical history of at least one unilateral optic neuritis event. We chose the MS patients who demonstrated poorest visual performance as determined by the adjusted 1.25% binocular contrast visual acuity. These patients were chosen from a pool of 32 MS patients. Each patient and control data set was acquired as in the methods. Using the outlined analysis approach and relying on multi-atlas segmentation for initialization [137] to locate the centroids of the ONs in the coronal plane and determine whether or not a slice contained ON tissue, we calculated the ON radii at every coronal slice. The slice-wise measurements were interpolated to be the same length as the longest observed ON. The nature of the ONs allows for them to be present in a different number of slices from volume to volume. Interpolation more closely aligns corresponding parts of the ON across subjects. A three-element moving window median filter is also applied across slices to reduce noise in the measurements.

4. Results

4.1. Calibration

Synthetic data was utilized to calibrate the model parameters of the radii of two concentric tubes using Monte Carlo simulation to examine the impact of partial volume effects. Tenfold cross validation was performed on a random forest regression using fifteen trees. Fifteen was found experimentally to be the point of diminishing returns (R2 improved by less than 0.01) with more trees and increased training time. The mean R^2 of the predicted versus actual result of the testing set is 0.959 for the outer radius

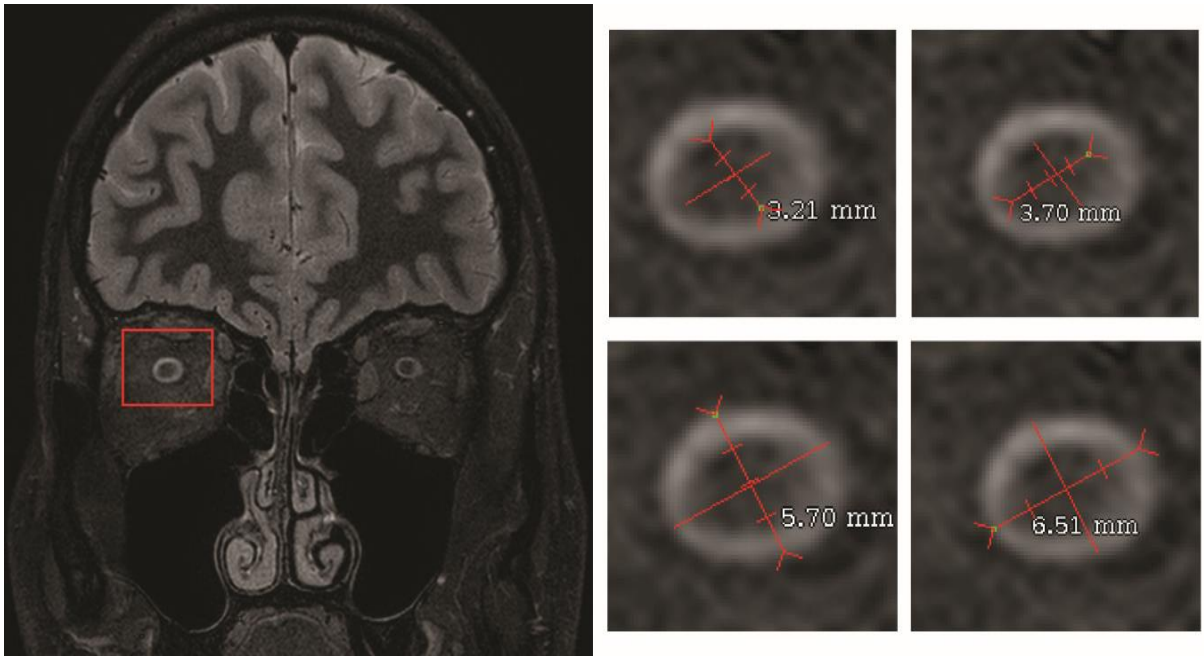

Figure III.7. The test volume slice used for validation is shown. The four images show the four measurements of inner and outer optic nerve diameter. This image was then down sampled and smoothed to match current in vivo imaging, and the proposed automatic measurement algorithm was applied. The automatic segmentation found the inner radius to be 1.673 mm and the outer radius to be 2.929 mm.

(CSF) and 0.958 for the inner radius (ON). The data density plots of these calibration results can be seen in Figure III.6. These plots show the correlation between the predicted and true underlying radius of the model. Finally, another forest of fifteen trees was built using all of the training data to be used on clinical data.

4.2. Validation

Validation proceeded by comparing manual measurement of the radii on high-resolution STIR acquisitions compared to the lower-resolution T2-weighted VISTA acquisition that was automatically segmented. Using the lower-resolution data, the automatic segmentation calculated the underlying inner radius (ON) to be 1.673 mm and the underlying outer radius (CSF) to be 2.929 mm. Using the STIR data (Figure III.7, left panel) Manual measurements were taken along the visually determined approximate major and minor axes for the inner and outer radii. Manually, the inner radius was measured at 1.605 mm

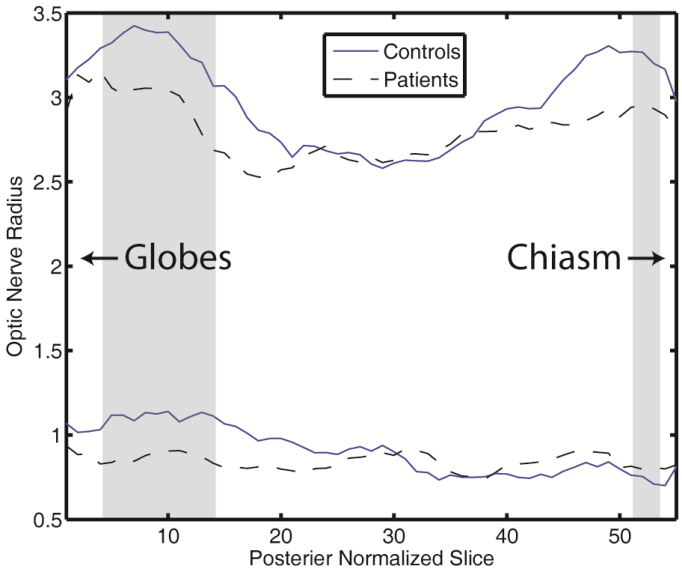

Figure III.8. Mean inner and outer optic nerve radii for the two six person sample populations tested interpolated to the same length as the longest sample. The shaded regions indicate where the outer radii are statistically different with p<0.05

and 1.855 mm and the outer radius was measured at 2.85 mm and 3.255 mm indicating close agreement with the automated approach. Details of the measurements can be seen in Figure III.7 right panels.

4.3. Clinical Application

We compared the average distribution of inner (ON) and outer (CSF) radii across a small cohort of healthy controls and MS patients with clinical history of optic neuritis. The distributions over slices of the two cohorts (healthy volunteers, dotted solid lines and MS patients, dotted lines) along the length of the ON and separated into outer (CSF) radius (top curves) and ON radius (bottom lines) are shown in Figure III.8. Statistically the profiles differ closest to the globe and chiasm and remain relatively similar across healthy volunteers and patients in the middle segments. The shaded areas indicate regions in which the radii of the two populations are statistically different using an unpaired two-sample t-test at $p<0.05$. It is important to note that the regions where the outer radii differ are similar to the where the inner radii differ. The inner radii have statistical difference only on slices nearer to the globe.

5. Discussion and Conclusions

This is a first demonstration that the ON can be automatically and quantitatively measured and separated from the surrounding CSF *in vivo* using MRI. In simulation, the model was found to have an explanatory R-squared for both ON and CSF radii of greater than 0.95. The accuracy of the method was

within the measurement error on the highest possible *in vivo* acquisition (Figure III.7). In the pilot study, significant structural differences were found near the ON head and the chiasm. Structurally, this is not surprising, as OCT has shown axonal loss near the ON head, which we identify as being an area of diminished ON radii. Very few studies have shown atrophy of the nerve proximal to the chiasm, which lends weight to the need for a high-resolution imaging method to survey the entire nerve.

There are a number of possible future directions that could lead to improved resolution and accuracy of the measurements. If the method were to be used on a different imaging resolution the model-physical space mapping would need to be recalibrated using an appropriate simulation framework. The current approach assumes that slices are independent which is a simplified framework and as such the measurements tend to be noisy across the length of the ON for an individual participant. In this work, we utilized a median filter to smooth this noise but constraining the model along the length of the nerve could address some of these issues and increase accuracy. More careful inter-slice analysis could improve model estimation and result in more accurate segmentation. Finally the curvature of the nerve could be better accounted for in the interpolation step along the entire length of the ON. The interpolation step currently assumes even samples along the length of every nerve which is not the case. If the curvature of the ON were characterized it would be possible to better align each measurement which may reveal new ways to differentiate patient populations. Future work will improve upon these techniques to better understand ON shape and size and how these vary among populations.

Chapter IV. Optic Nerve and CSF Sheath Size Short-Term Reproducibility and Variability of Optic Nerve and CSF Sheath Size within Young Healthy Controls

1. Introduction

The size of the optic nerve (ON) and cerebrospinal fluid (CSF) sheath have been manually measured [140, 141] previously and have been suggested as a differential diagnosis [142]. Optic neuritis is a sudden inflammation of the ON and is marked by pain on eye movement, and visual symptoms such as a decrease in visual acuity, color vision, contrast and visual field defects [122]. The ON is closely linked with multiple sclerosis (MS) and patients have a 50% chance of developing MS within 15 years [1]. Despite this, there is no radiological biomarker of the ON that predicts eventual development of MS. Furthermore, interventions can now help preserve and/or restore visual function if administered before ON axons are lost, i.e., during the 'neuroplasticity' window [4, 123, 124]. We hope to better understand ON disease etiology (including MS) using MRI to examine the ON anatomy along the length of the nerve.

Manual segmentation with "computer assistance" has been and remains the *de facto* standard process to characterize the ON on 3-D imaging. Hickman et al. used contouring to identify ON cross-sections in a longitudinal analysis and revealed patterns consistent with acute inflammation followed by long-term atrophy [51, 52]. We utilize a recently published method to automatically measure the optic nerve and CSF sheath [87]. We evaluate the short-term reproducibility of this method and then apply it to a population of healthy controls. From this population of healthy controls, we investigate any changes in ON size across demographics and build a normative distribution. As a preliminary analysis, we compare 6 MS patients with a history of optic neuritis to the normative distribution.

2. Methodology

2.1. Data

2.1.1. Short-Term Reproducibility

Ten healthy subjects age 24 to 36 years (average: 28.25, median: 27 years, 6 male/4 female) were enrolled in the imaging study. Imaging was acquired on a 3T Philips Achieva (Philips Medical Systems, Best, The Netherlands) with a 2-channel body coil for transmission and an 8 channel head coil for reception for all sequences. After tri-planar localization, we acquired the all volumes in the axial plane. The VISTA sequence parameters were: 3D FSE TR = 4000ms, TE = 455ms, $\alpha = 90°$, FOV= 180 x 180 x 20mm^3, acquired resolution = 0.55 x 0.55 x 0.55mm^3, reconstructed resolution = 0.35 x 0.35 x 0.35mm^3, SENSE factor = 2, fat saturation = SPIR, NSA=2 and total scan time = 7:48. For comparison a clinical standard of care T1 image was also acquired with parameters: SE TR=400ms, TE=12ms, $\alpha = 90°$, FOV= 180 x 180 x 33mm^3, acquired resolution = 0.70 x 0.88 x 3.0mm^3, reconstructed resolution = 0.42 x 0.42 x 3.0mm^3, and total scan time = 3:20. A clinical standard of care T2 image was also acquired with parameters: TSE TR=3000ms, TE=80ms, $\alpha = 90°$, FOV= 180 x 180 x 33mm^3, acquired resolution = 0.70 x 0.88 x 3.0mm^3, reconstructed resolution = 0.42 x 0.42 x 3.0mm^3, fat suppression=SPIR and total scan time = 2:48. Subjects were scanned with a baseline scan and again within 30 days of the original scan for short-term reproducibility. Inter-scan time was from 4 to 29 days (average: 19.4 days, median: 23 days).

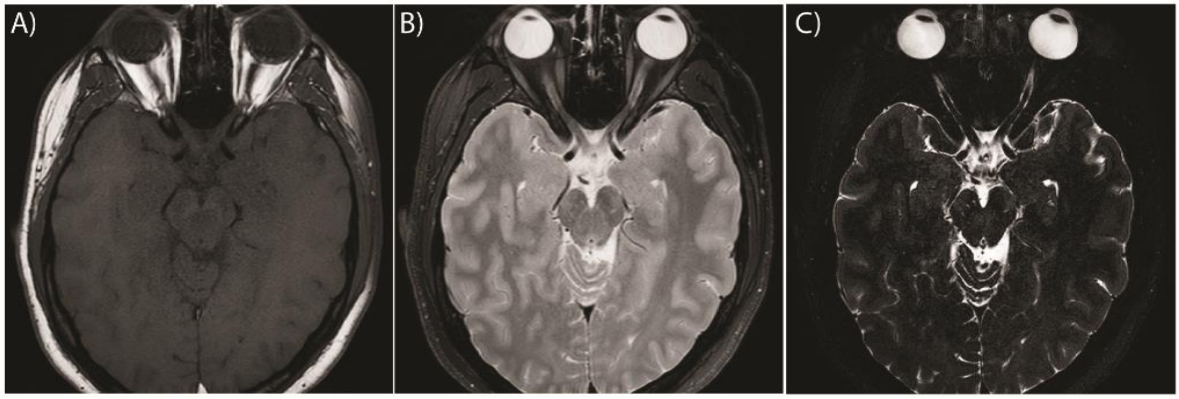

Figure IV.1. Comparison of the clinical standard of care (A) T1 image, (B) T2 image and (C) our proposed high-resolution sequence for a single subject. Note that the resolution of the clinical standard of care yields one slice containing the ON, which is shown, while a medial slice was chosen for our proposed method (C),

Table IV-1 Age demographic information for the 45 controls and six patients

	Controls: 45					Patients: 6				
	20-25	**25-30**	**30-35**	**Over 35**	**Total**	**20-25**	**25-30**	**30-35**	**Over 35**	**Total**
Male	5	12	3	1	21	0	0	1	0	1
Female	11	1	10	2	24	1	1	3	0	5
Total	16	13	13	3	45	1	1	4	0	6

Figure IV.1 shows the clinical standard of care T1 image (A), T2 image (B) and our optimized imaging method (C). Note the increased contrast between the CSF and ON in our optimized imaging as compared to the standard of care T2 image. The T1 image shows no contrast between CSF and ON, only the ON-Fat boundary is visible.

2.1.2. Demographics Analysis

2.1.3. Data acquisition

Anatomical T2-weighted VISTA scans were obtained on a 3T Philips Achieva (Philips Medical Systems, Best, The Netherlands) using a 2 channel body coil for transmission and an 8 channel head coil for reception. After tri-planar localization, we acquired the T2-weighted volume in the axial plane. The VISTA sequence parameters were: 3D FSE (TR/TE/a = 4000ms/404ms/90), FOV= 180 x 180 x 42mm3, nominal resolution = 0.6 x 0.6 x 0.6mm3, SENSE factor = 2, fat saturation = SPIR, and total scan time = 5:20. It should be noted that the TE is exceptionally long due to the nature of the asymmetrically sampled k-space pattern of the VISTA (SPACE on Siemens, and CUBE on GE) acquisition.

2.1.4. Demographic Information

Our control population consists of 45 individuals which are young adults with good representation of both male and female subjects. Six relapse-remitting MS patients with optic neuritis were selected to have the worst binocular 1.25% contrast visual acuity to assess whether they were different from the normative distribution.

2.2. Analysis

Our segmentation begins with a previously described multi-atlas segmentation method [86] which automatically segments the orbits, optic chiasm and ON. This method uses 35 manually labeled atlas images which include both healthy controls as well as drusen and MS patients. The target image to be segmented is registered to each of the 35 atlas images using an affine registration and non-rigid registration [143]. The manual labels of the atlas images are then transformed to the target space using these registrations and are fused using non-local spatial STAPLE[114, 144]. The segmentation of the ON includes both the ON and CSF sheath and so we must refine our segmentation to separate the two structures and measure them independently.

We utilize a previously described model [145] to fit the ON and CSF sheath in the coronal plane and extract the radii of both. The model is a difference of two Gaussian distributions which matches the intensity profile of the ON in the coronal plane. The second Gaussian is scaled by an exponential term and has a scaling factor on the covariance matrix in the range (0,1) such that the second Gaussian is always smaller than the first Gaussian. The covariance matrix is formulated with the correlation term as a sigmoid function to improve stability later on, during the optimization process.

The model is initialized using the result of a previously described multi-atlas segmentation

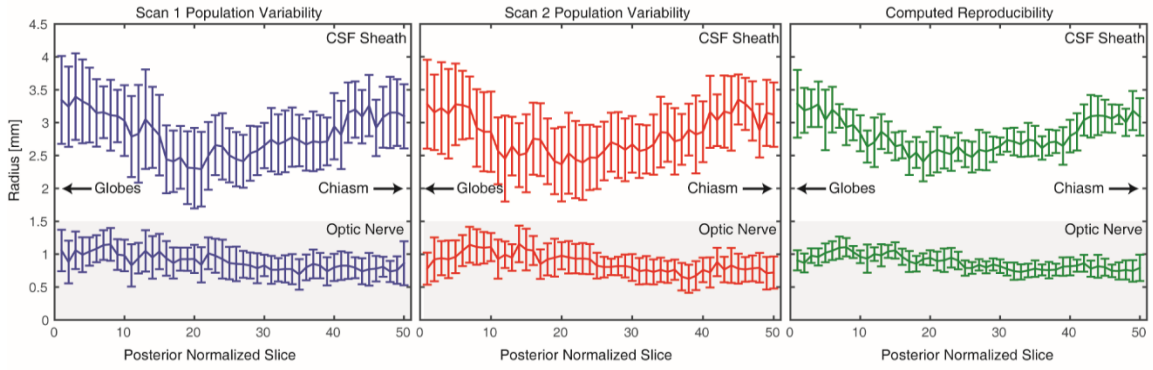

Figure IV.2. Comparison of population variability for scan 1 (blue) and scan 2 (red) as well as the computed reproducibility as the standard deviation of the difference of each scan-rescan measurement divided by $\sqrt{2}$. The computed reproducibility error bars are shown on the overall population mean distribution for comparison.

protocol [86]. Iterative conjugate gradient descent is performed on each slice which contains ON labels from the multi-atlas protocol. Each slice's optimal parameters are then used in the random forest regression to predict the true underlying radii of the ON and CSF sheath. The results are analyzed along the length of the ON. To make this comparison we interpolate every set of ON measurements to be the same number of samples as the longest one in the data set. The nature of the ONs allows for them to be present in a different number of slices from volume to volume. Interpolation more closely aligns corresponding parts of the ON across subjects. A three-element moving window median filter is also applied within each nerve across slices to reduce noise in the measurements.

3. Results

3.1. Short-Term Reproducibility

The radius of the ON (lower line) and CSF sheath (upper line) can be seen in Figure IV.2 for 8 subjects in scan 1 (blue) and 8 subjects in scan 2 (red). Two scans, from two separate subjects, were segmentation failures and are excluded from this analysis. The error bars are standard deviation and illustrate the population variability. The lower line is the radius of the ON along the length of the nerve and the upper line is the radius of the CSF sheath along the nerve. Note the labels indicating which direction is proximal to the globes and optic chiasm. The computed reproducibility (green) shows the standard deviation of the difference of each scan-rescan measurement divided by $\sqrt{2}$. This factor is divided out to account for the summation of two random variables. These error bars are plotted on the overall mean distribution for comparison. We here note that the computed reproducibility is less than the population variability and the variability along the length of the nerve. This data supports that this tool is useful in detecting local population differences.

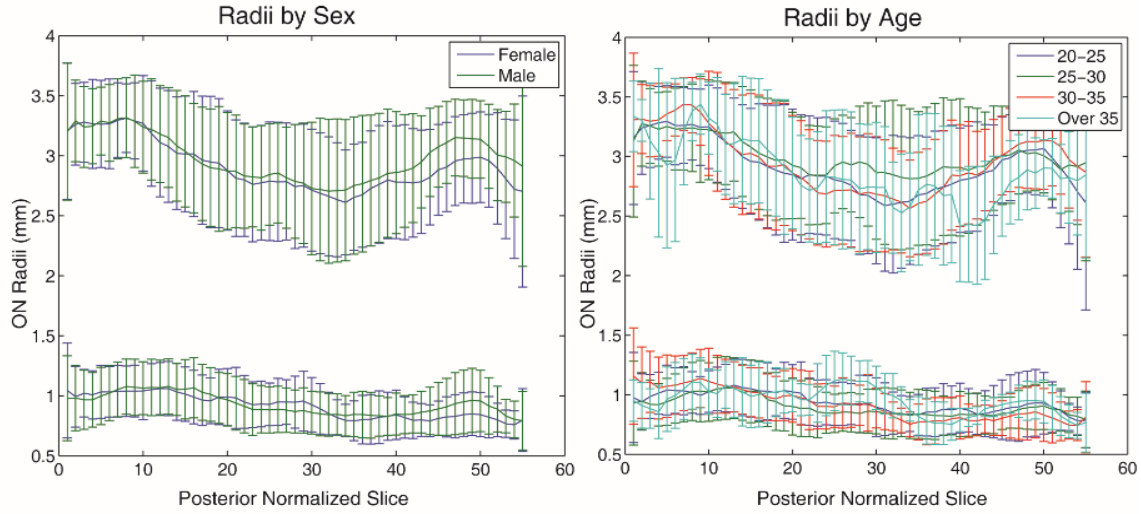

Figure IV.3. ON radius with error bars as the standard deviation as a function of normalized slice posterior to the globe illustrating the similarity of distributions regardless of age and sex among the 45 healthy controls.

3.2. Demographic Analysis

3.2.1. Normative Distribution Evaluation

Using this framework we examined the normative distribution of controls as a function of normalized length posterior to the globe. Variations in the distribution based on age and sex information were investigated and found to be nonexistent. Figure IV.3 shows the similarity of the distributions across both age and sex. This suggests that although the ON varies widely among healthy controls the variation is not dependent upon age or sex of the subject.

3.2.2. Patient Evaluation

We then compare the six selected patients to the normative distribution to see if irregularities became apparent. We would expect patients to fall outside of the normal distribution and it can be seen in Figure IV.4 that most of them do. From Figure IV.4 patient 1's ON appears to be smaller than the normative distribution around the midsection of the ON. This would suggest that this nerve is atrophic while the sheath appears to be approximately of normal size. The star indicates that this slice is shown for comparison in Figure IV.5 against an age matched control in the first column. The comparison in Figure IV.5 matches what is observed in the measurements from Figure IV.4. The sheath appears to be of a

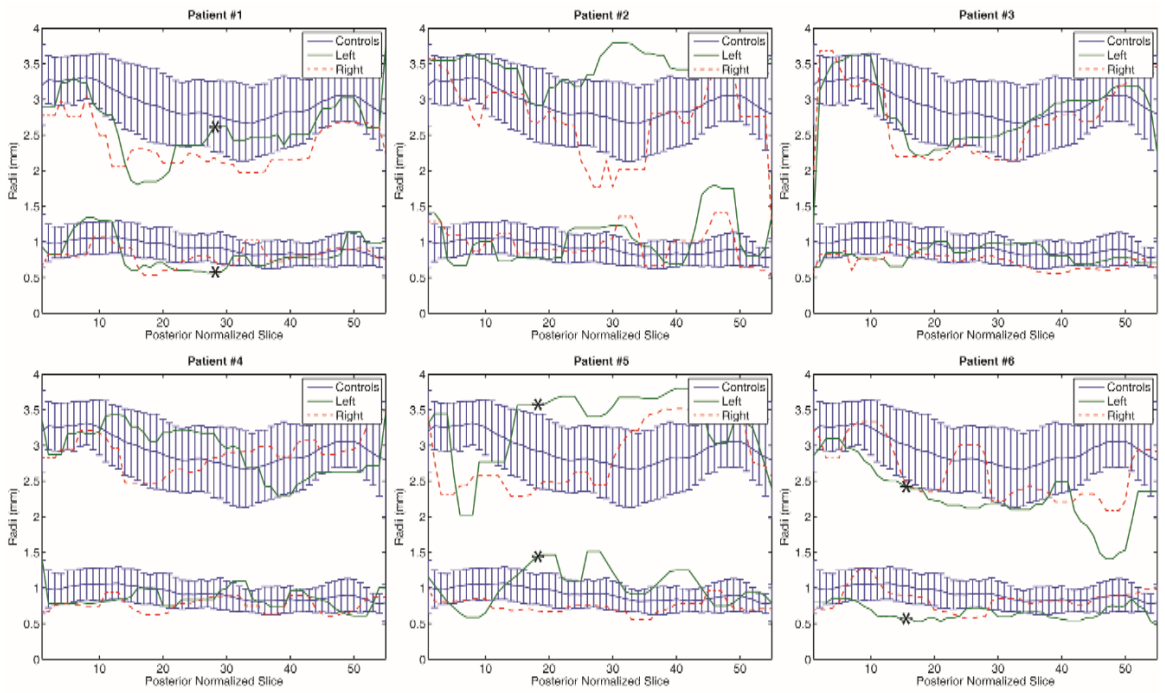

Figure IV.4. Measurements for the six selected patients as their left and right ONs compare to the normative distribution. Note the asterisks which mark the approximate locations of the visuals from Figure 4.

similar radius to the age matched control's sheath while the nerve appears slightly atrophic. Patient 2 appears slightly atrophic through the anterior part of the ON and we see inflammation in the posterior of the ON in both eyes. Patient 3 displays atrophy in both eyes in the anterior region. The right eye remains atrophic for the length of the ON while the left eye appears to approach the normative distribution. Patient 4 appears closest to the normative distribution although the right eye does appear to be slightly atrophic in some regions. Patient 5 shows atrophy in the right ON while the left ON appears highly inflamed. The stars again mark slices which can be seen in Figure IV.5 for comparison against an age matched control. In this comparison it is very clear the ON is much larger than that of the age matched control. Patient 6 appears atrophic in both eyes with the left being more severe. Once again Figure IV.5 shows a selected slice and it is clear that the ON is smaller in this patient when compared to the age matched control. These results show promise for this method as a possible tool to differentiate patient and control populations.

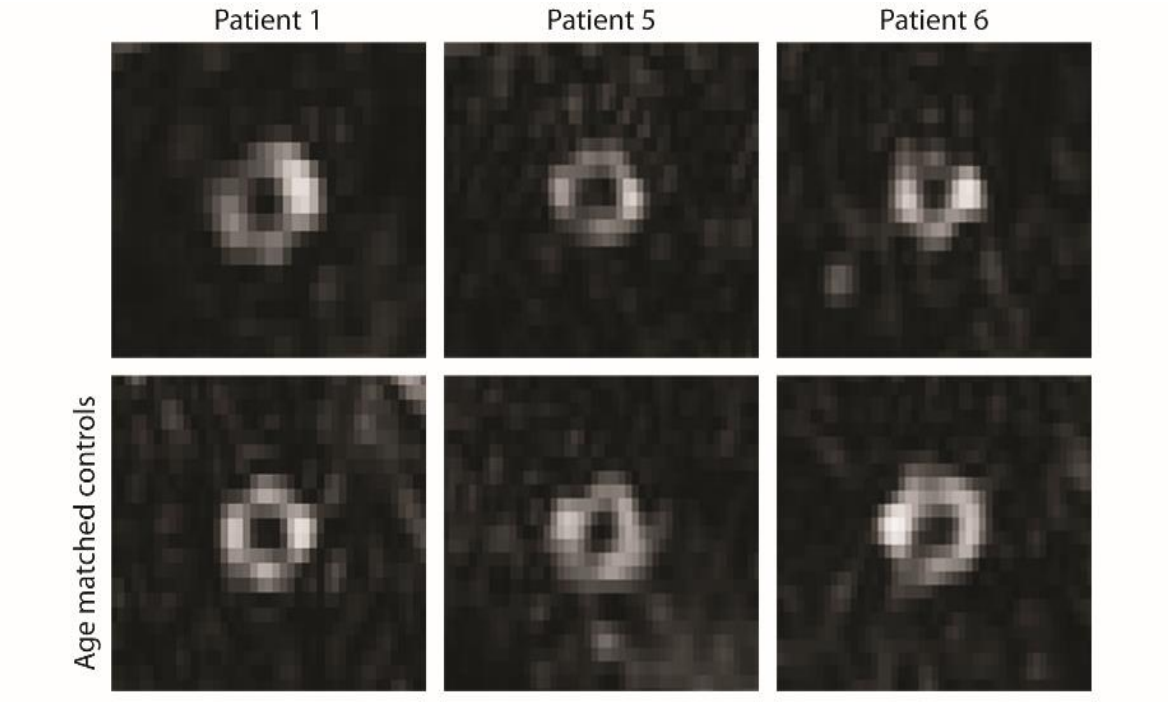

Figure IV.5. Selected comparisons of 3 patients and age matched healthy controls. Patients 1 and 6 are atrophic and patient 5 is hypertrophic.

4. Discussion

We have applied a fully automated pipeline to measure the radius of the ON and CSF sheath along the length of the nerve. We have demonstrated that this pipeline is sufficiently accurate to detect local population changes in both ON and CSF sheath size. The results are consistent with previous results that population variability should not vary across individuals based on age or sex [88]. Previously ON biomarkers have been investigated using manual or semi-automated methods which measured the ON at arbitrary points along the ON [61, 146, 147]. This proposed pipeline could be applied to disease populations to identify relevant disease biomarkers for disease onset. By measuring along the entire length of the nerve, we can identify meaningful areas of local changes which can lead to a more informed characterization of the ON by the clinical community.

We have presented a method for quantitatively measuring the ON and the CSF sheath and have demonstrated its feasibility as a possible tool for differentiating patients with ON atrophy or hypertrophy

from healthy subjects. Although this population of healthy control subjects contains a large amount of inter-subject variation the small comparison of patients suggests that there may be information which differs within patients from the normative distribution. This differentiation requires further investigation with a larger patient population to fully understand how patients with varying conditions compare across the length of the ON.

Chapter V. Improved Automatic Optic Nerve Radius Estimation from High Resolution MRI

1. Introduction

The human optic nerve (ON) is integral to visual performance as it carries all visual information posterior from the retina to the cortex for visual processing and is thus compromised in a number of diseases, most notably, multiple sclerosis (MS) [1], as well as several forms of optic neuropathy [1, 54]. Optic neuritis is known to be closely linked with MS as 25% of optic neuritis events eventually develop into MS [53]. However, despite this known association there are no current radiological biomarkers which can predict the eventual development of MS or the degree of visual recovery following an optic neuritis event. Therefore, while the ON is essential to visual function, it is challenging to image and quantify due to the fact that it is a small structure which is constantly in motion. The ON is surrounded by a sheath of cerebrospinal fluid (CSF). The size of this CSF sheath has been shown to correlate with intracranial pressure which may be associated with increased mortality and less favorable neurological outcomes [147]. Qualitatively, tools have been developed to visualize ON degradation utilizing high-resolution MRI but automatic quantitative methods are lacking.

Manual or computer-assisted measurements are still the tiresome standard for quantification of the ON. Hickman et al. used manual contouring to measure ON cross-sections in a longitudinal analysis

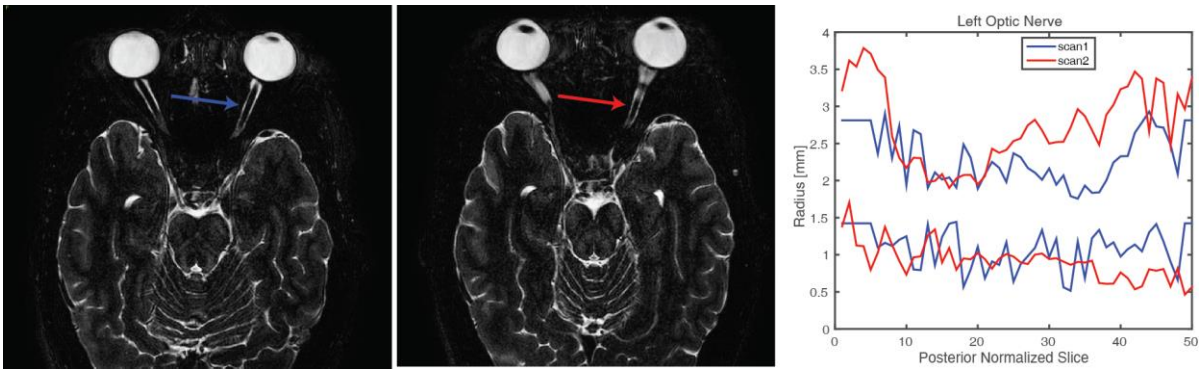

Figure V-1. An example subject's short term scan-rescan imaging showing scan 1 (left), scan 2 (middle) 19 days apart shown in radiological standard orientation. The right plot shows the measurement of the left optic nerve for scan 1(blue) and scan 2(red) illustrating the noise in the slice-wise measurements which warrant three-dimensional constraint.

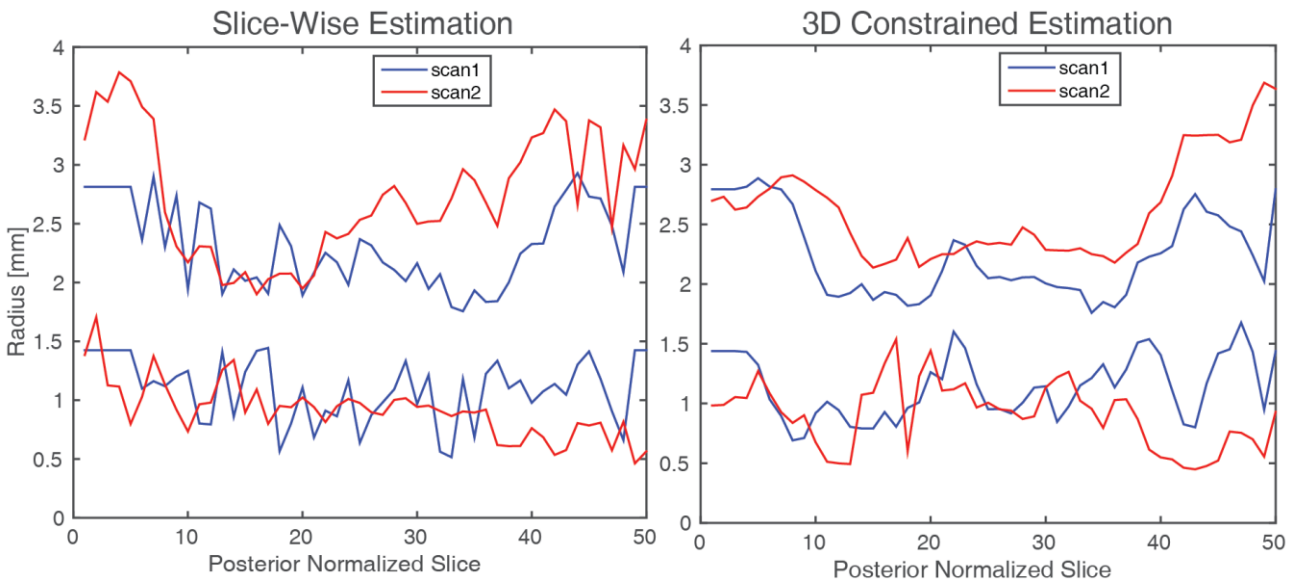

Figure V-2. Example radius estimation from slice-wise estimation (left) and constrained estimation (right) on the same ON from Figure V-1 showing the smoothness of the constrained estimation method

and found patterns consistent with acute inflammation followed by long-term atrophy [51, 52]. These measurements of optic nerve size are often taken at arbitrary points along the length of the ON and thus suffer because they would require significantly more time manually labeling cross sections to investigate local changes along the length of the nerve due to a lack of automated analysis techniques. A more detailed analysis of the ON may reveal anatomical patterns as well as other temporal patterns in disease state evolution. Automated segmentation methods have largely focused on segmenting the ON and CSF as a single structure, deeming it too challenging to measure the two independently [135, 137]. However, a previously presented slice-wise method addressed some of these concerns but yielded results which were useful in aggregate but could be difficult for interpretation on the single subject-level [87, 88]. Therefore, we propose a fully automated, three-dimensionally consistent technique, building upon the previous independent slice-wise technique, to estimate the radius of the ON and surrounding CSF on high-resolution heavily T2-weighted isotropic MRI.

2. Methodology

2.1. Proposed Method

Radius estimation begins with a previously described multi-atlas segmentation method [86], which automatically segments the orbits, optic chiasm and ON including the surrounding CSF for initialization purposes. This method uses 35 manually labeled atlas images, which include both healthy controls as well as ON head drusen, optic neuritis and MS patients. The target image to be segmented is registered to each of the 35 atlas images using an affine registration [107] to achieve a coarse alignment of the eye globes. The globe labels are summed for all 35 atlases to achieve a pseudo-probability map which is thresholded at 0.5 (or 18 atlas images indicating globe for a particular voxel). The centroids of each eye globe are extracted from this coarse hard segmentation and extended 30mm left, right and anteriorly, 40mm superiorly and inferiorly and 60mm posteriorly to define the cropping region. An affine and non-rigid registration of the cropped region to the cropped atlas images results in a more accurate transformation of the atlases to target space [143]. The manual labels of the atlas images are then transformed to the target space using these registrations and are fused using joint label fusion [148]. The segmentation of the ON includes both the ON and surrounding CSF so we must refine our segmentation to separate the two structures and measure them independently. The centroids of the ON label in the coronal plane are used as an initial estimate of the centerline of the ON. A cubic regression is performed to smooth the centerline and fill in any missing slices [62]. Patches are then extracted along this centerline for fitting to the following intensity model.

$$\hat{I}(x,y) = I_0\left[N\left(\vec{\mu},\Sigma_{xy}\right) - e^{\beta}\, N\left(\vec{\mu},\sigma_2\Sigma_{xy}\right)\right] \tag{V.1}$$

$$N\left(\vec{\mu},\Sigma_{xy}\right) = \frac{1}{2\pi\left|\Sigma_{xy}\right|}\exp\left[-\frac{1}{2}(X-\mu)^T\Sigma_{xy}^{-1}(X-\mu)\right] \tag{V.2}$$

$$\Sigma_{xy} = \begin{bmatrix} \sigma_x & \sigma_x\sigma_y\left(\frac{2}{1+e^{-\rho}}-1\right) \\ \sigma_x\sigma_y\left(\frac{2}{1+e^{-\rho}}-1\right) & \sigma_y \end{bmatrix} \tag{V.3}$$

We begin with a previously described model [145] which can be seen in Equation V.1 to fit the ON and CSF sheath in the coronal plane and extract the radii of both. Briefly, the model is a difference of two Gaussian distributions, as defined in Equation V.3, which closely resembles the intensity profile of the ON in the coronal plane in our heavily T2-weighted imaging. The covariance matrix in Equation V.3 allows for the model to become elliptical to account for off-axis imaging of the ON. The model is fit to the ON in the coronal plane using an iterative conjugate gradient descent optimization method [81].

In the novel variant of the method proposed herein, three-dimensional consistency is enforced through an iterative fitting procedure of this model. The length of the ON is initially fit with the model and each of the eight parameters are smoothed using a 5-element moving window average. Any points falling outside of a threshold n standard deviations away from the regression, $n\sigma_\theta$, are considered outliers and those slices are reinitialized with the regression value as their initial parameter values. The error term for the gradient descent is also winsorized at a value of ζ. The tolerance for n and ζ are simultaneously decreased with each iteration until a smooth set of parameters is converged upon.

The model parameters are correlated with the radii of the ON and CSF sheath through a random forest regression[85] using 1 million synthetic training images. Six of the eight model parameters are used for the regression, the centroids are omitted as they are dependent solely on field of view. The standard deviation parameters, $[\sigma_x, \sigma_y]$, are transformed to be a minimum and maximum term. It was experimentally observed that these terms can interchange for a single radius given the complementary angles of a nerve relative to the imaging plane. By characterizing the terms as a minimum and maximum, we force the radius transformation to be rotationally invariant to the fitting process and improves smoothness of the transformation. The 1 million training images were generated by simulating partial volume effects of imaging two concentric tubular structures with 0.6 mm isotropic voxels using a Monte Carlo simulation. This model is then tilted at randomly selected varying angles relative to the imaging plane and the size of each of the concentric tubes is varied randomly to generate the training set. The regression is validated using tenfold cross validation which shows the predicted radii to correlate with the true underlying simulated radii with an explanatory R-squared greater than 0.95 for both ON and CSF

radii.

2.2. Data Acquisition

Ten healthy subjects age 24 to 36 years (average: 28.25, median: 27 years, 6 male/4 female) were enrolled in the imaging study, after obtaining consent from the local institutional review board. Imaging was acquired on a 3T Philips Achieva (Philips Medical Systems, Best, The Netherlands) with a 2-channel multi-transmit body coil for transmission and an 8 channel head coil for reception. After tri-planar localization, we acquired all volumes in the axial plane. These images were collected with a Volume Isotropic Turbo spin echo Acquisition (VISTA) imaging sequence with the following parameters: 3D TSE TR = 4000ms, TE = 455ms, $\alpha = 90°$, FOV= 180 x 180 x 20mm^3, acquired resolution = 0.55 x 0.55 x 0.55mm^3, reconstructed resolution = 0.35 x 0.35 x 0.35mm^3, SENSE factor = 2, fat saturation = SPIR, NSA=2 and total scan time = 7:48. Subjects were scanned with a baseline scan and again within 30 days

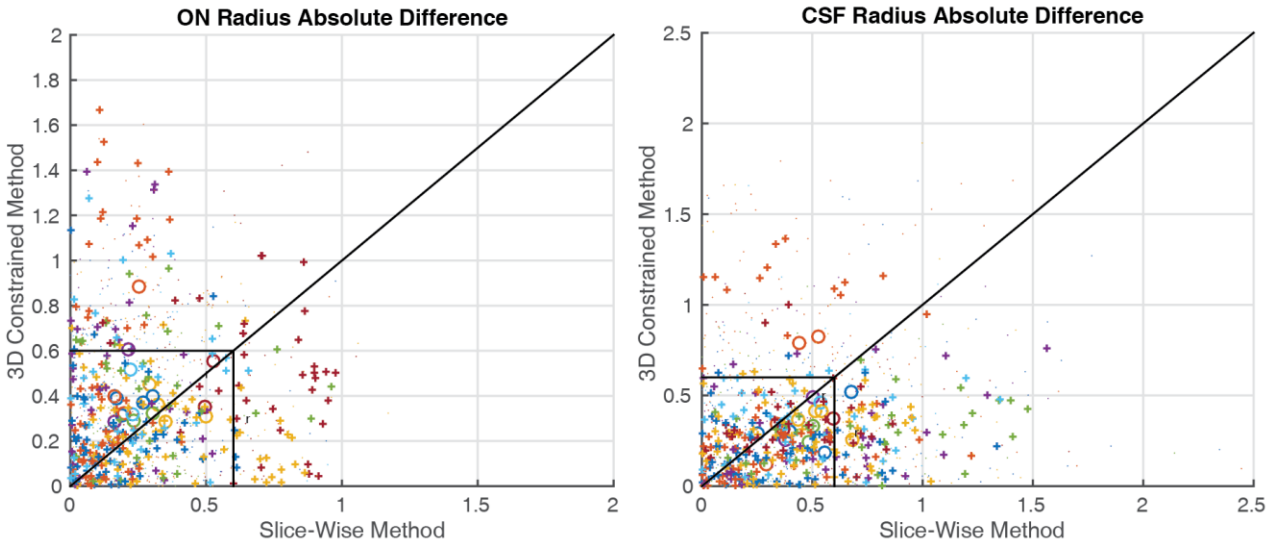

Figure V-3. Comparison of scan-rescan absolute error for the ON (left) and CSF (right). Large circles indicate the mean absolute error for a given nerve. Dots indicate individual points between nerves with the color corresponding to each subject. Pluses are individual points between nerves within the central third of the length of the nerve, the area which is most accurately imaged. The lines are drawn along unity and at resolution (0.6mm). Note that pluses tend to be localized within the box indicating reproducibility within a voxel for the central third of the nerve as well pluses being localized below the line of unity indicating the proposed method has lower absolute error between scans.

of the original scan for short-term reproducibility. Inter-scan time was from 4 to 29 days (average: 19.4 days, median: 23 days). Figure V-1 shows an example short term scan-rescan image pair. Five of the 10 subjects were also imaged 11 months later for a long-term follow-up scan with the same acquisition scheme.

2.3. Analysis: Short- and Long-Term Reproducibility

The original slice-wise analysis method [87] and the proposed method are performed on the above data for comparison. The shape of the ON often results in a variable number of coronal slices between individuals and within individuals across different scans. For comparison each ON was interpolated to be the same length as the longest ON in the population, we refer to this as posterior normalized slice. Scan-rescan error is quantified as the absolute difference for each point along the ON. Scale-invariant smoothness (Equation V.5) for each method is computed as the standard deviation of the difference between neighboring points scaled by the absolute mean difference of all neighboring points within the nerve. All tests for significance are performed using Wilcoxon sign-rank ($p<0.05$).

$$\mu_d = \frac{1}{n-1}\sum_{i=2}^{n} x_i - x_{i-1} \tag{V.4}$$

$$s = \frac{\sqrt{\frac{1}{n-1}\sum_{i=2}^{n}(x_i - x_{i-1} - \mu_d)}}{|\mu_d|} \tag{V.5}$$

3. Results

3.1. Short-Term Reproducibility

The 3D constrained results are smoother along the length of the ON, as computed by scale-invariant smoothness ($p=0.0025$), providing more anatomically plausible results since the ON does not change size rapidly. Figure V-2 shows a qualitative comparison of the slice-wise results and the 3D

constrained results. The 3D constrained results are much smoother along the length of the ON providing more anatomically plausible results since the ON does not change size rapidly. Figure V-3 shows the absolute error between the baseline and short term follow-up scans for the aligned ON points. The circles are mean absolute error for a single nerve, with colors representing each subject. The individual points which are dots are the absolute difference between two measurements outside the middle third of the ON, the points which are pluses are the absolute difference between two points within the middle third of the ON again with color corresponding to subjects. The black box indicates error of one voxel and the line of unity separates points with lower slice-wise error (above) and lower 3D constrained error (below). We can see that the majority of the circles and pluses are grouped within the box indicating absolute difference of less than one voxel for the entirety of the nerve and the points within the central third of the ON respectively. There are a large number of CSF sheath measurements (13%) within the central third of the ON which were previously larger than one voxel reproducibility which are now less than one voxel, of the CSF measurements previously outside one voxel nearly all (89%) are now within one voxel.

3.2. Long-Term Reproducibility

Figure V-4 shows a comparison of the short- and long-term reproducibility using the proposed method for the five subjects with long-term follow-up data. The symbols are the same as Figure V-3 with circles representing a subject's ON, pluses indicating individual points within the central third of the ON and dots representing individual points outside the central third. The black box is drawn at resolution and we can see that the majority of points fall within one voxel difference. The subject-wise ON reproducibility, represented by circles, is largely centered along the line of unity indicating that the short- and long-term reproducibility of the ON measurements are similar. While the subject-wise CSF reproducibility trends above the line indicating larger differences between the baseline and long-term follow-up scans than between baseline and the short-term follow-up scans.

4. Discussion

We have demonstrated the superiority of our proposed three-dimensionally consistent ON radius estimation procedure as compared to the previous slice-wise radius estimation procedure in generating anatomically viable results which are reproducible with error of less than the voxel resolution. Future work should address challenges faced in accurately characterizing the anterior ON in the presence of retrobulbar motion and the posterior ON in the presence of frontal lobe CSF to improve characterization along the entire length of the ON. A larger cohort of subjects with long-term follow-ups will be necessary to evaluate the long-term changes in ON morphology with more certainty.

Long-term reproducibility has been shown to be similar to short-term reproducibility indicating that the ON and surrounding CSF do not change substantially within a one year period. Histological studies have shown that there is a slow loss of axons in the optic nerve with normal aging [149-151], but the morphological differences in a 1 year period are expected to be very small based on minimal (if any) change in the optic disk [140, 152-155]. To date, the authors are not aware of studies that have longitudinally followed human optic nerve morphometry *in vivo*.

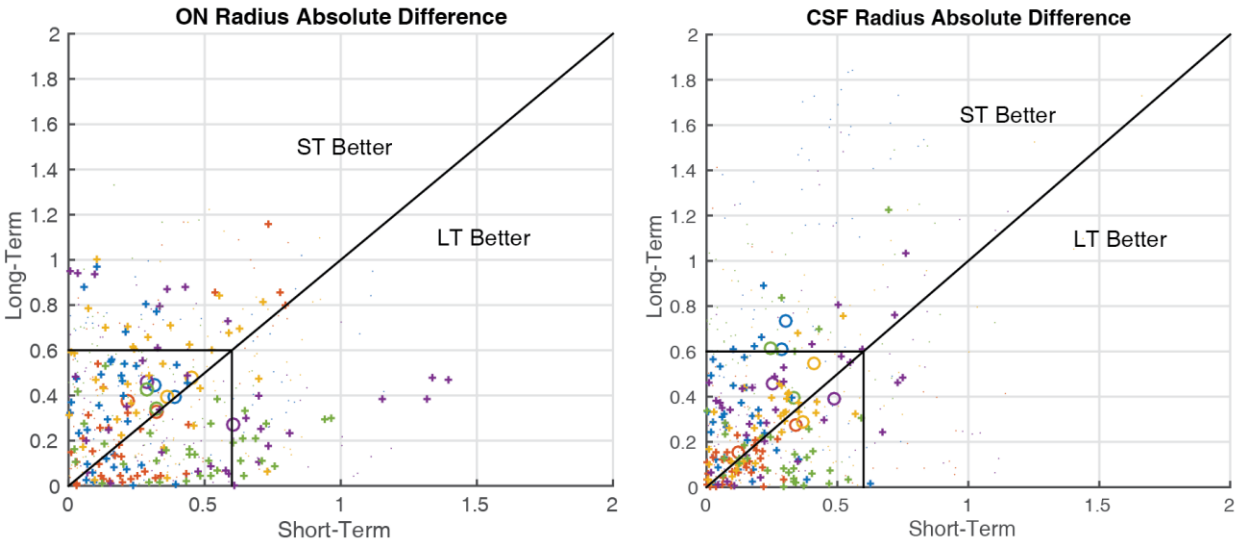

Figure V-4. Comparison of short- and long-term scan-rescan absolute error for the ON (left) and CSF (right). Large circles indicate the mean absolute error for a given nerve. Dots indicate individual points between nerves with the color corresponding to each subject. Pluses are individual points between nerves within the central third of the length of the nerve, the area which is most accurately imaged. The lines are drawn along unity and at resolution (0.6mm). Note that pluses tend to be localized within the box indicating reproducibility within a voxel for the central third of the nerve.

The large variability in ON size suggests that a much larger number of subjects will be required to characterize normal ON variability [140]. With a larger set of controls [88] evaluated with this method they could be compared against disease populations, such as acute optic neuritis or MS to investigate possible imaging biomarkers for disease severity or prognosis. Automatically characterizing the entire ON from globe to chiasm will allow for more meaningful searches for imaging biomarkers by the clinical community possibly revealing latent local changes in the ON which offer prognostic value.

All tools used and developed in this work are available in open source from their respective authors. The ON-CSF measurement code is primarily written in MATLAB (The MathWorks, Inc., Natick, Massachusetts, United States) and bundled into an automated program (i.e., "spider"[156]) that combines these tools using PyXNAT[157] and DAX[158] for XNAT [159] and is available through the NITRC project MASIMATLAB (http://www.nitrc.org/projects/masimatlab).

Chapter VI. Quantitative Characterization of Optic Nerve Atrophy in Patients with Multiple Sclerosis

1. Introduction

The human optic nerve is a small (< 3mm in diameter) white matter fiber bundle that exits the globe and courses posteriorly to the optic chiasm, and is responsible for communicating all visual stimuli to the optic tracts. It is immediately surrounded by cerebrospinal fluid (CSF) and sits inside the fatty tissue of the orbit superior to the maxillary sinuses. In patients with multiple sclerosis MS), the optic nerve is one of the most common sites of injury. Approximately 25% of MS patients have retro-bulbar optic neuritis as the first symptom and nearly two-thirds of MS patients experience at least one optic neuritis event in their lifetime. Optic neuritis is transient and may self-resolve in some cases or leave permanent damage in some others, though intervention with steroids has been shown to reduce the duration of symptoms[160]. Upon the acute phase resolution, optic neuritis leads to visual deficits in about 40-60% of MS patients. The biological substrate of these visual defects is unknown but axonal loss likely plays a major role[161]. This axonal loss is often investigated through optical coherence tomography using the surrogate of retinal nerve fiber layer thickness, which has been shown to correlate with disease severity because the loss of retinal axons is believed to be related to brain damage and atrophy[162]. However, this relationship is not well understood and only offers a surrogate for optic nerve axonal loss.

MRI of the orbits represents a viable diagnostic tool for optic neuritis. In the acute phase, may present as an active lesion of the optic nerve on T1-weighted post-contrast sequences. This may leave a hyperintense lesion on T2-weighted MRI upon the resolution of the inflammatory event. Signal changes may be either focal or diffuse. Despite its clinical application, MRI of the orbits often in times turns to be of little utility since signal alterations may not be visible even in the presence of a clear acute clinical event or chronic symptoms sequela of tissue injury. Capturing axonal loss which ultimately results into optic nerve atrophy is virtually not possible. Measuring volume of the optic nerve is challenged by lack of

contrast within the optic nerve, resolution sufficiently high to discriminate between the optic nerve and surrounding CSF.

Aside from MRI pulse sequences, a lack of robust analysis tools to characterize optic nerve atrophy cross-sectionally and over time. Analyses typically proceeded by taking a single measurement of optic nerve size at a specified location along the nerve [61, 163-165]. In this type of analysis, a single measurement is approximated as a surrogate for the health of the entire optic nerve and does not account for focal changes that may occur throughout the optic nerve length.

Recent advancements in MRI pulse sequences offered improved contrast between the optic nerve and surrounding CSF while maintaining a relative insensitivity to motion (Figure VI-1). Our group has characterized these improvements in optic nerve MRI in healthy controls[88]. Additionally, we have recently developed an analysis pipeline for optic nerve MRI that affords an opportunity to evaluate the morphology of the optic nerve in vivo along its entire length[87, 90], thereby allowing measurements of both global and focal atrophy.

To date, there has not been a systemic study of optic nerve morphological changes in patients

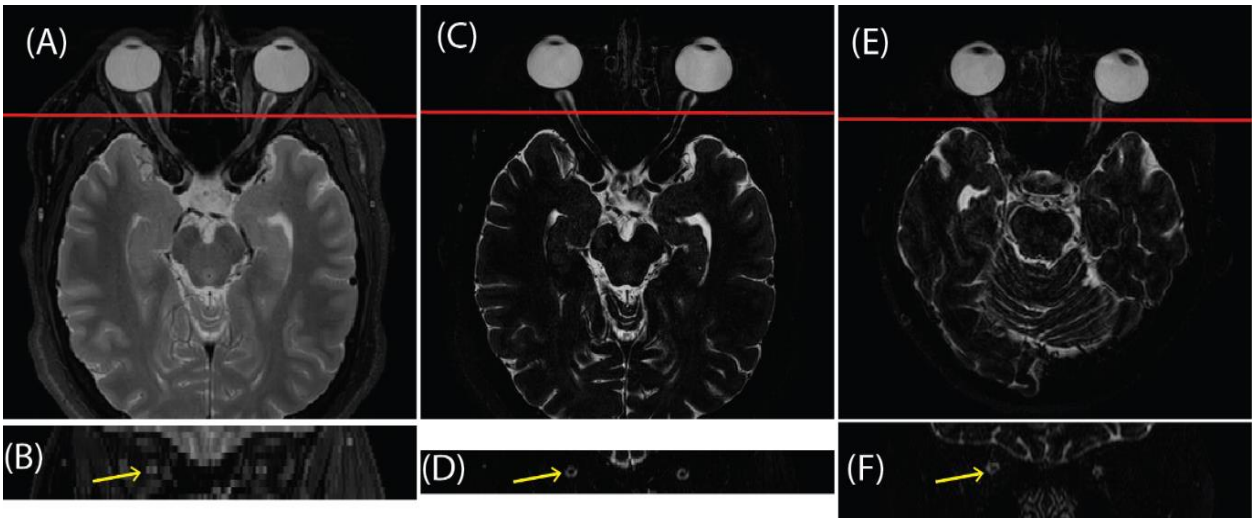

Figure VI-1. Healthy control scanned with: current clinical standard of care T2w MRI axial view (A) and coronal view approximately 10mm posterior to the globe (B), as well as high-resolution isotropic T2w research imaging axial view (C) and coronal view approximately 10mm posterior to the globe (D). One can appreciate the superior optic nerve:CSF contrast and benefits of isotropic resolution in visualizing optic nerve morphology in 3-dimensions. (E) and (F) show axial and coronal views of a 40-yo RRMS patient with bilateral history of optic neuritis one year post-diagnosis.

with MS, to ascertain the amount of atrophy the optic nerve undergoes along its length after optic neuritis. As atrophy is directly tied to axonal loss, there is a need to understand optic nerve damage in MS accounting for local changes along the length of the optic nerve. Motivated by this notion, we propose our study. We hypothesize that optic nerve volume loss can be detected and quantified in MS patients. Here, we report on the first automatic evaluation of optic nerve atrophy using advanced MRI in relapsing-remitting MS patients.

2. Materials and Methods

2.1. Study Design

This study is a collaborative project between the neuro-immunology division in the Neurology Department and the Institute of Imaging Science in the radiology Department at Vanderbilt University Medical Center. The study was performed with approval of the Vanderbilt Institutional Review Board and signed informed consent was obtained prior to data acquisition from each subject. Twenty-nine MS (median age: 33; age range: 18-53; 69% female; 28 relapsing remitting MS and 1 clinically isolated syndrome) and 42 healthy volunteers (median age: 28, age range: 20-38; 52% female) were enrolled in the study. Fourteen (48%) patients had no history of optic neuritis (namely ON-, hereafter). The remaining 15 patients had a history of either bilateral (7 patients) or unilateral (8 patients) optic neuritis (namely ON+, hereafter).

2.2. MRI Protocol

Anatomical T2-weighted (T2w) VISTA (SPACE on Siemens, CUBE on GE) scans were obtained on a 3 Tesla (3T) Philips Achieva (Philips Medical Systems, Best, The Netherlands) using a two-channel body coil for transmission and an eight-channel head coil for reception. Images were acquired on the axial plane aligned with the optic nerve. Sequence parameters were: 3-Dimensional (3D) fast spin echo

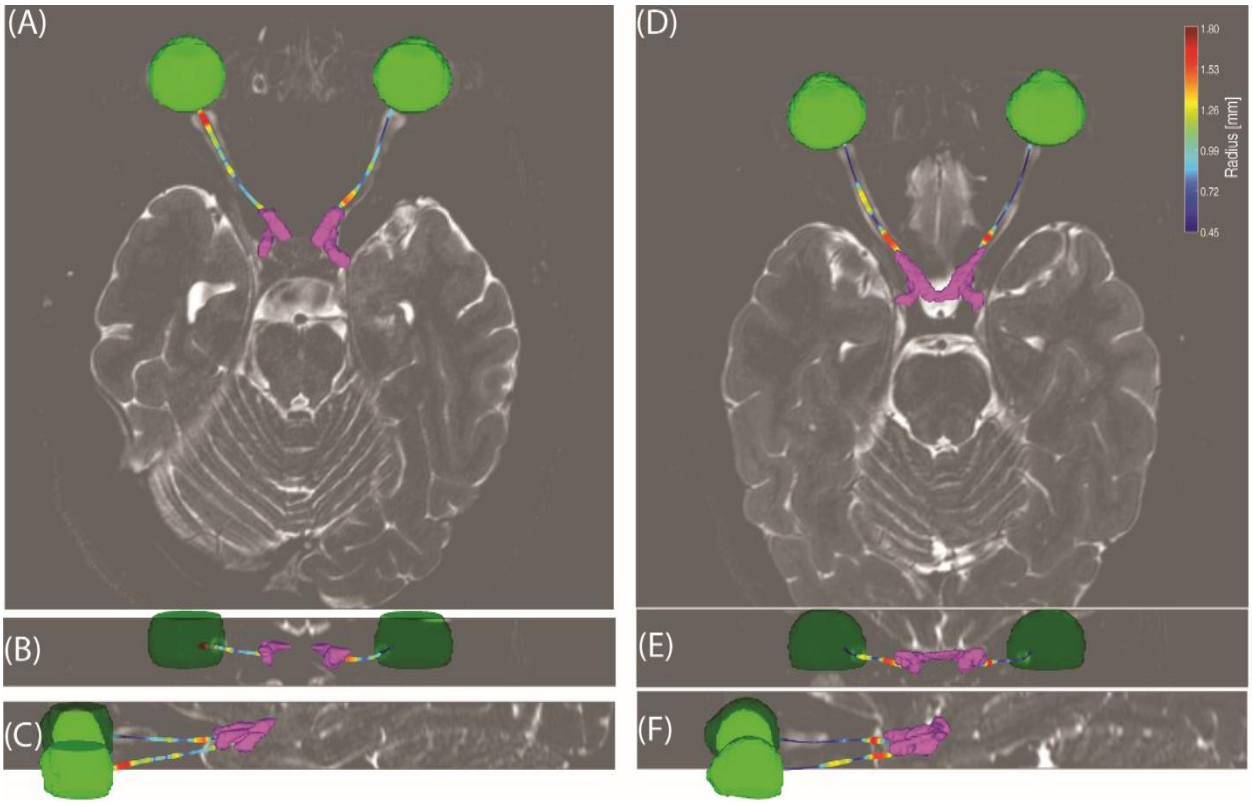

Figure VI-2. Renderings of the segmented eye globes (green) and optic chiasm (purple) along with the measured optic nerves for a healthy control (A-C) and a 47-yo RRMS patient 15.5 years post diagnosis with a history of optic neuritis in the left eye (D-F). Color of the optic nerve corresponds to estimated optic nerve radius in all panels according to the colorbar in (D). Optic nerve atrophy can be clearly seen in (D-F) as compared to (A-C).

(repetition time/echo time/flip angle [TR/TE/α= 4000ms/404ms/90°), field of view= 180 x 180 x 42mm3, nominal resolution = 0.6 x 0.6 x 0.6mm3, SENSE factor = 2, fat saturation = SPIR, and total scan time = 5:20.

2.3. Volumetric Measurements

We utilize a previously published, open source tool with minor modifications to automatically measure the radius of the optic nerve and surrounding cerebrospinal fluid[87]. Briefly, this model fits an intensity profile to the optic nerve and cerebrospinal fluid in the coronal plane and transforms the parameters from that fit into physical radius measurements. The model is applied to each coronal slice of the image containing the optic nerve and can therefore result in inconsistent measurements along the

length of the optic nerve. To address this shortcoming we have modified this model by applying it in an iterative manner while decreasing the tolerance from adjacent slices[90]. This technique allows the model to ignore slices which are less than optimal and results in anatomically viable, three-dimensionally consistent measurements along the entire length of the optic nerve. This model is then applied to all of the patients and healthy volunteers, generating two sets of measurements for each individual.

2.4. Statistical Analysis

Volumetric data from the 42 pairs of nerves of the healthy control group were used to generate a normative distribution for detecting differences in patient sub-populations [88]. Group (patents vs healthy volunteers) differences in the optic nerve radius estimates were compared using a Wilcoxon rank-sum test. We use a previously published technique for comparing optic nerves across subjects to overcome the differing number of measurements for each subject [88]. Measurements are interpolated to be the same length as the longest nerve amongst the population.

3. Results

3.1. Qualitative Results

Figure VI-2 shows qualitative results for a healthy control (A-C) and a 47-yo relapsing remitting MS patient (D-F). The automatically segmented eye globes and optic chiasm are rendered in green and purple respectively. The measurements for the optic nerve are rendered with color representing the nerve radius according to the color bar in (D).

3.2. Quantitative Analysis

Volumetrics of optic nerves which have never been affected by a clinical episode of ON (n=28) were not significantly different from those derived from healthy controls (Figure VI-3 left). Involved nerves showed significantly reduced radius from healthy controls at 33% (16/48) of measurements localized in the central portion of the nerve and surviving Bonferroni correction (Wilcoxon rank-sum; $p<0.05$ Figure VI-3 right). Of these differences, 15 were continuous points in the central portion of the nerve (Figure VI-3 right: shaded area), the last point which is significantly different from the healthy controls is posterior to the shaded region, separated by a single non-significant point.

4. Discussion

We present the first analysis of optic nerve radius using advanced MRI along the entire length of the nerve as it applies to patients with MS and optic neuritis. In the present work, we used a T2W TSE sequence with extended echo train. The advantage of this sequence over currently available ones is the superior resolution and nerve/CSF contrast. It also shows a clinically affordable acquisition time[89]

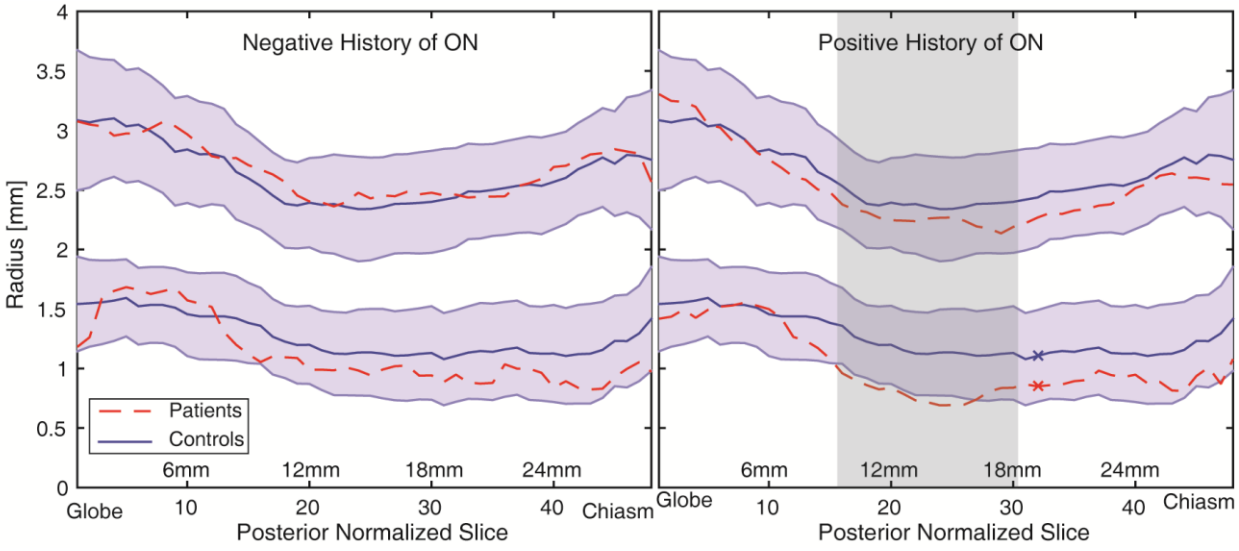

Figure VI-3. Comparison of volumes of optic nerves never affected by optic neuritis (left) and optic nerves with a previous history of optic neuritis (right) to healthy controls. The shaded blue region indicates one standard deviation of the healthy control population. The shaded region (right) illustrates the region of 15 consecutive measurements (9mm) where the patients' nerves are significantly smaller than healthy nerves (Wilcoxon rank-sum; p<0.05 Bonferroni corrected). The nerves from patients with a negative history of optic neuritis were not significantly different from healthy controls.

(Figure VI-1 A-D). The isotropic resolution allows for accurate 3D characterization of the optic nerve from globe to chiasm.

Our data detected for the first time a group-level atrophy effect on nerves affected by optic neuritis as compared to optic nerves which have never been affected by disease. This analysis is superior to traditional single-point metrics which have been traditionally used to characterize optic nerve atrophy as this technique can provide more insight into focal optic nerve changes. As such this technique has the potential to provide a greater understanding of the degree and location of axonal loss which is known to be associated with optic neuritis.

The single non-significant measurement point between the large collection of significantly different points is likely due to the reduction of estimation accuracy at the most posterior and inferior regions of the optic nerve. The anterior portion of the nerve is difficult to characterize accurately due to motion artifacts from saccadic eye movements. The posterior region of the nerve is difficult to characterize as the sub-arachnoid CSF thins as the nerve approaches the optic chiasm. This thinning of CSF reduces the contrast available for accurately measuring the nerve. We hypothesize that a more sensitive radius estimation technique would likely find global atrophy among even more measurements than that found in this study.

Although novel, our work is not exempt from limitations. In the future it could be improved upon by accounting for the curvature of the optic nerve in the interpolation step. Interpolating nerves to be the same length results in a coarse alignment of nerves across the population but does not account for varying curvature across subjects. Investigation into the most appropriate alignment methods is still required.

Our method is also resolution dependent which limits the number of subjects which can be utilized in these studies since it cannot be applied to clinical standard of care imaging protocols. If the method were to be extended to work on multiple or lower resolutions while maintaining comparable accuracy study sizes could increase.

Notwithstanding the above limitations, we believe that our work represents a preliminary but solid demonstration of volumetric measurements of the optic nerve in its entire length. With future work

this methodology may translate into clinical application and can provide useful information on the disease stage and course in patients with history of optic neuritis, whose symptoms often in times do not find a biological surrogate.

All tools used and developed in this work are available in open source from their respective authors. The optic nerve/CSF estimation code is primarily written in MATLAB (The MathWorks, Inc., Natick, Massachusetts, United States) and bundled into an automated program (i.e., "spider"[156]) that combines these tools using PyXNAT[157] for XNAT[159] and is available in open source through the NITRC project MASIMATLAB (http://www.nitrc.org/projects/masimatlab).

Chapter VII. Characterization of Short- and Long-Term Stability of Non-Invasive Optic Nerve Imaging

1. Introduction

Magnetic resonance imaging (MRI) has been utilized for decades to investigate anatomical changes in the eye orbit [48, 166]. For example, in a clinical setting it is used to evaluate possible optic glioma [167]. However, more recently there has been an effort to utilize MRI quantitatively to attempt to uncover yet undiscovered biomarkers of eye orbit health. Historically, quantitative MRI measurements have been made manually which is time consuming and inaccurate [61, 163-165]. More recently, advancements in eye orbital MRI and image processing techniques have allowed for automated quantitative investigation of eye orbital structure [87, 92]. With these recent advancements comes the challenge of comparing and contrasting various algorithmic approaches to quantitative eye orbit MRI analysis. Results reported must always be taken in context with the type of data being analyzed. Optimization of non-clinically viable MRI techniques could lead to inflated algorithmic performance compared to those designed to work on clinical standard of care imaging. There are currently many open resources for multi-parametric whole brain MRI including the Alzheimer's disease neuroimaging initiative (ADNI) [168], open access series of imaging studies (OASIS) [169], the openFMRI project [170] and the PAIN repository [171]. However, none of these resources are targeted at orbital imaging and therefore present an accurate representation of the current clinical standard of care, and state-of-the-art, of orbital MRI. In this work, we address this challenge by acquiring a short- and long-term reproducibility dataset of young healthy controls acquired using current clinical standard of care as well as current state-of-the-art MRI techniques at 3T. The release of this resource provides the image processing community with a common dataset for fair comparison of both clinical standard of care and advanced MRI image processing techniques.

2. Methods

Twenty-four healthy volunteers with no history of ophthalmological or neurological conditions were enrolled in the study and informed consent was obtained. Five subjects never returned for any follow-up scans after baseline. Of the remaining nineteen subjects (7 Female; age at baseline mean: 27.1 years; median: 25 years; range 23-36 years) Ten were scanned a second time within one month of the initial scan (mean age: 27.6 years; 4 females; mean difference: 19.4 days; min: 4 days; max: 29 days) both with protocol 1 (Table VII-1). Seventeen subjects were scanned again approximately one year after baseline (mean difference: 353 days; min: 329 days; max: 395 days) with Protocol 2 (Table VII-1) to asses long-term stability. All data were acquired using a 3T Philips Achieva (Philips Healthcare, Best, The Netherlands) with body coil excitation and an 8-channel head coil for reception. These seventeen subjects also underwent bilateral retinal and optic nerve head OCT scanning on a Heidelberg Spectralis (Heidelberg Engineering, Heidelberg, Germany). The sequence selection (Table VII-1) is introduced in the following sections.

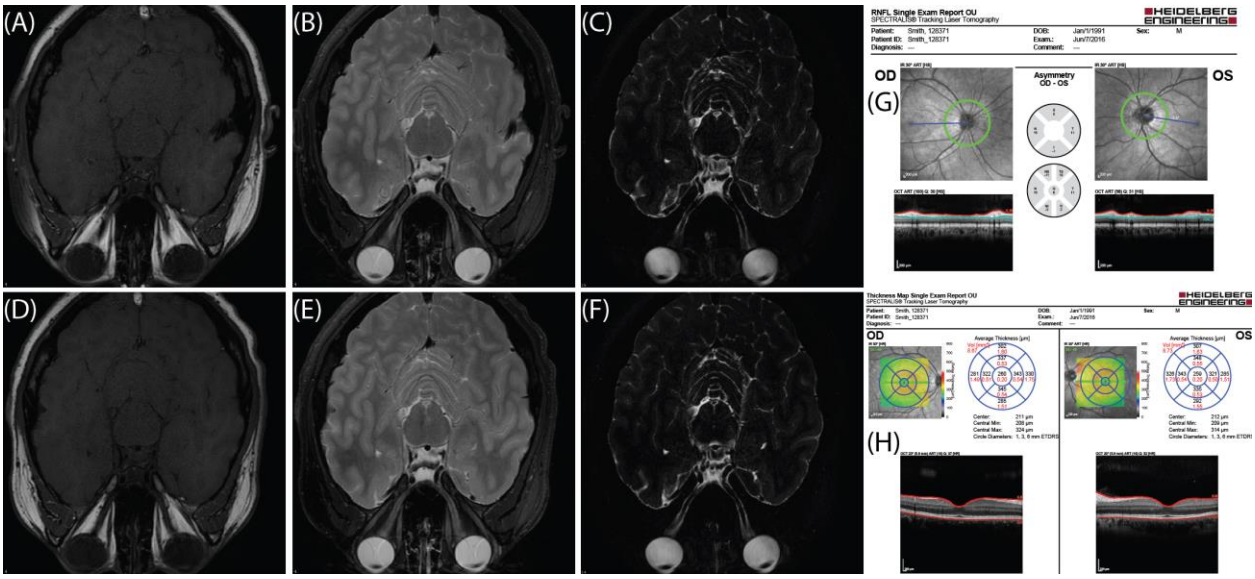

Figure VII-1. Example subject showing their baseline clinical standard of care T1w scan (A) T2w scan (B) and high resolution isotropic optic nerve optimized scan (C) as well as their long-term follow up T1w (D), T2w (E) and high resolution optic nerve (F). The associated OCT imaging acquired at long-term follow up for their optic nerve head scan (G) and macular (H).

2.1. Data

2.1.1. Structural Imaging

Structural MRI has been used to generate contrast between surrounding structures of interest, in this case the optic nerve and surrounding orbital tissues. Images representative of the current clinical standard of care were acquired for evaluation of application to clinical imaging. Clinically viable high resolution isotropic optic nerve imaging optimized for optic nerve:CSF contrast [89] is included for evaluation of algorithms which aim to differentiate optic nerve and surrounding CSF [87]. Finally, traditional whole-brain MPRAGE and FLAIR imaging were acquired for normalization of brain volume as well as evaluation of the controls' whole brains.

2.1.1.1 Current Clinical Standard of Care

Traditional MRI contrast mechanisms of transverse (T2) and longitudinal (T1) relaxation have been used clinically to look for qualitative abnormalities of orbital structures. We employ a recreation of the current clinical standard of care scans performed at Vanderbilt University Medical Center for orbital evaluation of patients. This protocol includes four scans for visualization of the eye orbit, coronal and axial T1W spin echo images and coronal and axial T2W turbo spin echo images. These images each have high in-plane resolution with thick (3mm) slices for visualizing orbital abnormalities. Inclusion of these protocols allows for evaluation of applicability of processing techniques to current clinical imaging databases.

2.1.1.2 High resolution isotropic optic nerve imaging

Recently 3-dimensional isotopic imaging sequences have been developed to illicit contrast between the optic nerve and surrounding cerebrospinal fluid for accurate characterization of optic nerve morphology [89]. This sequence employs a T2W turbo spin echo with optimized readout to achieve high-resolution isotropic contrast. This eliminates the need for coronal and axial acquisitions and therefore reduces scan time compared to current clinical standard of care. These data allow for evaluation of analysis techniques which aim to measure optic nerve morphology [90].

2.1.1.3 MPRAGE

Magnetization prepared rapid acquisition gradient echo (MPRAGE) [172] creates high-contrast T1W images by playing out an inversion pulse such that the magnetization of the gray matter is very near zero during the excitation pulse. This creates contrast between the gray- and white-matter allowing for qualitative assessments of neurological health. This sequence is included to ensure neurological normality of enrolled subjects and for any analysis techniques which may require whole-brain information.

2.1.1.4 FLAIR

Fluid attenuated inversion recovery (FLAIR) imaging uses an inversion pre-pulse which is timed such that the water signal is very near zero when excitation occurs. This occurs in combination with a long echo time produces heavy T2-weighting and is very useful in identifying lesions [173].

2.1.2. Magnetization Transfer Imaging

Magnetization transfer (MT) imaging has been shown to be sensitive to myelin content and may be useful in evaluating disease progression in demyelinating diseases [174]. We deploy a single-slice MT imaging protocol which uses a three-echo Dixon readout in combination with fixation to achieve MT quantification of the optic nerve[175].

2.1.2.1 B_0 Mapping

A map of the main magnetic field (B_0) is acquired to correct for any shift in the offset frequency prescribed when fitting a quantitative MT biophysical model. B_0 estimation is acquired from two gradient echo phase images with $\Delta TE=2.3ms$[176].

2.1.2.2 B_1^+ Mapping

Mapping of the RF transmit field is employed to correct for any shift in the actual transmitted RF power of the saturation flip angle for MT estimation. Mapping is achieved using the actual flip angle imaging method[177].

2.1.2.3 Multiple Flip Angle

Longitudinal relaxation (T_1) is estimated using a multiple flip angle (MFA) acquisition using six flip angles from 5° to 30° (TR/TE=20/4.6ms).

2.1.3. Diffusion Tensor Imaging

Diffusion tensor imaging (DTI) utilizes multiple diffusion weighted images (DWI) acquired with

different directions and diffusion times to estimate the diffusion of water within a single voxel. We acquire 32 gradient directions at b-value 1000 s/mm^2. Five minimally weighted reference images (b0's) were also acquired. Voxel resolution for the data is 2.5mm x 2.5mm x 2.5mm with a matrix of 96 x 96 and 50 slices. The scan parameters were: SENSE=2.2; TR=7800ms; TE=53 ms; partial Fourier=0.7. Fold over direction was A-P.

2.1.3.1 B_0 Mapping

As with MT imaging a map of the main magnetic field is acquired to accompany the DTI imaging to allow for correction of main magnetic field inhomogeneities.

2.1.4. Optical Coherence Tomography Imaging

Each subject has bilateral retinal and optic nerve head OCT imaging acquired for Protocol 2. OCT has been shown to be a useful surrogate for demyelination and progression of multiple sclerosis [25, 62] and it is important to understand the interactions of OCT and retinal health and how it relates to other orbital structures investigated through MRI.

2.2. Analysis

All imaging data were transferred in DICOM format to a PACS node and then to an XNAT instance where they were converted to Neuroimaging Informatics Technology Initiative (NifTI) format [158]. Data are identified by randomized scan session codes and all subsequent processing was performed on the anonymized NifTI images.

2.2.1. Structural MRI Analysis

2.2.1.1 Clinical Standard of Care Orbital Segmentation

The axial T1W and T2W clinical standard of care orbital MRI images were segmented using multi-atlas segmentation [178]. Separate T1W and T2W axial orbital MRI atlases were used, each consisting of 20 orbital MRI images containing expert drawn labels for eye globe, optic nerve, orbital fat and rectus muscles. The resulting segmentations were then used to calculate volumetric morphological features describing common radiological descriptive anatomical measurements [92]. The metrics

computed include: volume, maximal diameter and average diameter for each of the superior, inferior, medial and lateral rectus muscles; volume and diameter of the globe; length, volume, average area and maximal diameter of the optic nerve. Whole eye orbit features calculated included the Barrett index and volume crowding index. The result was 22 bilateral features for each subject. These metrics are compared across scan sessions and across subjects with reproducibility of each metric being computed as the percent difference between measurements.

2.2.1.2 High resolution isotropic optic nerve radius estimation

The high resolution isotropic optic nerve imaging was segmented using multi-atlas segmentation [178] using an atlas of high resolution isotropic MRI contained expert labels of optic nerve, eye globe and optic chiasm. The other anatomical structures considered in the clinical standard of care imaging are not visible with this protocol. The results of the multi-atlas segmentation are used as initialization for an intensity model fitting based method to estimate the radius of the optic nerve and surrounding CSF [87, 90].

2.2.1.3 Whole-brain segmentation

The whole-brain MPRAGE acquired with Protocol 2 were affine registered to the MNI305 atlas [179] and bias corrected with N4 [180] using Advanced Normalization Tools (ANTs)[181] on the atlas and the target images. Non-rigid registration was performed from atlas images to the target image using Advanced Normalization Tools (ANTs) and symmetric image normalization algorithm (SyN)[182]. Image and label volumes for the atlas were then deformed to the target space with bi-cubic and nearest-neighbor interpolation and fused with non-local spatial STAPLE [183, 184] and Adaboost correction [185]. Each individual voxel in the brain was labelled to one of the 133 labels obtained from the multi-atlas labelling using the BrainCOLOR protocol [186]. T1 image labels were brought back to original target space with the ANTs inverse transformation.

2.2.2. Diffusion Tensor Imaging Analysis

Diffusion tensor imaging quality analysis reports were generated to ensure data quality and perform first level analyses including motion correction and goodness of fit metrics [144, 187-190].

2.2.3. Optical Coherence Tomography Analysis

The macular OCT images were segmented using a random forest classifier based method to segment 8 layers of the retina [191]. These layer segmentations are then reported as average layer thicknesses within different sectors of the macula which surround the fovea. Sectors are defined as the central 1mm diameter area surrounding the fovea, the inner 3mm diameter ring in superior, inferior, nasal and temporal directions and the outer 6mm diameter ring in the same directions with the rest of the image being described as just macula[192].

3. Results

3.1. MRI Results

Table VII-2 shows population averages and standard deviations for all 44 metrics for each of the scan measurements split between measurements from the T1w and T2w axial orbital images. It can be noted that some metrics, such as right optic nerve average area display a difference in population means between T1w and T2w imaging. While others such as the globe diameter appear relatively similar across imaging modalities.

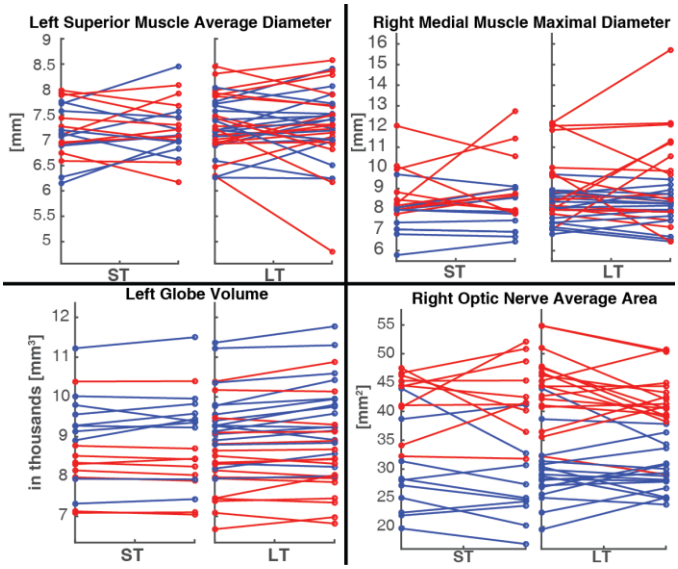

Figure VII-2. Raw short- (left) and long-term (right) reproducibility for four selected metrics showing T2w (red) and T1w (blue) measurements to illustrate reliability and stability of various metrics as well as T1w/T2w bias (bottom right).

Further visualization of four of these metrics can be seen in Figure VII-2 which shows the short- and long-term reproducibility of each of the four metrics. The red lines show measurements from T2w scans while the blue lines show

measurements from T1w scans. Each short-term panel will have 20 lines (10 subjects for T1w and T2w) while each long-term panel has 26 lines (13 subjects for T1w and T2w). Again we note that some metrics, such as right optic nerve average area (lower right), show a bias in T1w measurements compared to T2w measurements while other metrics, such as left superior muscle average diameter (top left), do not.

Also, the stability of metrics varies depending on scale as well as the nature of the measurement. Left globe volume (bottom left) is more stable than left superior muscle average diameter (top left) and right medial muscle maximal diameter (top right). However, left superior muscle average diameter (top left) is more stable than right medial muscle maximal diameter (top right) as the maximal diameter is more susceptible to segmentation errors than the average muscle diameter.

Figure VII-3 shows the reproducibility of average muscle diameter metrics as compared across

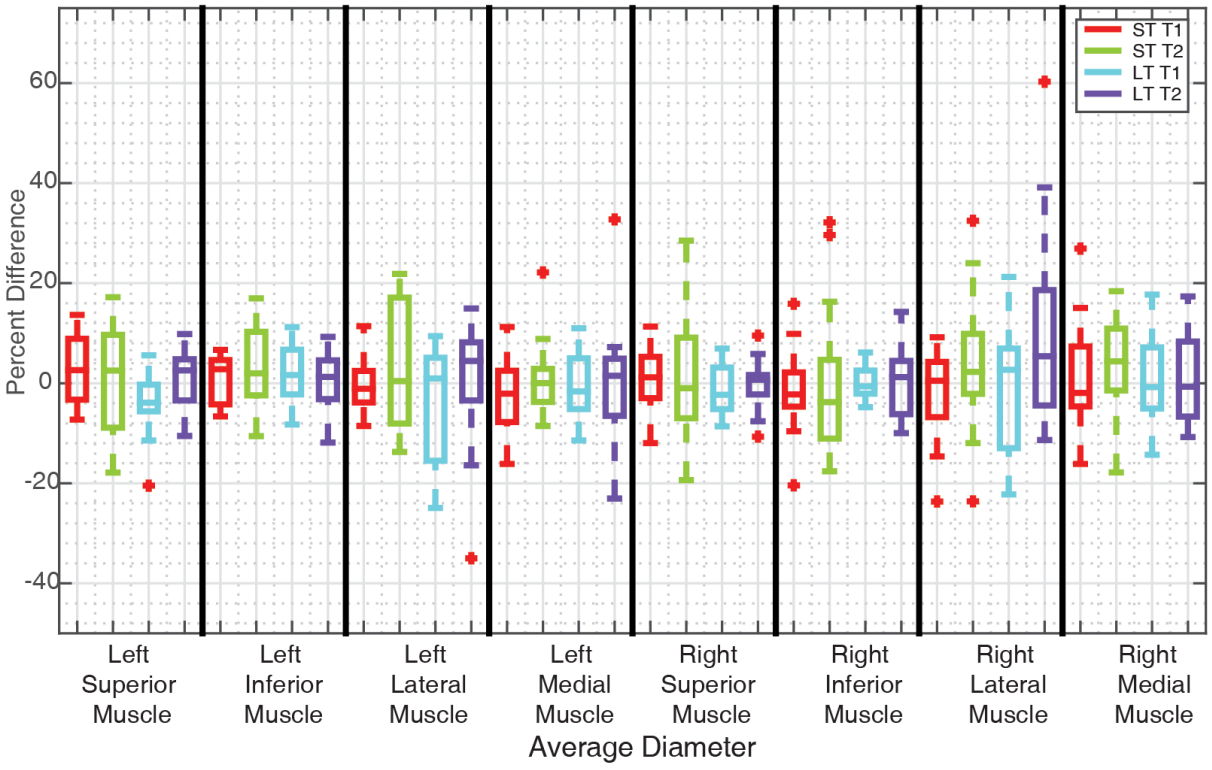

Figure VII-3. Reproducibility as percent difference between corresponding short- and long-term reproducibility scans for T1w and T2w scans for the average diameter of the eight rectus muscles. Illustrating greater reliability of muscle metrics from T1w imaging over T2w imaging and the stability of both short- and long-term muscle metric reproducibility.

short- and long-term reproducibility using both T1w and T2w measurements. Reproducibility for all 44 metrics aggregated across all subjects can be seen in Table VII-3. Further visualizations of metric reproducibility are available in supplementary material. Figure VII-3 shows reproducibility for all 8 rectus muscles' average diameter and it is easily apparent that T1w measurements of muscle diameter are more reliable than T2w measurements. Short- and long-term percent differences were not significantly different for T1w and T2w measurements (Wilcoxon rank-sum; $p<0.01$). T1w and T2w percent differences were not significantly different for short- or long-term measurements (Wilcoxon sign-rank; $p<0.01$);

3.2. OCT Results

Table VII-4 shows population averages and standard deviations for all 17 macular OCT volumes acquired with Protocol 2. As expected, the central fovea is thinnest especially the retinal nerve fiber layer. Also, the retinal nerve fiber layer is thicker in the inner region superiorly and inferiorly as retinal ganglion cells carry visual information away from the fovea. While the outer region has the thickest retinal nerve fiber layer nasally as the cells converge on the optic nerve head.

4. Discussion and Conclusions

Metrics computed from T1w and T2w MRI showed variable reliability and reproducibility as would be expected from these modalities. The two modalities are shown to have inherent bias in the measurement of optic nerve size, likely due to the fact that these modalities are eliciting different contrast from the tissue and therefore any measurements made along contrast boundaries are likely measuring different anatomical structures. The optic nerve is part of the central nervous system and therefore contains all three meningeal layers. Our results would indicate that T1w and T2w contrast of the optic nerve occurs at different layers. This is further evidence that more sophisticated MRI acquisition schemes [89] and processing pipelines [87, 90] are required for understanding of any underlying anatomical changes occurring in the optic nerve.

Imaging metrics should be chosen carefully and their susceptibility for artifactual or segmentation

error influence should be accounted for. Metrics which measure mean or standard deviation are more reliable than maximal metrics for example. These metrics could also be made more resistant to artifactual segmentation errors by incorporating robust estimators into their calculation.

The nature of the imaging is also shown to be important in metric accuracy for rectus muscle measurements in Figure VII-3 where we see the superior reliability of T1w metrics for average muscle diameter. This is not surprising since the T1w contrast in the muscles is greater than that of T2w imaging. This is further evidence that contrast-to-noise ratio of an image directly impacts segmentation and morphological feature calculation performance.

Herein we have presented a comprehensive acquisition and processing dataset for optic nerve characterization. We have acquired a wide range of optic nerve imaging sequences utilizing both MRI and OCT. We have automatically computed metrics based upon these imaging modalities and demonstrated their short- and long-term stability and reliability.

Table VII-1. MRI acquisition protocols and sequence parameters

			Scan Time		Acquired Resolution (mm)			
Sequence	**Target**	**Orientation (type)**	**Minutes**	**Seconds**	**Left-right**	**Ant-pos**	**Foot-head**	**SENSE (direction)**
Triplanar Survey	Localizer	-	0	30	250	250	50	-
B1 Calibration		Axial	0	31	8	10	8	-
T2W	Localizer	Axial (MS)	0	30	1.2	0.9	4	2(RL)
T2W	Localizer	Sagittal (MS)	0	36	4	1.2	0.9	2(AP)
T2W	Localizer	Coronal (MS)	0	30	1.2	4	0.9	2(RL)
mDixon test	Coronal	Coronal (MS)	0	8	1	3	1	2(RL)
quantitative Magnetization Transfer (qMT)	qMT	Coronal (MS)	6	41	1	3	1	2(RL)
Multi-Flip Angle (MFA)	qMT	Coronal (MS)	1	58	1.25	3	1.25	2(RL)
B0 Map	qMT	Coronal (MS)	0	21	2	3	2	-
B1 Map	qMT	Coronal (MS)	0	34	2	3	2	-
Clinical T1W Spin Echo	Structural	Axial (MS)	3	21	0.88	0.7	2	-
High resolution isotropic T2W TSE	Structural	Axial (3D)	7	48	0.55	0.55	0.55	2(RL)
Clinical T1W Spin Echo	Structural	Coronal (MS)	3	20	0.88	3	0.7	-
Clinical T2W Turbo Spin Echo	Structural	Axial (MS)	2	48	0.88	0.7	3	-
Clinical T2W Turbo Spin Echo	Structural	Coronal (MS)	2	48	0.88	3	0.7	-
T1W Fast Field Echo[1]	Structural	Axial (3D)	4	28	1	1	1	2(AP)
MPRAGE[2]	Structural	Axial (3D)	4	53	1	1	1	2(RL)
FLAIR	Structural	Sagittal (3D)	4	53	1.1	1.1	1.1	2.6(AP)/2.0(RL)
B0 Map[2]	Diffusion	Axial	0	57	3	3	2.5	-
Diffusion Tensor Imaging (DTI)[2]	Diffusion	Axial	10	8	2.5	2.5	2.5	2.2(AP)
			57	43				

[1]=Only included in Protocol 1

[2]=Only included in Protocol 2

Table VII-2. Population averages and standard deviations of all MRI metrics

	Rectus Muscle Volume							
	Left Superior	Left Inferior	Left Lateral	Left Medial	Right Superior	Right Inferior	Right Lateral	Right Medial
Baseline T1	1489.47± 240.36	1127.22± 420.38	1057.26± 231.27	923.05± 186.57	1638.32± 302.05	896.49± 266.96	992.87± 173.85	875.60± 185.80
Baseline T2	1611.60± 431.98	1223.52± 376.86	1487.50± 448.74	1127.93± 467.46	1512.17± 414.45	956.83± 216.87	1431.63± 515.87	1003.04± 309.62
ST T1	1489.74± 214.65	1248.33± 389.78	956.15± 218.45	925.42± 194.34	1602.40± 272.77	1011.87± 362.21	981.61± 212.71	861.51± 227.71
ST T2	1602.81± 385.11	1163.54± 174.27	1277.76± 306.64	1258.07± 582.52	1499.01± 369.17	988.18± 292.96	1246.88± 290.81	1007.97± 305.40
LT T1	1536.58± 291.02	1178.13± 375.80	1042.95± 237.51	949.84± 155.54	1597.32± 368.37	957.64± 358.04	1011.09± 148.97	928.31± 174.05
LT T2	1655.02± 455.83	1377.70± 261.74	1453.68± 426.38	1275.00± 345.71	1645.37± 375.09	1098.04± 244.91	1520.22± 493.30	1011.61± 307.74
All T1	1506.94± 250.92	1172.36± 391.72	1029.99± 229.31	933.47± 173.90	1615.36± 316.24	944.17± 319.96	997.16± 170.78	892.02± 189.13
All T2	1625.74± 422.74	1267.46± 308.30	1429.40± 413.22	1210.58± 450.24	1558.54± 387.99	1015.83± 247.99	1424.21± 469.45	1007.28± 301.14
All Scans	1566.34± 350.82	1219.91± 353.79	1229.70± 388.28	1072.02± 366.89	1586.95± 353.14	980.00± 286.94	1210.68± 411.70	949.65± 256.69
	Rectus Muscle Average Diameter							
	Left Superior	Left Inferior	Left Lateral	Left Medial	Right Superior	Right Inferior	Right Lateral	Right Medial
Baseline T1	7.14± 0.53	6.22± 0.68	5.73± 0.55	6.08± 0.61	7.46± 0.69	5.84± 0.38	5.69± 0.42	6.07± 0.70
Baseline T2	7.31± 0.62	6.45± 0.85	6.54± 0.81	6.11± 1.22	7.19± 0.73	5.90± 0.40	6.54± 0.90	5.76± 0.68
ST T1	7.23± 0.51	6.35± 0.66	5.48± 0.57	6.07± 0.67	7.44± 0.65	6.10± 0.48	5.70± 0.63	5.96± 0.79
ST T2	7.24± 0.59	6.43± 0.49	6.08± 0.65	6.33± 1.36	7.06± 0.69	5.95± 0.50	6.25± 0.68	5.86± 0.88
LT T1	7.28± 0.60	6.21± 0.63	5.73± 0.60	6.19± 0.47	7.41± 0.75	5.76± 0.73	5.75± 0.41	6.19± 0.61
LT T2	7.28± 0.88	6.70± 0.58	6.43± 0.82	6.34± 0.87	7.29± 0.65	6.11± 0.44	6.61± 0.96	5.75± 0.72
All T1	7.21± 0.54	6.24± 0.65	5.67± 0.57	6.12± 0.56	7.44± 0.69	5.87± 0.56	5.71± 0.46	6.09± 0.68
All T2	7.28± 0.71	6.54± 0.69	6.40± 0.79	6.24± 1.12	7.20± 0.68	5.99± 0.44	6.50± 0.87	5.78± 0.73
All Scans	7.25± 0.63	6.39± 0.68	6.04± 0.77	6.18± 0.88	7.32± 0.69	5.93± 0.50	6.11± 0.80	5.93± 0.72
	Rectus Muscle Maximal Diameter							
	Left Superior	Left Inferior	Left Lateral	Left Medial	Right Superior	Right Inferior	Right Lateral	Right Medial
Baseline T1	9.09± 0.57	8.81± 1.46	7.69± 1.41	8.15± 0.80	9.56± 0.66	7.99± 1.06	7.36± 0.82	7.89± 0.94
Baseline T2	11.21± 1.27	9.87± 1.53	9.44± 1.54	10.29± 2.34	11.29± 1.27	8.74± 1.15	9.29± 1.27	9.38± 1.66
ST T1	9.32± 0.70	9.22± 1.47	6.94± 0.76	7.91± 0.88	9.43± 0.76	8.80± 1.32	7.61± 1.26	7.67± 0.97
ST T2	11.62± 1.48	8.99± 0.99	9.12± 1.36	10.63± 2.18	11.34± 1.03	9.06± 0.80	9.10± 1.12	9.35± 1.67
LT T1	9.14± 0.89	8.30± 1.15	7.32± 1.11	8.19± 0.69	9.50± 0.74	7.92± 1.29	7.28± 0.81	8.04± 0.87

LT T2	11.20± 1.52	10.54± 1.44	9.42± 1.04	11.15± 2.05	11.63± 1.41	9.33± 1.16	9.49± 1.58	9.58± 2.37
All T1	9.16± 0.72	8.71± 1.37	7.39± 1.20	8.11± 0.77	9.51± 0.70	8.14± 1.23	7.39± 0.91	7.90± 0.91
All T2	11.30± 1.39	9.92± 1.49	9.36± 1.31	10.68± 2.19	11.42± 1.26	9.03± 1.09	9.32± 1.34	9.45± 1.91
All Scans	10.23± 1.54	9.32± 1.55	8.38± 1.59	9.40± 2.08	10.47± 1.40	8.58± 1.24	8.36± 1.50	8.67± 1.68
	Barrett Index		Globe Volume		Globe Diameter		Optic Nerve Curvilinear Length	
	Left	Right	Left	Right	Left	Right	Left	Right
Baseline T1	0.52± 0.06	0.48± 0.07	9317.13± 1015.44	9376.04± 1076.87	26.07± 0.95	26.13± 1.00	32.41± 1.80	33.07± 2.43
Baseline T2	0.69± 0.27	0.67± 0.29	8304.91± 1016.40	8206.99± 1103.81	25.09± 1.01	24.98± 1.11	27.68± 4.37	28.42± 2.41
ST T1	0.48± 0.08	0.49± 0.06	9363.96± 1105.51	9346.51± 1076.71	26.11± 1.04	26.10± 1.02	32.52± 2.31	32.98± 3.50
ST T2	0.69± 0.15	0.56± 0.05	8221.04± 939.44	8166.46± 944.07	25.01± 0.93	24.95± 0.95	26.91± 3.14	28.13± 2.68
LT T1	0.51± 0.05	0.51± 0.07	9609.13± 1015.10	9693.86± 1055.93	26.35± 0.92	26.42± 0.94	32.74± 3.03	32.89± 3.57
LT T2	0.65± 0.12	0.63± 0.07	8391.91± 1065.57	8282.54± 1054.85	25.17± 1.05	25.06± 1.05	28.35± 4.32	28.66± 3.12
All T1	0.51± 0.06	0.49± 0.07	9435.22± 1020.63	9487.08± 1057.31	26.18± 0.94	26.23± 0.97	32.56± 2.38	32.98± 3.06
All T2	0.68± 0.20	0.63± 0.20	8318.83± 998.83	8226.10± 1031.21	25.10± 0.99	25.00± 1.03	27.76± 4.07	28.45± 2.69
All Scans	0.59± 0.17	0.56± 0.16	8877.03± 1150.43	8856.59± 1216.78	25.64± 1.10	25.62± 1.17	30.16± 4.10	30.71± 3.66
	Optic Nerve Straight-line Length		Optic Nerve Volume		Optic Nerve Average Area		Optic Nerve Maximal Diameter	
	Left	Right	Left	Right	Left	Right	Left	Right
Baseline T1	26.80± 2.08	26.03± 1.68	709.54± 133.79	710.01± 163.24	26.96± 4.69	28.41± 5.97	7.43± 0.82	7.61± 0.71
Baseline T2	22.58± 2.90	23.13± 2.32	923.96± 183.08	973.05± 178.02	43.20± 7.70	43.94± 6.34	10.63± 0.77	10.48± 0.93
ST T1	26.71± 1.99	26.09± 2.25	676.93± 172.88	664.11± 168.06	25.71± 6.43	26.68± 6.83	7.12± 0.79	7.30± 0.86
ST T2	23.01± 1.47	23.35± 2.12	820.21± 182.63	950.99± 130.06	37.80± 7.52	43.07± 6.37	9.93± 1.15	10.69± 0.95
LT T1	27.16± 2.20	26.16± 2.17	731.20± 143.59	735.62± 112.94	27.49± 4.83	29.48± 4.10	7.43± 0.69	7.65± 0.66
LT T2	23.02± 3.33	23.39± 2.71	890.90± 277.99	944.73± 162.33	40.24± 8.84	42.17± 5.28	10.08± 1.06	10.48± 0.69
All T1	26.91± 2.07	26.09± 1.95	710.45± 144.50	709.50± 146.83	26.88± 5.08	28.43± 5.54	7.36± 0.76	7.56± 0.72
All T2	22.83± 2.79	23.27± 2.38	889.19± 221.64	957.79± 160.01	40.93± 8.21	43.10± 5.89	10.27± 1.00	10.53± 0.84
All Scans	24.87± 3.19	24.68± 2.59	799.82± 206.62	833.64± 197.24	33.91± 9.79	35.76± 9.31	8.82± 1.71	9.04± 1.68
	Eye Orbital Volume		Volume Crowding Index					
	Left	Right	Left	Right				
Baseline T1	24885.36± 2920.66	24532.95± 2716.34	1.44± 0.15	1.46± 0.16				
Baseline T2	24942.84± 3444.07	24563.37± 3158.55	1.50± 0.41	1.39± 0.29				

ST T1	24922.92± 2856.84	24200.89± 2470.01	1.45± 0.15	1.50± 0.15				
ST T2	25030.05± 2309.78	24458.44± 1966.88	1.36± 0.16	1.32± 0.15				
LT T1	25671.27± 2709.02	25323.90± 2688.53	1.43± 0.15	1.45± 0.16				
LT T2	25521.72± 3200.10	25073.71± 3094.41	1.48± 0.25	1.40± 0.19				
All T1	25183.97± 2792.18	24753.07± 2636.84	1.44± 0.15	1.47± 0.16				
All T2	25175.73± 3086.36	24729.17± 2870.82	1.46± 0.31	1.38± 0.22				
All Scans	25179.85± 2926.74	24741.12± 2741.15	1.45± 0.24	1.42± 0.20				

Table VII-3. Mean and standard deviation reproducibility of all MRI metrics

	Rectus Muscle Volume							
	Left Superior	Left Inferior	Left Lateral	Left Medial	Right Superior	Right Inferior	Right Lateral	Right Medial
Short-Term T1	3.34±16.46	20.39±60.17	-9.44±14.44	2.36±11.91	2.58±13.23	11.74±52.89	2.99±9.46	3.28±9.00
Short-Term T2	4.57±17.99	8.63±38.54	-5.45±24.40	2.58±32.17	6.22±15.67	7.42±33.40	-4.67±12.02	5.35±33.19
Long-Term T1	1.05±13.14	23.75±65.66	-3.25±10.99	-0.62±11.12	-4.47±15.18	21.52±63.26	0.16±4.94	2.13±12.74
Long-Term T2	-2.49±16.46	22.39±48.99	0.12±26.72	36.95±66.77	5.66±12.32	23.81±49.89	8.48±25.62	3.36±23.23
	Rectus Muscle Average Diameter							
	Left Superior	Left Inferior	Left Lateral	Left Medial	Right Superior	Right Inferior	Right Lateral	Right Medial
Short-Term T1	2.51±7.25	1.09±11.35	-4.51±7.31	0.93±6.09	1.21±4.99	3.47±9.00	1.95±5.82	0.38±6.04
Short-Term T2	-0.51±5.73	3.31±12.15	-4.25±12.21	-0.52±15.18	-2.15±7.78	1.77±8.63	-0.34±6.76	0.79±14.88
Long-Term T1	1.34±6.21	0.82±12.73	-1.00±4.88	-0.28±4.79	-1.07±7.88	-0.32±14.57	0.16±3.10	-0.01±7.01
Long-Term T2	-1.56±8.48	4.22±13.66	-1.37±12.03	9.74±19.46	1.51±10.14	4.35±9.10	1.17±8.94	1.19±9.04
	Rectus Muscle Maximal Diameter							
	Left Superior	Left Inferior	Left Lateral	Left Medial	Right Superior	Right Inferior	Right Lateral	Right Medial
Short-Term T1	4.55±4.87	0.39±17.17	-9.99±13.91	-2.20±7.24	-0.00±7.16	5.62±9.65	4.13±10.17	1.66±6.15
Short-Term T2	6.49±8.96	-1.45±11.73	1.23±18.96	3.53±26.89	3.77±6.32	9.79±9.13	3.96±15.43	5.64±21.18
Long-Term T1	0.26±7.88	-3.48±19.91	-4.78±13.96	-1.87±5.54	-0.78±6.68	2.10±20.49	-1.47±6.21	-0.31±6.13
Long-Term T2	-1.08±12.81	5.86±13.47	0.49±15.66	14.96±24.42	1.77±9.83	6.70±12.56	1.70±14.01	3.98±22.36

	Barrett Index		Globe Volume		Globe Diameter		Optic Nerve Curvilinear Length	
	Left	Right	Left	Right	Left	Right	Left	Right
Short-Term T1	-4.47±25.52	8.47±25.42	1.30±2.79	0.29±1.83	0.42±0.92	0.09±0.61	0.23±7.56	0.77±11.07
Short-Term T2	17.28±36.90	-4.94±15.97	-0.52±0.95	-0.33±2.37	-0.17±0.32	-0.11±0.79	-2.10±15.54	1.44±8.66
Long-Term T1	0.30±15.69	8.91±18.43	2.26±2.66	2.53±3.28	0.74±0.88	0.83±1.08	1.23±8.57	0.23±11.98
Long-Term T2	2.61±34.32	-0.44±22.88	0.55±2.91	0.23±2.10	0.17±0.96	0.07±0.69	2.17±16.73	0.47±13.71
	Optic Nerve Straight-line Length		Optic Nerve Volume		Optic Nerve Average Area		Optic Nerve Maximal Diameter	
	Left	Right	Left	Right	Left	Right	Left	Right
Short-Term T1	-0.65±2.82	0.47±3.70	-4.61±17.80	-5.96±10.51	-4.31±17.73	-6.00±12.92	-4.55±4.55	-2.86±6.07
Short-Term T2	-0.78±8.18	2.09±8.25	-6.47±9.84	3.48±10.59	-4.29±11.58	2.68±15.28	-4.45±9.76	4.74±9.17
Long-Term T1	0.58±2.24	-0.31±4.56	1.12±10.96	1.62±13.68	0.93±11.17	2.25±13.82	-0.41±6.44	-0.83±7.28
Long-Term T2	1.92±17.05	-0.07±10.51	-3.23±22.83	-4.22±12.79	-4.92±14.17	-4.16±11.21	-4.57±8.96	-0.42±5.97
	Eye Orbital Volume		Volume Crowding Index					
	Left	Right	Left	Right				
Short-Term T1	0.39±4.19	0.44±4.00	0.92±5.64	1.47±7.51				
Short-Term T2	0.59±3.60	-0.26±5.09	-3.45±6.32	2.70±11.57				
Long-Term T1	1.92±5.24	1.81±4.54	0.11±6.78	0.27±6.64				
Long-Term T2	2.22±4.61	2.14±3.86	-0.26±11.80	-0.70±9.93				

Table VII-4. Average and standard deviations of OCT segmentation thicknesses averaged over the central fovea (1mm diameter), inner regions (1-3mm diameter), outer regions (3-6mm diameter) and the rest of the macula

		Inner				Outer				
Region	Center	Superior	Inferior	Nasal	Temporal	Superior	Inferior	Nasal	Temporal	Macula
RNFL	9.35±1.01	27.17±2.99	27.47±2.56	21.90±2.20	17.57±1.22	41.11±4.41	40.94±4.25	44.47±4.18	19.89±2.04	34.71±3.24
GCL+IPL	34.75±8.34	95.79±4.10	94.43±4.55	94.31±4.14	91.65±4.78	71.54±5.52	68.76±5.99	79.25±6.14	77.35±5.61	73.74±4.42
INL	20.80±4.23	43.58±1.88	44.40±1.86	43.27±2.32	41.46±2.10	36.33±2.31	36.00±2.46	38.95±1.79	37.86±2.34	36.67±1.66
OPL	15.53±2.80	22.09±1.33	23.89±2.50	22.80±3.31	21.85±1.18	20.58±0.98	21.79±1.29	22.56±1.36	21.36±0.65	21.18±0.89
ONL	91.95±7.65	73.81±5.86	68.72±6.32	76.48±7.37	74.14±5.50	64.04±5.18	55.72±4.95	62.41±6.12	60.89±5.14	63.68±5.09
IS	23.22±1.10	18.61±0.90	18.37±0.96	19.36±1.14	19.04±0.65	16.78±0.61	16.21±0.48	17.02±0.66	16.49±0.46	17.18±0.49
OS	35.57±1.46	28.94±1.28	28.61±1.00	29.52±1.29	29.00±1.09	27.67±0.86	28.01±0.94	27.51±0.88	27.46±0.50	28.33±0.53
RPE	32.40±2.18	33.25±2.62	32.61±2.18	33.18±2.47	32.47±2.11	33.40±2.11	31.80±2.17	32.55±2.12	32.45±1.94	32.57±1.96
Total	263.59±17.84	343.23±8.46	338.50±9.52	340.82±9.23	327.18±9.27	311.44±9.89	299.22±12.79	324.74±12.68	293.75±11.05	308.08±8.81

Chapter VIII. Structural-Functional Relationships between Clinical Eye Orbital MRI and Visual Assessments

1. Introduction

The onset of eye diseases and impairment of vision are often accompanied by changes in physical characteristics of eye orbital structures. These changes in orbital structures may play a significant role in the progression or recurrence of eye diseases. Magnetic resonance imaging (MRI) of the eye orbit can be used to assess the risk and progression of optic diseases and visual loss [22]. Imaging data after damage to the orbit of the eye in trauma situations can be related to decline in visual function [21]. Orbital metrics of the eye such as Barrett Index have also been shown to be associated with dysthyroid optic neuropathy in patients with Graves' orbitopathy [19-20].

Other studies show on a case-by-case basis that orbital structure does not just have an effect on eye function, but can also be used as a predictive measure for the decline of visual function [19-21]. The orbit is a complex environment—many different factors affect orbital structure and loss of vision. However, these studies suggest that a deeper relationship exists between orbital structure and the onset of optic conditions. The goal of this study was to explore the relationship between clinical and structural metrics by correlating large sets of structural metrics (e.g., Barrett Index) with the clinically obtained visual field scores (e.g., visual acuity score). This was done in order to determine if a relationship between the two could be obtained, or if a general statistical model for the relationship between the orbital structure metrics of the eye and visual field scores can be determined.

The subjects in this study were selected because they had magnetic resonance imaging (MRI) performed on the orbit of the eye as a regular part of their clinical care. They all had clinical visual disability scores available as well. An experienced undergraduate manually labeled approximately 20 subjects of each MRI contrast mechanism. Then, multi-atlas segmentation was performed to segment the extraocular rectus muscles, eye globes, optic nerves, and orbital fat [2,3]. Twenty-one different structural metrics were then calculated from the segmentation pipelines. For each visual metric, a stepwise

regression function fit a generalized linear model to a Poisson distribution in order to determine the amount of variance in visual function metrics that can be explained by the structural metrics of the eye orbit.

2. Methods

2.1. Patient Data

The relationship between visual function and MRI-derived orbital structures were investigated in a retrospective cohort of patients at Vanderbilt University Medical Center. Subjects were selected based on both having met clinical criteria for eye disease and undergoing MRI imaging as part of their regular clinical care. The eye diseases incorporated in this study are: *Thyroid Eye Disease*: toxic diffuse goiter without thyrotoxic crisis or storm (242.00), endocrine exophthalmos (376.2*), thyrotoxic exophthalmos (376.21), exophthalmic opthalmoplegia (376.22); *Orbital Inflammation*: acute inflammation of the orbit (376.0), acute inflammation of the orbit unspecified (376.00), orbital cellulitis (376.01), orbital periotisis (376.02), chronic inflammation of orbit unspecified (376.10), orbital granuloma (376.11), orbital myositis (376.12); *Optic Nerve Edema*: benign intracranial hypertension (348.2); *Glaucoma*: low-tension open angle glaucoma (365.12); *Intrinsic Optic Nerve Disease*: optic neuritis (377.3), optic neuritis unspecified (377.30), optic pappilitis (377.31), retrobular neuritis (acute), nutritional optic neuropath (377.33), toxic optic neuropathy (377.34), other optic neuritis (377.39), other disorders of the optic nerve (377.4), ischemic optic neuropathy (377.41), hemorrhage in optic nerve sheaths (377.42), optic nerve hypoplasia (377.43), other disorders of the optic nerve (377.49).

The study was conducted on 241 subjects (157 female) over 510 scan sessions. Each of the sessions had an instance of visual function testing available within 6 months of the scan. Visual function was assessed using the American Medical Association Functional Vision Score (FVS), which is calculated based on visual acuity and visual field testing acquired through routine clinical care. FVS is described through a subset of four other scores. The Visual Acuity Scores (VAS) of the left and right eyes

was combined with the better VAS of both eyes in a weighted manner to calculate the Functional Acuity Score (FAS). The Visual Field Scores (VFS) of the left and right eyes were combined with the better VFS of both eyes in a weighted manner to calculate the Functional Field Score (FFS). The FVS is calculated using the resulting FAS and FFS. [1]

2.2. Image Processing

Segmentation of the MRI data for computation of image-derived anatomical metrics was based off a previously described multi-atlas segmentation method [86, 178], which automatically segments the optic nerves (including the surrounding CSF), extraocular rectus muscles, eye globes, and orbital fat. This method uses 20 manually labeled atlas images, which include healthy controls as well as multiple sclerosis patients. Three atlases, T2W, FLAIR and proton density weighted images, each consisting of 20 images, were used in this study. Each target scan type was manually assigned to an atlas based on contrast similarity, with T1w imaging being segmented with FLAIR atlases due to similar orbital contrast. The

target image to be segmented was registered to each of the 20 atlas images using an affine registration [107]. The sum of the globe labels was used as a probability map in a majority voting fashion, and the area corresponding to >50% globe probability, or 10 atlases, was used to compute the centroids of the two eye globes. These centroids were dilated by 30mm in the left-right direction, 40mm in the superior-inferior direction, 60mm posterior direction, and 30mm anterior direction. The cropped images were segmented using an affine and non-rigid registration of cropped atlases [143]. The manual labels of the atlas images were transformed to the target space using these registrations and are fused using non-local spatial STAPLE (NLSS) [114, 144]. Kalman filters were used to isolate the Superior Rectus Muscle, Inferior Rectus Muscle, Lateral Rectus Muscle and Medial Rectus Muscle from the muscle labels obtained from the multi-atlas segmentation pipeline [8].

From the segmented orbital structures a MATLAB program computed both traditional radiology measures and novel morphological metrics and generated a set of descriptive features for each patient. For each of the segmented structures, volume and size features were calculated. These include: volume,

Table VIII-1. ICD-9 codes for disease cohorts

Disease	ICD-9 codes	Description
Thyroid Eye Disease	242.00	Toxic diffuse goiter without thyrotoxic crisis or storm
	376.2	Endocrine exophthalmos
	376.21	Thyrotoxic exophthalmos
	376.22	Exophthalmic ophthalmoplegia
Orbital Inflammation	376.0, 376.00	Acute inflammation of orbit
	376.01	Orbital cellulitis
	376.02	Orbital periostitis
	376.1	Chronic inflammation of orbit
	376.11	Orbital granuloma
	376.12	Orbital myositis
	373.13	Abscess of eyelid
Optic Nerve Edema	348.2	Idiopathic intracranial hypertension
	377.0, 377.00	Papilledema
	377.01	Papilledema, increased intracranial pressure
	377.02	Papilledema, decreased ocular pressure
Glaucoma	365.0*	Borderline glaucoma
	365.1*	Open-angle glaucoma
	365.2*	Primary angle-closure glaucoma
	365.3*	Corticosteroid-induced glaucoma
	365.4*	Glaucoma associated with congenital anomalies, dystrophies, and systemic syndromes
	365.5*	Glaucoma associated with disorders of the lens
	365.6*	Glaucoma associated with other ocular disorders
	365.7*	Glaucoma stage, unspecified
	365.8*	Other specified forms of glaucoma
	365.9*	Unspecified glaucoma
Intrinsic Optic Nerve Disease	377.3*	Optic Neuritis
	377.4*	Other disorders of optic nerve

maximum diameter, and average diameter for the superior, inferior, medial, and lateral rectus muscles [9-12]; volume and diameter of the globe[193-196]; and length, volume, average area, and maximum diameter of the optic nerve[197, 198]. Features that describe the eye orbit as a whole were also calculated. These include: orbital volume; Barrett index[199]; and the volume crowding index[200]. All 21 features are calculated bilaterally for each patient.

2.3. Statistical Modeling

For each of the nine visual function targets (right eye VAS, left eye VAS, both eyes VAS, right eye VFS, left eye VFS, both eyes VFS, FAS, FFS, FVS), a forward stepwise univariate regression procedure (stepwiseglm, MATLAB 2014b, Mathworks, Natick, MA) was conducted with the structural metrics listed above. Structural metrics are combined at the subject level using a median, assuming no significant changes across multiple scan sessions each within 6 months of the visual assessment. Significant individual correlates (t statistic) were reported along with the coefficient of variation R^2 for each regression. The models were created for all patient data overall as well as within disease subgroups with enough subjects for statistical power. The base regression model was

$$y = \beta_1 x_1 + \cdots + \beta_n x_n \quad \text{(VIII.1)}$$

where y is a visual function metric and $x_1 \ldots x_n$ are structural metrics derived from the MRI data. Since the visual scores are integer values the response variable was fit to a Poisson distribution. This model is applied to all subjects, subjects within each of the five disease cohorts (when enough subjects are present), with only lateral eye metrics and outcomes, and with age, sex, years since diagnosis and age*sex effects added.

3. Results

3.1. Image Processing

Using the multi-atlas segmentation pipeline, 1,995 MRI volumes across the 510 scan sessions were associated with a contrast atlas and labeled with optic nerves (including the sub-arachnoid CSF), extraocular rectus muscles, eye globes, and orbital fat. Radiological and morphological features were calculated for each image volume.

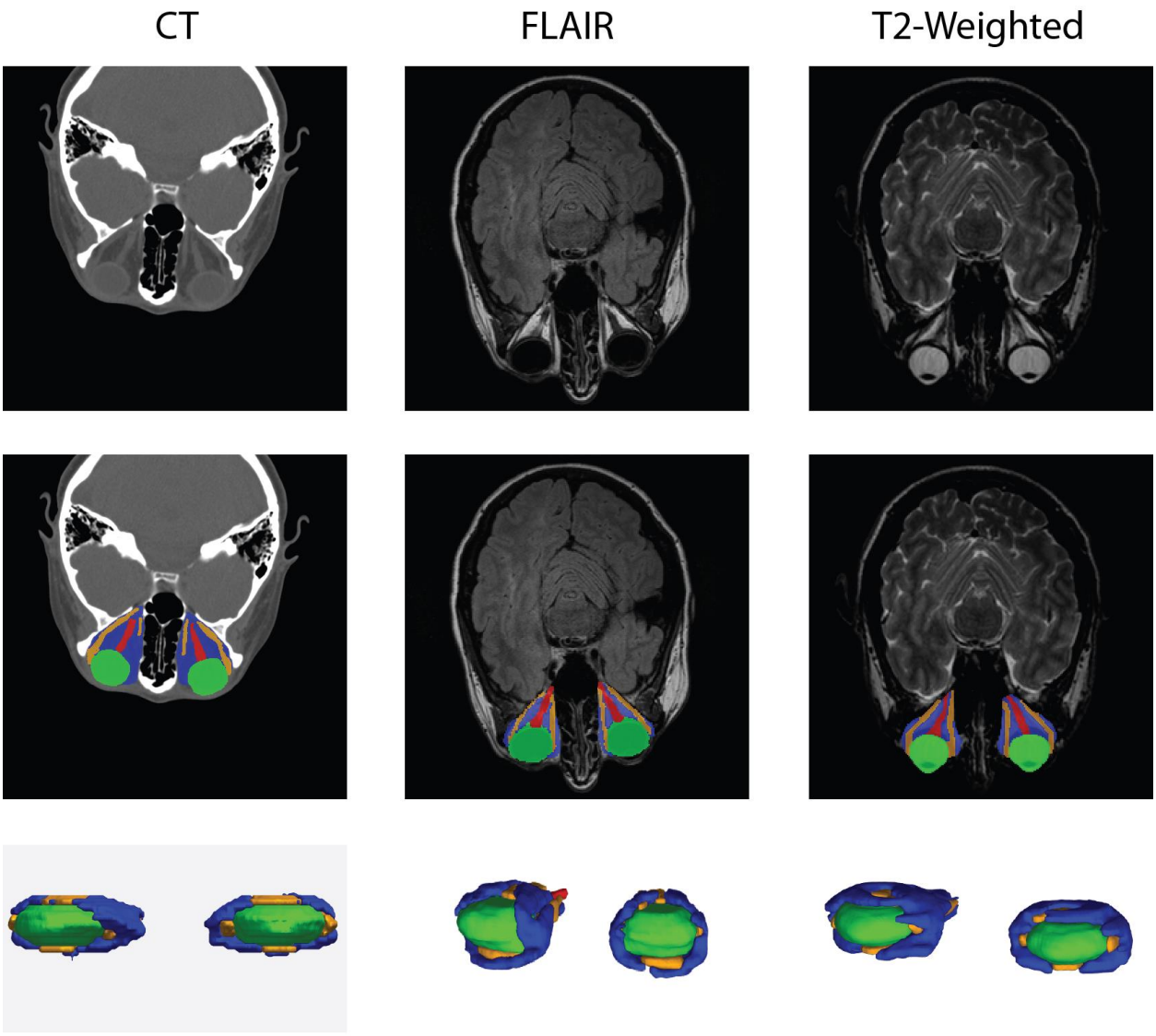

Figure VIII-1. Example CT and MRI scans (top row) were expertly labeled (center row, lower row) and used in multi-atlas segmentation pipelines.

3.2. Statistical Modeling

All 1,995 sets of morphological features were combined using the median of all measurements. Three subjects were excluded from analysis because their optic nerve length measurements were >3 standard deviations from the mean. Each visual function measurement was regressed with all the structural metrics from both eyes as shown in Table VIII-2. These nine regression models were all significant ($p < 0.001$). The structural metrics were separated into left eye structural metrics and right eye structural metrics. RVAS and RVFS were regressed with the right eye structural metrics, and LVAS and

LVFS were regressed with the left eye structural metrics. These four regression models were all significant ($p < 0.001$). As noted in Table VIII-2, the fraction of variance explained by all four models in the second set of regressions were less than the amounts of variance explained in their corresponding models in first set of regressions using structural metrics from both eyes, indicating significant explanatory power in contra-lateral metrics. Each visual function measurement was also regressed with all structural metrics from both eyes within each of the three disease cohorts with enough subjects. The other two disease cohorts were excluded from this analysis as they contained only 12 subjects (thyroid eye disease) and 38 subjects (glaucoma) which the authors determined was not a reasonable number of subjects for any amount of significant results. Within the subjects with ICD-9 codes included in the edema cohort we can see that the variance explained is much higher than that of all subjects and the addition of age, sex and age*sex terms even further increase variance explained. The same trend can be seen for orbital inflammation subjects. The subjects within the optic neuropathy cohort have similar results to that of the regression with all subjects included. We also note that for all models we capture more variance in visual field metrics than in visual acuity metrics. This is likely due to the fact that visual acuity is measured as best corrected visual acuity and power is lost with corrective lenses as compared to uncorrected visual field measures.

Table VIII-2. Explanatory R^2 for various regression models. All models significant at p<0.001.

R-squared (ordinary)	LVFS	RVFS	LVAS	RVAS	VFS	VAS	FFS	FAS	FVS
All Subjects	0.203	0.194	0.158	0.225	0.145	0.084	0.174	0.132	0.190
Corresponding eyes	0.126	0.067	0.016	0.057	-	-	-	-	-
Edema (90 Subjects)	0.478	0.376	0.438	0.338	0.383	0.170	0.434	0.187	0.449
Edema + age/sex	0.499	0.392	0.482	0.338	0.390	0.170	0.434	0.187	0.461
Orbital Inflammation (90 Subjects)	0.476	0.480	0.376	0.379	0.366	0.124	0.438	0.213	0.443
Orbital Inflammation + age/sex	0.530	0.511	0.485	0.374	0.364	0.124	0.438	0.213	0.456
Optic Neuropathy (144 Subjects)	0.250	0.292	0.196	0.306	0.265	0.091	0.274	0.102	0.261
Optic Neuropathy + age/sex	0.269	0.292	0.223	0.323	0.276	0.091	0.277	0.102	0.254

4. Discussion and Conclusion

This research explores the macro relationship between eye orbit structural metrics and visual function measurements. The results indicate a significant relationship between structural and visual metrics. The results show broad correlation between structural metrics and visual function with limited explanatory power and significant contra-lateral explanatory power. This analysis is further refined by breaking down the metrics into manually stratified disease cohorts which represent similar disease processes. By doing so our models can better capture variability and increase explanatory power of the models. This would indicate that although the predictive power of broad structural-functional relationships is limited, within disease cohorts there are trends which are more powerful predictors. These results agree with literature on disease processes in that orbital inflammation and edema cause gross morphological changes in eye orbit structure which meaningfully correspond to visual deficits. Optic neuropathy is not known to have gross morphological changes on orbital structures and therefore has similar predictive power to the overall cohort of all disease subtypes. By separating similar disease groups we are able to better model the disease process and explain visual function loss through structural changes.

This study is limited in its scope and understanding of underlying disease processes. Further investigation into the strongest predictors of visual function loss could yield interesting insights into morphological changes which impact visual field. More detailed analysis of changes in visual field according to regions of loss could yield interesting effects of morphological changes on regional visual field deficits. More subjects for each disease cohort would increase the predictive power and refine results. Another limitation of this work is its lack of incorporation of time dependence on data. We define the broad window of 6 months for associating a visual assessment with an imaging study as well as then aggregating all scans for a single subject. A more refined treatment of the time course variability of these effects would also increase study reliability and applicability.

Chapter IX. Numerical Optimization of Quantitative Magnetization Transfer Sampling Schemes

1. Introduction

Quantitative magnetization transfer (qMT) sampling schemes have not changed drastically since the earliest implementations and have been based off uniform sampling of the MT z-spectrum [71, 201, 202]. Previous work attempted to numerically optimize qMT of the brain through numerical propagation of error, but similar studies have not been attempted to obtain robust estimates of qMT-derived indices in the human spinal cord [203]. In this work we use Monte Carlo fitting of simulated data to optimize a qMT acquisition protocol to improve the accuracy of the pool-size ratio (PSR) estimation in the human spinal cord in vivo. We will begin by formulating our qMT model from the Bloch equations, then proceed to describe the experiments conducted to optimize and validate qMT sampling.

2. Background

Magnetization transfer (MT) is a known effect within biological systems in which an off resonance saturation pulse will transfer magnetization to free, mobile, water protons through cross relaxation [204]. This type of interaction is typically modeled with a two-pool, or binary-spin-bath, model. The two-pool model contains a free water (liquid) pool and a semisolid pool of hydrogen protons bound to semi-solid macromolecules [70]. The mobility of protons within each of these pools differs and a quantitative description of this model will represent the relative size of each of the pools as well as the magnetic properties of both pools. In this work we utilize pulsed z-spectroscopic imaging and extend our model as follows from previous works [202, 205].

As a starting point of our derivation we begin with the model of pulsed cross-relaxation which extends the Bloch equations for two spins coupled by cross-relaxation:

$$\frac{dM_x^F}{dt} = -\frac{M_x^F}{T_2^F} - 2\pi\Delta M_y^F \tag{IX.1}$$

$$\frac{dM_y^F}{dt} = 2\pi\Delta M_x^F - \frac{M_y^F}{T_2^F} - \gamma B_1(t) M_z^F \quad \text{(IX.2)}$$

$$\frac{dM_z^F}{dt} = \gamma B_1(t) M_y^F - (R_1^F + k) M_z^F + k\frac{(1-f)}{f} M_z^B + R_1^F(1-f) \quad \text{(IX.3)}$$

$$\frac{dM_z^B}{dt} = -\left[R_1^B + k\frac{1-f}{f} + \pi\gamma^2 B_1^2(t) g(\Delta, T_2^B)\right] M_z^B + k M_z^F + R_1^B f \quad \text{(IX.4)}$$

Where $M_{x/y/z}^{F/B}$ is the x-, y- and z-components of the magnetization of the free (F) or bound (B) pool. Δ and $B_1(t)$ are the offset frequency and amplitude of the RF saturation pulse. $R_1^{F/B}$ is the inverse of the longitudinal relaxation time ($T_1^{F/B}$) for the free or bound pool. k is the effective relaxation rate of magnetization from the free to bound pools. γ is the gyromagnetic ratio. f is related to PSR as $f = \frac{PSR}{1+PSR}$. $g(\Delta, T_2^B)$ is the absorption line-shape of the bound pool spins, or the amount of absorption of the bound pool at a given offset frequency. Although there are a number of choices for this absorption line shape function we use the superLorentzian function which has been shown to have the best fit to experimental data of any single-parameter line shapes [206, 207]. Any line shapes which better fit experimental data require more parameters and are therefore more difficult to fit [208]. Since the goal of this work is to reduce scan times and produce accurate fits with the least number of offsets we choose to adopt the best single parameter lineshape.

$$g(\Delta, T_2^B) = \sqrt{\frac{2}{\pi}} \int_o^{\pi/2} \frac{T_2^B}{|3\cos^2\theta - 1|} \exp\left[-2\left(\frac{2\pi\Delta T_2^B}{3\cos^2\theta - 1}\right)^2\right] \sin\theta \, d\theta \quad \text{(IX.5)}$$

With the underlying equations formalized above we now turn to the MT-prepared spoiled gradient echo pulse sequence which can be broken down into four distinct segments in which Equations V.1-(IX.4) need to be solved. These four time intervals are: (1:s) off-resonance saturation, (2:d) delay for spoiling, (3:p) readout pulse and (4:r) delay for signal readout and relaxation. For simplicity we assume that the direct effect of the off-resonance saturation on the free pool is negligible and the sequence is

ideally spoiled [209]. We define the magnetization vector $\mathbf{M}_i$ as the z-magnetization of the free and bound pools at the end of each of time intervals, i.

$$\mathbf{M}_i = \begin{bmatrix} M_z^F(t = t_i) \\ M_z^B(t = t_i) \end{bmatrix}, i = \text{ s,d,p,r} \tag{IX.6}$$

We also assume that the time-dependant RF amplitude, $B_1(t)$, can be approximated as a square-wave RF pulse of constant amplitude and the same duration with effective amplitude, B_{1e}, defined such that:

$$B_{1e} = \sqrt{\int_0^{t_s} {B_1}^2(t)dt/t_m} \tag{IX.7}$$

These simplifications allow us to solve Equations V.1-(IX.4) for the saturation time interval ($i =$ s):

$$\mathbf{M}_\text{s} = \exp[(\mathbf{R} + \mathbf{W})t_\text{s}] \cdot \mathbf{M}_\text{r} + \left[\mathbf{I} - \exp\big((\mathbf{R} + \mathbf{W})t_\text{s}\big)\right] \cdot \mathbf{M}_{\boldsymbol{ss}} \tag{IX.8}$$

Where $\mathbf{R}$ is the relaxation matrix:

$$\mathbf{R} = \begin{bmatrix} -R_1^F - k & k\dfrac{1-f}{f} \\ k & -R_1^B - k\dfrac{1-f}{f} \end{bmatrix} \tag{IX.9}$$

$\mathbf{I}$ is the 2x2 identity matrix; $\mathbf{W}$ is the diagonal matrix:

$$\mathbf{W} = -\text{diag}(W^F, W^B) \tag{IX.10}$$

Where the elements $W^{F,B}$ is the average saturation rate for the free or bound pool respectively

$$W^{F,B} = \pi\gamma^2 B_{1e}^2 g(\Delta, T_2^{F,B}) \tag{IX.11}$$

Note that the line shape, $g(\Delta, T_2^{F,B})$, is superLorentzian for the reasons described above for the bound pool but follows a Lorentzian distribution for the free pool which follows from the Bloch equations [210].

$$g(\Delta, T_2^F) = \frac{T_2^F}{\pi} \frac{1}{1 + (2\pi\Delta T_2^F)^2} \tag{IX.12}$$

The steady-state magnetization vector, $\mathbf{M}_{\boldsymbol{ss}}$, is:

$$\mathbf{M}_{ss} = \frac{1}{D}\begin{bmatrix}(1-f)(A+R_1^F W^B)\\ f(A+R_1^B W^F)\end{bmatrix} \tag{IX.13}$$

Where A is the determinant of the relaxation matrix, $\mathbf{R}$:

$$A = R_1^F R_1^B + R_1^F k\frac{1-f}{f} + R_1^B k \tag{IX.14}$$

And D is:

$$D = A + (R_1^F + k)W^B + \left(R_1^B + k\frac{1-f}{f}\right)W^F + W^F W^B \tag{IX.15}$$

The non-irradiated case can be solved by analyzing Equations V.3 and (IX.4) at $B_1 = 0$;

$$\mathbf{M}_{\mathrm{d,r}} = \exp\left(\mathbf{R}t_{\mathrm{d,r}}\right)\cdot\mathbf{M}_{\mathrm{d,r}} + \left(\boldsymbol{I} - exp(\boldsymbol{R}t_{d,r})\right)\cdot\mathbf{M}_{\mathrm{eq}} \tag{IX.16}$$

Where the equilibrium magnetization, $\mathbf{M}_{\mathrm{eq}}$, is:

$$\mathbf{M}_{\mathrm{eq}} = \begin{bmatrix}1-f\\ f\end{bmatrix} \tag{IX.17}$$

The readout pulse ($i = \mathrm{p}$) is described by a flip angle (α). We accept the conventional assumption that the readout pulse has no effect on the bound pool:

$$\mathbf{M}_{\mathrm{p}} = \mathbf{C}\cdot\mathbf{M}_{\mathrm{s}} \tag{IX.18}$$

Where $\mathbf{C}$ is the diagonal matrix,

$$\mathbf{C} = \mathrm{diag}\,(\cos\alpha, 0) \tag{IX.19}$$

Using Equations (IX.8), (IX.13) and (IX.16) we can solve for the z-component of the free pool magnetization directly before the readout pulse which will be proportional to our signal intensity. For simplicity we define some repetitive terms as:

$$\begin{aligned}\mathbf{E}_{\mathrm{s}} &= \exp\left[(\mathbf{R}+\mathbf{W})t_{\mathrm{s}}\right]\\ \mathbf{E}_{\mathrm{d}} &= \exp\left(\mathbf{R}t_{\mathrm{d}}\right)\\ \mathbf{E}_{\mathrm{r}} &= \exp\left(\mathbf{R}t_{\mathrm{r}}\right)\end{aligned} \tag{IX.20}$$

Using these terms we can write the z-component of the free pool magnetization before the

readout pulse as:

$$\mathbf{M}_{zs}^{F} = \{\, \boldsymbol{I} - \exp[\boldsymbol{R}(t_s + t_d + t_r)] \cdot exp(\boldsymbol{W}t_s) \cdot \boldsymbol{C}\}^{-1} \cdot \left\{[\boldsymbol{E}_s \cdot \boldsymbol{E}_d \cdot (\boldsymbol{I} - \boldsymbol{E}_r) + (\boldsymbol{I} - \boldsymbol{E}_d)] \cdot \mathbf{M}_{\boldsymbol{eq}} + [\boldsymbol{E}_d \cdot (\boldsymbol{I} - \boldsymbol{E}_s)] \cdot \mathbf{M}_{\boldsymbol{ss}}\right\} \quad \text{(IX.21)}$$

This formulation is quite intuitive but it is useful computationally to compute the inverse term first and check for singularity which occurs as $f \to 0$. This formulation allows for us to simulate a given qMT experiment or fit this model to experimental data.

3. Methods

3.1. qMT Model Implementation

The qMT model was implemented in Matlab (Natick, Massachusetts). Estimation of empirical data is done by sequential fitting of T_1 to multi flip angle (MFA) using the signal equation:

$$M_z = \frac{1 - \exp\left(-\frac{TR}{T_1}\right)}{1 - \cos\theta \, \exp\left(-\frac{TR}{T_1}\right)} \sin\theta \quad \text{(IX.22)}$$

Where TR is the repetition time for the MFA acquisition and θ is the excitation flip angle for each acquisition of the MFA. The Matlab optimization function lsqnonlin is used to fit three parameters, f, k and T_2^B. We use R_1^F from the MFA fit and assume $R_1^F = R_1^B$ and we also use the assumption that $T_2^F R_1^F = 0.0232$ to estimate T_2^F [211].

3.2. Optimization

To optimize the sampling scheme for qMT z-spectra, we started with a log-linearly spaced sampling scheme and iteratively swapped points with those from a denser sampling scheme, accepting the

permutation with the lowest PSR mean squared error. The initial model comprised of 8 offset frequencies evenly distributed in log-space from 15Hz – 100kHz at two RF MT saturation powers, 900° and 1200°. A denser sample set of 32 offsets at these same two powers were generated as possible sampling points. The swapping of each original point was evaluated iteratively by evaluating the mean squared error of PSR estimation of each potential model using 10,000 Monté Carlo simulations of Gaussian random noise at SNR=100. The best performing swap (or the original model) was chosen and the next point was then evaluated. Once all 16 points in the original model had been evaluated for superior performance, the final model consisted of the sampling scheme in Table IX-1, column 2. Figure I.1 shows a graphical representation of the three sampling schemes evaluated including the original starting scheme (left) and the optimized scheme (middle).

3.3. Acquisition

One healthy volunteer was imaged using a 3.0T Achieva whole body scanner (Philips, The Netherlands). A two-channel transmit body coil was used for excitation and a 16-channel SENSE neurovascular coil for reception. A volume centered near C2-C3 was selected from a T2-weighted survey image. qMT data were acquired over this volume using a 3D MT-prepared spoiled gradient echo sequence. MT-preparation used a 20ms single-lobe sinc-Gauss pulse, saturation flip angle (α_{MT}) and offset frequencies ($\Delta\omega$) as well as other imaging parameters prescribed in Table IX-1, FOV=150x150x60mm^3 , resolution = 1.0x1.0x5.0mm^3, 2 signal averages. B_1 was measured in the same volume using the actual flip angle imaging method TR1/TR2=30/130ms, α=60°)[177]; ΔB_0 from gradient echo phase images acquired (ΔTE=2.3ms)[176]; and T_1 using a multiple flip angle (MFA) acquisition (TR/TE=20/4.6ms, α=5, 10, 15, 20, 25, 30°). A high-resolution (0.65x0.65x5.0mm^3) multi-echo gradient echo (mFFE) anatomical image was also acquired for registration (TR/TE/ΔTE=700/6.5/8.2 ms, α=28°). Total scan time for all three sampling schemes and accompanying scans was 44 minutes.

Table IX-1. MT Acquisition Parameters

Acquisition	Log-spaced	Optimized	High offsets
α_{MT} = 900°	Δω = 15, 53, 186, 653, 2297, 8081, 28427, 100000 Hz	Δω = 47, 62, 186, 653, 1875, 32107, 42653, 100000 Hz	Δω = 1000, 1500, 2000, 2500, 8000, 16000, 32000, 100000 Hz
α_{MT} = 1200°	Δω = 15, 53, 186, 653, 2297, 8081, 28427, 100000 Hz	Δω = 15, 82, 186, 653, 2297, 7759, 56663, 75275 Hz	Δω = 1000, 1500, 2000, 2500, 8000, 16000, 32000, 100000 Hz
TR/TE/α	90/4.9ms/7°	90/4.9ms/7°	50/2.4ms/6°

3.4. Processing

All image volumes were coregistered to the MFA to correct for motion artifacts using reg_aladin from niftyreg [107]. Measurements were normalized to the highest offset acquired (>70kHz) and fit to a two-pool model[2] of the MT effect also using MFA, B_1^+ and B_0 maps for correction of field inhomogeneities and T1 variations as described above. Gray matter (GM) and white matter (WM) was manually labeled on the mFFE scan and propagated to each of the qMT fits for comparison of PSR contrast.

4. Results

Figure IX.2 shows the anatomical mFFE (left) as compared to the PSR maps generated from the log-spaced sampling scheme (A), optimized sampling scheme (B) and high offsets sampling scheme which avoids lower offsets nearer to water (C). Qualitatively the PSR map in (B) using the optimized

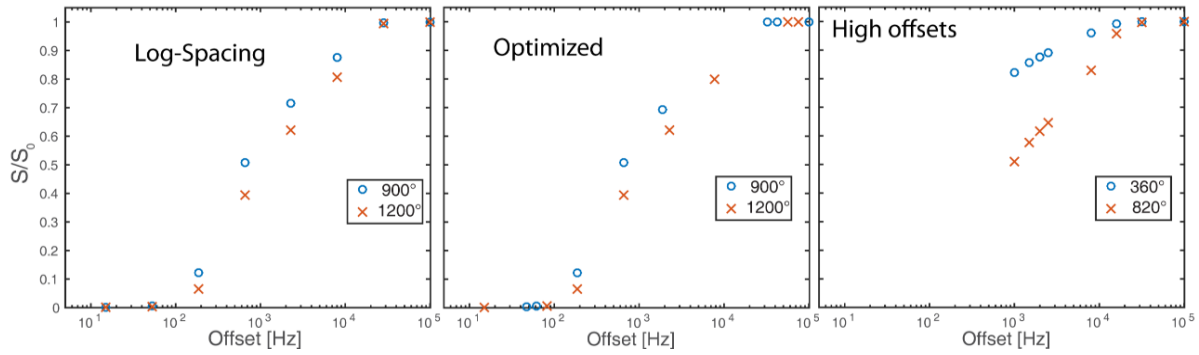

Figure IX.1. Comparison of sampling schemes showing original log-spacing (left), optimized spacing (middle) and high offsets approach (right).

sampling scheme presents the best visualization of the spinal cord GM butterfly seen in the mFFE. Figure IX.3 shows a comparison of PSR for both GM and WM. For all three methods PSR was significantly different between GM and WM by Wilcoxon rank-sum ($p<0.01$). The optimized sequence shows lower variance within WM than the other two methods while maintaining the superior contrast of the high offsets approach.

5. Discussion

These initial results are promising that numerical optimization of qMT sampling using computational modeling can translate to superior image acquisition schemes. This work presents a first proof of concept that optimizing qMT sampling schemes can improve upon current norms. The optimization framework used here is superior to the numerical propagation of error used by Levesque [203] because it more closely mimics the experimental setup of acquiring imaging with noise and fitting the empirical data numerically. This framework allows for fewer assumptions than the numerical propagation of error framework.

The use of a single subject is one limitation, more subjects would be necessary to evaluate stability of this sampling scheme. These sequences also need to be evaluated in patients with pathology to assess sensitivity to useful pathologies such as normal appearing white matter (NAWM) in patients with MS. This sensitivity analysis will be crucial in determining whether the added sensitivity from sampling optimization is necessary for detecting pathology or if current standards are sufficient. If there is no need

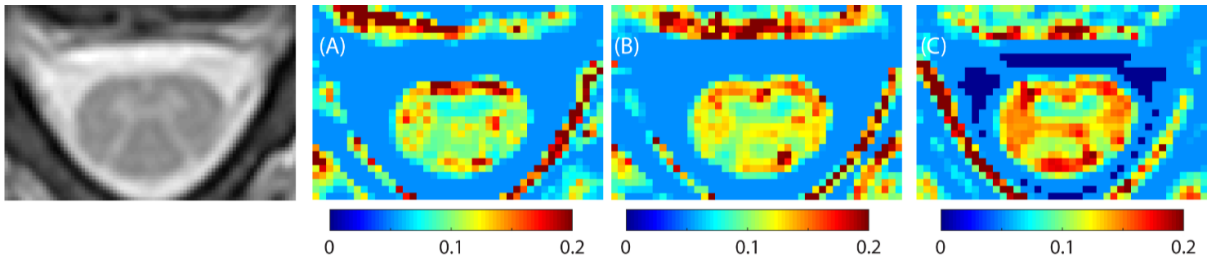

Figure IX.2. PSR map results of fitting empirical data for (A) log-spaced sampling, (B) optimized sampling and (C) high offsets sampling with mFFE for comparison (left).

for increased sensitivity to pathology this technology could be translated to optimizing qMT acquisition times by reducing the number of offsets necessary. This could increase clinical utility of qMT techniques by allowing for clinically viable scan times which are sensitive to pathology.

This work could be improved upon by optimizing for multiple underlying signal models. In this work we only optimize sampling for WM but this could be extended. A useful extension would be to simulate multimodal distributions of various tissue types such as WM, GM and NAWM and optimize detection or discrimination between them. This would be a trivial extension of this work but would require additional Monte Carlo iterations to ensure variance stability amongst all of the distributions. Also not included in this model are B_0 and B_1 inhomogeneities. While not significant in the brain other anatomies do suffer from substantial inhomogeneities which change the actual offsets and powers being acquired. In these cases it would be useful to model this uncertainty to assess sensitivity of these sampling patterns to inhomogeneities. Certain acquisition schemes could be very robust in differentiating tissue types but only if acquired accurately. In this case one would need to evaluate the tradeoff between tissue differentiation and robustness to inhomogeneities based upon the anatomy of interest and how well inhomogeneities can be corrected.

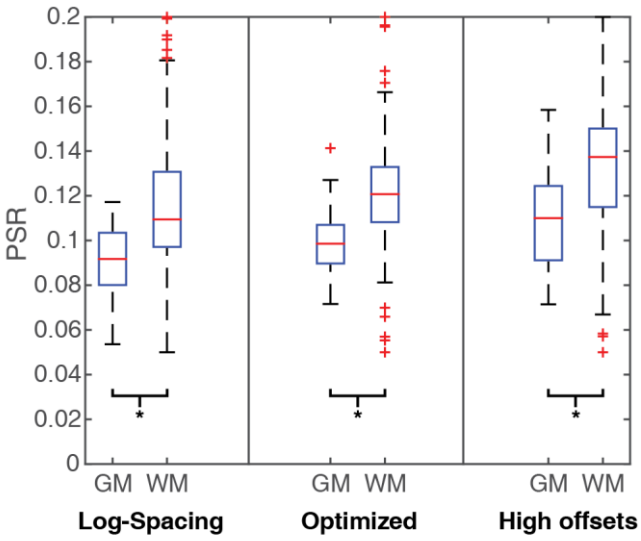

Figure IX.3. Comparison of GM/WM contrast for each of the three evaluated sampling schemes. Asterisks indicate significance by Wilcoxon rank-sum p<0.01.

This framework could also be improved by utilizing a global optimal search as opposed to an iterative approximation. The iterative approach is significantly more computationally efficient but may not yield the globally optimal sampling scheme and as discussed there may need to be evaluation of multiple sampling

schemes based upon properties of robustness to various tissues or inhomogeneities. One final area of improvement for this work would be in increasing the RF power and offset search space. We utilize only two RF powers and 32 offsets for a total search space of 64 points. However, this could be expanded to include more RF powers, assuming imaging parameters are still reasonable such as RF deposition and TR. Also each of the RF powers could be more densely sampled to include more than 32 points. This expansion of search space will make the global optimal search even more challenging. Likely the benefit of increasing the search space will outweigh the benefits of ensuring a globally optimal search although this area requires further investigation.

Chapter X. Conclusions and Future Work

1. Summary

Imaging of the optic nerve (ON), particularly MRI of the ON has long been a target of the medical imaging community. However, the last 10 years have seen limited advances in this field as many challenges facing MRI of the ON are still open areas of research today. This work focuses on addressing various challenges of ON imaging by developing robust automated processing techniques (**Chapters II, III, V**), applying these techniques to large-scale patient populations (**Chapters VI, VIII**), acquiring a reproducibility data set for comparison of techniques (**Chapters IV, VII**) and improving upon current state-of-the-art quantitative magnetization transfer (qMT) MRI to increase its applicability to small structures like the ON (**Chapter IV**).

2. Multi-Atlas Optic Nerve Segmentation

2.1. Summary

We present a multi-atlas based method optimized for automatic segmentation of eye orbital structures including eye orbital fat, optic nerve, rectus muscles and eye globe (**Chapter II**). This method is extended to be applied to multiple MRI sequence types and morphological and radiological metrics are computed from the volumetric segmentations. These metrics are applied to a large-scale retrospective patient population from VUMC of patients with imaging and coincident visual field assessments to evaluate broad structural-functional relationships in the eye orbit (**Chapter VIII**).

2.2. Main Contributions

1. We present a comparison of various eye orbital multi-atlas segmentation frameworks and compare them quantitatively based upon performance to arrive at an optimized eye orbital multi-atlas segmentation algorithm.
2. This algorithm is extended through the use of multiple atlases to automatically segment large retrospective populations of varying MRI contrast mechanisms. Multi-atlas segmentation relies on correspondence of contrast between the atlas images and target images which is not true for various contrast mechanisms in MRI. We overcome this issue by defining multiple atlases and applying the appropriate atlas for segmentation to increase the amount of data segmented from large-scale studies.
3. We extend this algorithm to automatically calculate both radiological and morphological metrics describing eye orbital structures. We utilize the volumetric labels produced by the multi-atlas segmentation technique to automatically calculate various morphological features of each eye orbital structure including radiologically defined biomarkers of disease progress.
4. These techniques are applied to a large-scale diverse retrospective patient population from Vanderbilt University Medical Center in which patients had coincident eye orbital imaging and visual assessments. We identified broad structural-functional relationships between these automatically calculated metrics and the visual field assessments conducted independently. This points towards a utility of these tools in identifying potential biomarkers of eye orbital diseases in more targeted patient populations.

2.3. Future Work

The current framework could be improved upon by automating atlas selection and atlas creation based upon input MRI contrast. The current broad definition of contrast mechanisms provides large improvements over a single set of atlas images but is time consuming for large heterogeneous data sets.

Multi-atlas segmentation is time consuming and efforts have been made to speed up multi-atlas segmentation, incorporation of these efforts would be beneficial for clinical utility [212]. The application of these techniques to a single diverse data set identifies that structural-functional relationships are present but more targeted hypotheses need to be formulated and tested within individual disease cohorts to identify clinically relevant biomarkers.

3. Non-Invasive Automatic Optic Nerve Radius Estimation

3.1. Summary

We present an optimized MRI pulse sequence for ON:CSF contrast to address challenges of MRI in the ON and enable development of ON image processing pipelines and show that this sequence is clinically viable and achieves superior contrast-to-noise ratio to current clinical standard of care imaging (**Chapter III**). An automated ON and CSF radius estimation algorithm is proposed (**Chapter III**) and improved upon (**Chapter V**) to incorporate 3-dimensional consistency and anatomical viability. This improved algorithm is applied to a population of patients with MS and shown to detect a group effect of atrophy in patients with a history of optic neuritis as compared to healthy controls while patients without a history of optic neuritis are not significantly different from healthy controls (**Chapter VI**).

3.2. Main Contributions

1. We optimized an anatomical MRI pulse sequence for the purpose of generating superior ON:CSF contrast for accurate non-invasive morphological measurements of the ON. This sequence is designed with clinical utility in mind being acquired in clinically viable time of only 8 minutes and not requiring modifications to scanner software or hardware. This sequence is shown to quantitatively provide better contrast than current clinical standard of care MRI.

2. We proposed and optimized the first automatic ON radius estimation algorithm which takes advantage of the superior contrast from this optimized pulse sequence. This algorithm overcomes the limitation of many current studies which often measure a single slice of the ON, acting as a surrogate for global ON health. This tool allows for investigation of populations with focal or global ON changes.
3. We propose a method for comparison of these ON measurements by interpolating measurements to be the same length, aligning parts of the ON as is commonly done in other anatomies such as the spinal cord. The importance of this alignment sheds further doubt on previous methodologies of single ON measurements at a predefined location posterior to the globe.
4. We develop a statistical atlas of normative ON radius measurements for comparison of patient populations to healthy controls. This atlas is shown to be stable across young healthy controls and male and female participants. We also show that these measurements are stable for both short- and long-term reproducibility.
5. We apply this tool to a patient population of MS patients both with and without a history of optic neuritis and show that patients with a history of optic neuritis are significantly different from healthy controls while patients without a history of optic neuritis are not significantly different from healthy controls. This initial application shows just one possible application of this tool to detecting global atrophy amongst patient populations and increasing our understanding of disease processes.

3.3. Future Work

The deployment of this sequence to clinical settings will be crucial in the gathering of data for further investigation with these tools. Improvements in the pulse sequence to improve resolution or signal-to-noise ratio would be beneficial to radius estimation accuracy and clinical utility. The radius estimation algorithm has been shown to be useful in detecting group population effects with realistic

effect sizes but individual patient measurements are not reliable biomarkers for disease detection or progression monitoring. Improving upon the accuracy and robustness of the radius estimation algorithm by further refining the understanding of the manifold between model parameters and radius space could improve accuracy and clinical utility. The current work can also be extended to other patient populations to detect group effects in little understood patient populations, such as glaucoma. This knowledge could still be useful clinically in defining guidelines for disease progression or treatment even if manual measurements were necessary for applicability to individual patients.

4. Short- and Long-Term Optic Nerve Imaging Reproducibility

4.1. Summary

We designed and acquired a short- and long-term ON imaging reproducibility study including whole-brain MRI, qMT of the ON with fixation to reduce motion artifacts, clinical standard of care orbital imaging, optimized ON anatomical imaging and retinal OCT imaging (**Chapter VII**). This data set is used to validate the tools described above in terms of short- and long-term reproducibility and stability (**Chapter IV**). We also show normative values for eye orbit structural morphology and retinal thickness measurements from automated OCT layer segmentation. These data will be useful for comparison of future eye orbit image processing algorithms as an independent resource for reproducibility of algorithms.

4.2. Main Contributions

1. We designed and acquired reproducibility data for non-invasive imaging of the eye orbit including, clinical standard of care anatomical imaging, optimized anatomical imaging, whole-brain anatomical imaging, ON qMT imaging and retinal OCT imaging.
2. These data are publicly released for future evaluation of reproducibility of eye orbit image processing techniques in context. Similar to useful whole brain imaging repositories currently used for challenges this resource hopefully provides motivation for

development of new eye orbit image processing techniques and fair comparison of techniques from various development centers around the world.

3. Applying the tools above we present the normative and reproducibility of eye orbit morphological metrics and OCT segmentation layer thicknesses for a population of healthy controls. Publishing normative values contributes positively to the literature of non-invasive eye orbit imaging allowing for comparison of techniques and measurements from other investigators.

4.3. Future Work

With the release of these data the hosting of a challenge would now be possible to further push the community towards developing clinically relevant image processing techniques. The inclusion of current clinical standard of care imaging allows for the evaluation of image processing techniques which can be utilized to take advantage of the large amounts of clinical imaging currently being stored at medical centers around the world. Additionally, the current state-of-the-art imaging included in this study allows for investigators without the ability to acquire their own sophisticated eye orbital MRI to develop image processing techniques and evaluate them freely.

5. Numerical Optimization of qMT Sampling

5.1. Summary

We utilize simulations to numerically optimize qMT sampling to reduce acquisition times for increased applicability of qMT imaging to small structures like the ON and spinal cord (**Chapter IX**). qMT imaging offers useful insight into tissue microstructure but comes at a cost of long scan times and high knowledge of entry barriers for new investigations. We address long scan times by optimizing qMT sampling for tissue sensitivity using established biomechanical models of MT signal and numerical simulation.

5.2. Main Contributions

1. We utilize existing biomechanical models of underlying MT signal in an iterative Monte Carlo framework to optimize qMT sampling for increased accuracy in estimation of underlying tissue properties of interest. This framework is the first of its kind to simulate qMT imaging experiments and numerical fitting to optimize sampling based upon fitting accuracy of underlying tissue parameters.
2. Using this framework we develop an optimized offset sampling scheme for estimation of pool size ratio of white matter, a quantity which has been shown to be sensitive to myelin content within a voxel and useful in investigation of demyelinating diseases and detecting areas of white matter with normal transverse and longitudinal relaxation but displaying early signs of demyelination.
3. We show that this optimized offset sampling scheme displays superior pool size ratio estimation homogeneity within white matter and gray matter as well as superior contrast between white matter and gray matter in the spinal cord of a healthy control compared to traditional qMT sampling schemes.

5.3. Future Work

While this framework presents initially promising results for improvement in qMT sampling schemes there are many areas which need further investigation. The optimization framework itself is an iterative solution and does not guarantee a globally optimal sampling scheme, optimization of computational modeling could enable a search for a globally optimal sampling scheme. The optimization performed was limited in scope for simplicity and does not account for other tissue types or transmit and main field inhomogeneities. The current framework also does not address the utility of reducing sampling to achieve more clinically relevant acquisition times. The promise of these initial results warrants further investigation into these areas and improvement upon current qMT best practices through numerical simulation.

6. Concluding Remarks

Despite the many challenges of MRI of the ON this work reflects significant advancements in the field. Despite the recent absence of large amounts of ON MRI investigation there have been advancements which enable the new study of ON through the use of MRI. There are vast opportunities now in improvement of orbital MRI imaging and processing techniques as well as application of current processing techniques to the large amounts of orbital imaging data available to researchers.

Traditional clinical orbital imaging can be improved upon without the need for complicated MRI techniques which are difficult to translate to the clinic. This ability to translate the imaging protocols to the clinic is crucial to further improvement of our understanding of ON pathology as we follow the imaging community's trend towards quantitative imaging metrics. Current clinical standard of care imaging is inferior in both contrast and resolution and these new imaging techniques offer greater accuracy in characterizing eye orbital morphology for enhanced detection of disease processes. However, implementation of these new techniques will take time and so it is also important to ensure that we develop algorithms which are applicable to clinically available data which contains latent knowledge about disease pathology which has yet to be uncovered. The algorithms derived in this work also present a multitude of avenues available for study by applying these techniques to all of the various eye orbital disease patient populations available for study in clinical imaging databases. The release of the reproducibility data set also marks an important resource for future advancements in image processing techniques and this tool will play an important role in algorithm selection and community consensus.

Non-invasive imaging techniques for the ON have seen thrusts of efforts in the past but with the tools presented here the groundwork is set for MRI to play an important role in understanding disease pathology in the future. The increased interest of clinicians and engineers in the role of MRI of the ON and the ability to answer well formulated hypotheses of eye orbital disease pathology means that the impacts of these works will likely yield fruitful investigation for some time and may prove useful as we begin to investigate other small anatomical structures of interest.

Appendix A: Publications

1. Journal Articles

1. **Robert L. Harrigan**, Alex K. Smith, Bailey Lyttle, Bailey Box, Seth A. Smith, Bennett A. Landman. "Characterization of Short- and Long-Term Stability of Non-Invasive Optic Nerve Imaging". Neuroimage. *In Preparation.*
2. Shikha Chaganti, Katrina M Nelson, **Robert L. Harrigan**, Kunal P Nabar; Naresh Nandakumar; Tara Goecks, Seth A Smith, Bennett A Landman, Louise A Mawn. "Estimated Incidence of Ophthalmic Conditions Associated with Optic Nerve Disease in Middle Tennessee." *In Preparation.*
3. Shikha Chaganti, Katrina Nelson, Kevin Mundy, **Robert L. Harrigan**, Robert Galloway, Louise A. Mawn, and Bennett A. Landman. "Imaging Biomarkers in Thyroid Eye Disease and their Clinical Associations". *In Preparation.*
4. **Robert L. Harrigan**, Alex K. Smith, Bailey Lyttle, Bailey Box, Bennett A. Landman, Francesca Bagnato, Siddharama Pawate, Seth A. Smith. "Quantitative Characterization of Optic Nerve Atrophy in Patients with Multiple Sclerosis". Multiple Sclerosis Journal. *Submitted.*
5. Andrew J. Plassard, **Robert L. Harrigan**, Swati Rane, Srivatsan Pallavaram, Pierre F. D'Haese, Daniel O. Claassen, Benoit M. Dawant, Bennett A. Landman. "Synthetic Atlases Improve Segmentation Consistency between T1-Weighted Imaging Sequences". Journal of Medical Imaging. *Submitted.*
6. Kevin Mundy, Shikha Chaganti, Michael P DeLisi, Katrina M Nelson, **Robert L. Harrigan**, Swetasudha Panda, Robert Galloway, Bennett Landman, Louse Mawn "Assessment of Orbital Computed Tomography (CT) Imaging Biomarkers in Patients with Thyroid Eye Disease". American Journal of Ophthalmology. *In Press.*
7. **Robert L. Harrigan**, Benjamin C. Yvernault, Brian D. Boyd, Stephen M. Damon, Kyla David Gibney, Benjamin N. Conrad, Nicholas S. Phillips, Baxter P. Rogers, Yurui Gao, Bennett A.

Landman "Vanderbilt University Institute of Imaging Science Center for Computational Imaging XNAT: A multimodal data archive and processing environment" Neuroimage. (2015) doi:10.1016/j.neuroimage.2015.05.021

8. **Robert L. Harrigan**, Andrew J. Plassard, Frederick W. Bryan, Gabriela Caires, Louise A. Mawn, Lindsey M. Dethrage, Siddharama Pawate, Robert L. Galloway, Seth A. Smith, Bennett A. Landman. "Disambiguating the Optic Nerve from the Surrounding Cerebrospinal Fluid: Application to MS-related Atrophy." Magnetic Resonance in Medicine. (2014) doi:10.1002/mrm.25613
9. **Robert L. Harrigan**, Swetashuda Panda, Andrew J. Asman, Katrina M. Nelson, Shikha Chaganti, Michael P. DeLisi, Benjamin C. W. Yvernault, Seth A. Smith, Robert L. Galloway, Louise A. Mawn, Bennett A. Landman. "Robust optic nerve segmentation on clinically acquired CT." Journal of Medical Imaging. 1.3 (2014) doi:10.1117/1.JMI.1.3.034006

2. Conference Publications

1. **Robert L. Harrigan**, Alex K. Smith, Louise A. Mawn, Seth A. Smith, Bennett A. Landman. "Improved Automatic Optic Nerve Radius Estimation from High Resolution MRI" In Proceedings of the SPIE Medical Imaging Conference. Orlando, Florida, February 2017. Oral Presentation.
2. Yuankai Huo, Jiaqi Liu, Zhoubing Xu, **Robert L. Harrigan**, Albert Assad, Richard G. Abramson, Bennett A. Landman. "Multi-atlas Segmentation Enables Robust Multi-contrast MRI Spleen Segmentation for Splenomegaly" In Proceedings of the SPIE Medical Imaging Conference. Orlando, Florida, February 2017. Oral Presentation.
3. Kurt G. Schilling, Vishwesh Nath, Justin Blaber, **Robert L. Harrigan**, Zhaohua Ding, Adam W. Anderson, Bennett A Landman. "Effects of b-Value and Number of Gradient Directions on Diffusion MRI Measures Obtained with Q-ball Imaging" In Proceedings of the SPIE Medical Imaging Conference. Orlando, Florida, February 2017. Oral Presentation.

4. Xiuya Yao, Shikha Chaganti, Kunal P. Nabar, Katrina Nelson, Andrew Plassard, **Robert L. Harrigan**, Louise A. Mawn, Bennett A. Landman. “Structural-Functional Relationships Between Eye Orbital Imaging Biomarkers and Clinical Visual Assessments” In Proceedings of the SPIE Medical Imaging Conference. Orlando, Florida, February 2017. Oral Presentation.
5. **Robert L. Harrigan**, Alex K. Smith, Louise A. Mawn, Seth A. Smith, Bennett A. Landman. “Short Term Reproducibility of a High Contrast 3-D Isotropic Optic Nerve Imaging Sequence in Healthy Controls. In Proceedings of the SPIE Medical Imaging Conference. San Diego, California, February 2016. Oral Presentation
6. Shikha Chaganti, Katrina Nelson, Kevin Mundy, Yifu Luo, **Robert L. Harrigan**, Steve Damon, Daniel Fabbri, Louise Mawn, Bennett Landman."Structural Functional Associations of the Orbit in Thyroid Eye Disease: Kalman Filters to Track Extraocular Muscles". In Proceedings of the SPIE Medical Imaging Conference. San Diego, California, February 2016. Oral Presentation
7. Andrew J. Plassard, **Robert L. Harrigan**, Allen T. Newton, Swati D. Rane, Srivatsan Pallavaram, Pierre F. D'Haese, Benoit M. Dawant, Daniel O. Claassen, Bennett A. Landman. "One the Fallacy of Quantitative Segmentation for T1-Weighted MRI." In Proceedings of the SPIE Medical Imaging Conference. San Diego, California, February 2016. Oral Presentation.
8. **Robert L. Harrigan**, Andrew J. Plassard, Louise A. Mawn, Robert L. Galloway, Seth A. Smith, Bennett A. Landman. "Constructing a Statistical Atlas of the Radii of the Optic Nerve and Cerebrospinal Fluid Sheath in Young Healthy Adults." In Proceedings of the SPIE Medical Imaging Conference. Orlando, Florida, February 2015. Oral Presentation. doi:10.1117/12.2081887

3. Abstracts

1. **Robert L. Harrigan**, Bennett A. Landman, Seth A. Smith. “Optimization of Quantitative Magnetization Transfer Imaging for Accurate PSR Estimation in the Spinal Cord”. International Society for Magnetic Resonance in Medicine Conference. Honolulu Hawaii, April 2017. Poster.

2. **Robert L Harrigan**, Bennett A Landman, Louise A Mawn, Siddharama Pawate, Seth A Smith. "Automatic Measurement of Optic Nerve Atrophy in Multiple Sclerosis Patients with and without Optic Neuritis in MRI". American Academy of Neurology. Vancouver, BC, Canada, April 2016. E-poster.
3. **Robert L. Harrigan**, Katrina M. Nelson, Lindsey M Dethrage, Robert L Galloway, Bennett A. Landman, Louise A. Mawn, Seth A. Smith. Mapping of the optic nerve in multiple sclerosis patients with and without optic neuritis. International Society for Magnetic Resonance in Medicine, Toronto, Ontario. June 3, 2015 E-Poster

Appendix B: Biography

Robert L. Harrigan was born in Amherst, New Hampshire in 1989. He received his B.S. degree in imaging science from Rochester Institute of Technology in Rochester, New York, in 2011, his Master's in business administration degree from The University of Tennessee at Martin, Martin, Tennessee, in 2013, and his Ph.D. degree in electrical engineering from Vanderbilt University, Nashville, Tennessee, in 2017.

Before arriving at Vanderbilt University he worked at Integrity Applications Inc. in the summer of 2010 and 2012 on algorithm development for remote sensing target detection. He also worked for Goodrich ISR Systems (now UTC Aerospace Systems) in 2011 working on airborne sensor quality analysis and threat detection algorithms. As a graduate student, his work focused on improving optic nerve MRI acquisition and analysis techniques. Through this work he had research interests in image segmentation, non-convex optimization, random forest regression, Monte Carlo simulation and quantitative magnetization transfer imaging.

Dr. Harrigan is a member of the International Society for Optics and Photonics (SPIE), the International Society for Magnetic Resonance in Medicine (ISMRM), the American Academy of Neurology (AAN), and the Association for the Advancement of Science (AAAS).

References

1. Group, O.N.S., *Multiple sclerosis risk after optic neuritis: final optic neuritis treatment trial follow-up.* Archives of neurology, 2008. **65**(6): p. 727.
2. Glaser, J.S., *Topical diagnosis: prechiasmal visual pathways.* Neuro-Ophthalmology, 1979: p. 95-198.
3. Quigley, H.A. and A.T. Broman, *The number of people with glaucoma worldwide in 2010 and 2020.* British journal of ophthalmology, 2006. **90**(3): p. 262-267.
4. Zhang, K., L. Zhang, and R.N. Weinreb, *Ophthalmic drug discovery: novel targets and mechanisms for retinal diseases and glaucoma.* Nat Rev Drug Discov, 2012. **11**(7): p. 541-59.
5. Quigley, H.A., E.M. Addicks, and W.R. Green, *Optic nerve damage in human glaucoma: III. Quantitative correlation of nerve fiber loss and visual field defect in glaucoma, ischemic neuropathy, papilledema, and toxic neuropathy.* Archives of Ophthalmology, 1982. **100**(1): p. 135-146.
6. Quigley, H.A., G.R. Dunkelberger, and W.R. Green, *Chronic human glaucoma causing selectively greater loss of large optic nerve fibers.* Ophthalmology, 1988. **95**(3): p. 357-363.
7. Arnold, A.C., *Evolving management of optic neuritis and multiple sclerosis.* American journal of ophthalmology, 2005. **139**(6): p. 1101-1108.
8. Foroozan, R., et al., *Acute demyelinating optic neuritis.* Current opinion in ophthalmology, 2002. **13**(6): p. 375-380.
9. Balcer, L.J., *Optic neuritis.* New England Journal of Medicine, 2006. **354**(12): p. 1273-1280.
10. Hayreh, S., *Anterior ischemic optic neuropathy.* Clinical neuroscience (New York, NY), 1996. **4**(5): p. 251-263.
11. Arnold, A.C., *Pathogenesis of nonarteritic anterior ischemic optic neuropathy.* Journal of neuro-ophthalmology, 2003. **23**(2): p. 157-163.
12. Beck, R.W., et al., *Optic disc structure in anterior ischemic optic neuropathy.* Ophthalmology,

1984. **91**(11): p. 1334-1337.

13. Hayreh, S.S. and M.B. Zimmerman, *Non-arteritic anterior ischemic optic neuropathy: role of systemic corticosteroid therapy*. Graefe's Archive for Clinical and Experimental Ophthalmology, 2008. **246**(7): p. 1029-1046.
14. Atkins, E.J., et al., *Treatment of nonarteritic anterior ischemic optic neuropathy*. Survey of ophthalmology, 2010. **55**(1): p. 47-63.
15. Jenkin, D., et al., *Optic glioma in children: surveillance, resection, or irradiation?* International Journal of Radiation Oncology* Biology* Physics, 1993. **25**(2): p. 215-225.
16. Weizman, L., et al., *Automatic segmentation, internal classification, and follow-up of optic pathway gliomas in MRI*. Medical image analysis, 2012. **16**(1): p. 177-188.
17. Boppart, S.A., et al., *Intraoperative assessment of microsurgery with three-dimensional optical coherence tomography*. Radiology, 1998. **208**(1): p. 81-86.
18. Ide, T., et al., *Intraoperative use of three-dimensional spectral-domain optical coherence tomography*. Ophthalmic surgery, lasers & imaging: the official journal of the International Society for Imaging in the Eye, 2009. **41**(2): p. 250-254.
19. Fercher, A., K. Mengedoht, and W. Werner, *Eye-length measurement by interferometry with partially coherent light.* Optics letters, 1988. **13**(3): p. 186-188.
20. Gabriele, M.L., et al., *Optical coherence tomography: history, current status, and laboratory work.* Investigative ophthalmology & visual science, 2011. **52**(5): p. 2425-2436.
21. Tuulonen, A. and P.J. Airaksinen, *Initial glaucomatous optic disk and retinal nerve fiber layer abnormalities and their progression.* American journal of ophthalmology, 1991. **111**(4): p. 485-490.
22. Schuman, J.S., et al., *Quantification of nerve fiber layer thickness in normal and glaucomatous eyes using optical coherence tomography: a pilot study.* Archives of Ophthalmology, 1995. **113**(5): p. 586-596.
23. Bowd, C., et al., *The retinal nerve fiber layer thickness in ocular hypertensive, normal, and glaucomatous eyes with optical coherence tomography.* Archives of Ophthalmology, 2000. **118**(1):

p. 22-26.

24. Wollstein, G., et al., *Comparison of three optical coherence tomography scanning areas for detection of glaucomatous damage.* American journal of ophthalmology, 2005. **139**(1): p. 39-43.
25. Medeiros, F.A., et al., *Detection of glaucoma progression with stratus OCT retinal nerve fiber layer, optic nerve head, and macular thickness measurements.* Investigative ophthalmology & visual science, 2009. **50**(12): p. 5741-5748.
26. Jørgensen, T.M., et al., *Enhancing the signal-to-noise ratio in ophthalmic optical coherence tomography by image registration—method and clinical examples.* Journal of biomedical optics, 2007. **12**(4): p. 041208-041208-10.
27. Ricco, S., et al., *Correcting motion artifacts in retinal spectral domain optical coherence tomography via image registration*, in *Medical Image Computing and Computer-Assisted Intervention–MICCAI 2009*. 2009, Springer. p. 100-107.
28. Wollstein, G., et al., *Optical coherence tomography longitudinal evaluation of retinal nerve fiber layer thickness in glaucoma.* Archives of ophthalmology, 2005. **123**(4): p. 464-470.
29. Petzold, A., et al., *Optical coherence tomography in multiple sclerosis: a systematic review and meta-analysis.* The Lancet Neurology, 2010. **9**(9): p. 921-932.
30. Frohman, E., et al., *Optical coherence tomography in multiple sclerosis.* The Lancet Neurology, 2006. **5**(10): p. 853-863.
31. Kallenbach, K. and J. Frederiksen, *Optical coherence tomography in optic neuritis and multiple sclerosis: a review.* European journal of neurology, 2007. **14**(8): p. 841-849.
32. Gordon-Lipkin, E., et al., *Retinal nerve fiber layer is associated with brain atrophy in multiple sclerosis.* Neurology, 2007. **69**(16): p. 1603-1609.
33. Henderson, A.P., et al., *An investigation of the retinal nerve fibre layer in progressive multiple sclerosis using optical coherence tomography.* Brain, 2008. **131**(1): p. 277-287.
34. Frohman, E.M., et al., *Optical coherence tomography: a window into the mechanisms of multiple sclerosis.* Nature Clinical Practice Neurology, 2008. **4**(12): p. 664-675.

35. Bloch, F., *Nuclear induction.* Physical review, 1946. **70**(7-8): p. 460.

36. Purcell, E.M., H. Torrey, and R.V. Pound, *Resonance absorption by nuclear magnetic moments in a solid.* Physical review, 1946. **69**(1-2): p. 37.

37. Nagayama, K., et al., *Two-dimensional J-resolved 1 H nmr spectroscopy for studies of biological macromolecules.* Biochemical and biophysical research communications, 1977. **78**(1): p. 99-105.

38. Hahn, E.L., *Spin echoes.* Physical review, 1950. **80**(4): p. 580.

39. Bernstein, M.A., K.F. King, and X.J. Zhou, *Handbook of MRI pulse sequences*. 2004: Elsevier.

40. de Bazelaire, C.M., et al., *MR imaging relaxation times of abdominal and pelvic tissues measured in vivo at 3.0 T: preliminary results 1.* Radiology, 2004. **230**(3): p. 652-659.

41. Stanisz, G.J., et al., *T1, T2 relaxation and magnetization transfer in tissue at 3T.* Magnetic Resonance in Medicine, 2005. **54**(3): p. 507-512.

42. Selwood, P., *Tables de Constantes et Données Numériques. Organisme Affilié de l'Union Internationale de Chimie Pure et Appliquée. No. 7. Constantes Sélectionnées. Diamagnétisme et Paramagnétisme*. Journal of the American Chemical Society, 1958. **80**(11): p. 2915-2915.

43. Schenck, J.F., *The role of magnetic susceptibility in magnetic resonance imaging: MRI magnetic compatibility of the first and second kinds.* Medical physics, 1996. **23**(6): p. 815-850.

44. Stenger, V.A., F.E. Boada, and D.C. Noll, *Three‐dimensional tailored RF pulses for the reduction of susceptibility artifacts in T* 2‐weighted functional MRI.* Magnetic resonance in medicine, 2000. **44**(4): p. 525-531.

45. Czervionke, L., et al., *Magnetic susceptibility artifacts in gradient-recalled echo MR imaging.* American journal of neuroradiology, 1988. **9**(6): p. 1149-1155.

46. Bahill, A.T., M.R. Clark, and L. Stark, *The main sequence, a tool for studying human eye movements.* Mathematical Biosciences, 1975. **24**(3): p. 191-204.

47. Takahashi, K. and Y. Atsumi, *Precise measurement of individual rapid eye movements in REM sleep of humans.* Sleep, 1997. **20**(9): p. 743-752.

48. Daniels, D., et al., *Magnetic resonance imaging of the optic nerves and chiasm.* Radiology, 1984. **152**(1): p. 79-83.

49. Miller, D., et al., *Magnetic resonance imaging of the optic nerve in optic neuritis.* Neurology, 1988. **38**(2): p. 175-175.

50. Hickman, S., et al., *Detection of optic nerve atrophy following a single episode of unilateral optic neuritis by MRI using a fat-saturated short-echo fast FLAIR sequence.* Neuroradiology, 2001. **43**(2): p. 123-128.

51. Hickman, S.J., et al., *Continuing optic nerve atrophy following optic neuritis: a serial MRI study.* Mult Scler, 2002. **8**(4): p. 339-42.

52. Hickman, S.J., et al., *A serial MRI study following optic nerve mean area in acute optic neuritis.* Brain, 2004. **127**(Pt 11): p. 2498-505.

53. Toosy, A.T., D.F. Mason, and D.H. Miller, *Optic neuritis.* The Lancet Neurology, 2014. **13**(1): p. 83-99.

54. Rizzo III, J.F., C.M. Andreoli, and J.D. Rabinov, *Use of magnetic resonance imaging to differentiate optic neuritis and nonarteritic anterior ischemic optic neuropathy.* Ophthalmology, 2002. **109**(9): p. 1679-1684.

55. Huber, D.J., E. Mueller, and P. Heubes, *Oblique magnetic resonance imaging of normal structures.* American journal of roentgenology, 1985. **145**(4): p. 843-846.

56. Haik, B.G., et al., *Manetic Resonance, Imaging in the Evaluation of Optic Nerve Gliomas.* Ophthalmology, 1987. **94**(6): p. 709-717.

57. Gass, A., et al., *Lesion discrimination in optic neuritis using high-resolution fat-suppressed fast spin-echo MRI.* Neuroradiology, 1996. **38**(4): p. 317-321.

58. Barker, G., *Technical issues for the study of the optic nerve with MRI.* Journal of the neurological sciences, 2000. **172**: p. S13-S16.

59. Weigel, M., et al., *Fast and quantitative high-resolution magnetic resonance imaging of the optic nerve at 3.0 tesla.* Investigative radiology, 2006. **41**(2): p. 83-86.

60. Hickman, S.J., *Optic nerve imaging in multiple sclerosis.* Journal of Neuroimaging, 2007. **17**(s1): p. 42S-45S.

61. Yiannakas, M.C., et al., *A method for measuring the cross sectional area of the anterior portion of the optic nerve in vivo using a fast 3D MRI sequence.* Journal of Magnetic Resonance Imaging, 2010. **31**(6): p. 1486-1491.

62. Frohman, E.M., et al., *Relationship of optic nerve and brain conventional and non-conventional MRI measures and retinal nerve fiber layer thickness, as assessed by OCT and GDx: a pilot study.* Journal of the neurological sciences, 2009. **282**(1): p. 96-105.

63. Lindner, T., et al., *High spatial resolution in vivo magnetic resonance imaging of the human eye, orbit, nervus opticus and optic nerve sheath at 7.0 Tesla.* Experimental eye research, 2014. **125**: p. 89-94.

64. Forsén, S. and R.A. Hoffman, *Study of moderately rapid chemical exchange reactions by means of nuclear magnetic double resonance.* The Journal of Chemical Physics, 1963. **39**(11): p. 2892-2901.

65. Wolff, S.D. and R.S. Balaban, *Magnetization transfer contrast (MTC) and tissue water proton relaxation in vivo.* Magnetic resonance in medicine, 1989. **10**(1): p. 135-144.

66. Henkelman, R., G. Stanisz, and S. Graham, *Magnetization transfer in MRI: a review.* NMR in Biomedicine, 2001. **14**(2): p. 57-64.

67. Dousset, V., et al., *Experimental allergic encephalomyelitis and multiple sclerosis: lesion characterization with magnetization transfer imaging.* Radiology, 1992. **182**(2): p. 483-491.

68. Barker, G., P. Tofts, and A. Gass, *An interleaved sequence for accurate and reproducible clinical measurement of magnetization transfer ratio.* Magnetic resonance imaging, 1996. **14**(4): p. 403-411.

69. Berry, I., et al., *A multicenter measurement of magnetization transfer ratio in normal white matter.* Journal of Magnetic Resonance Imaging, 1999. **9**(3): p. 441-446.

70. Gochberg, D.F., et al., *Quantitative imaging of magnetization transfer using multiple selective pulses.* Magnetic resonance in medicine, 1999. **41**(5): p. 1065-1072.

71. Sled, J.G. and G.B. Pike, *Quantitative imaging of magnetization transfer exchange and relaxation*

properties in vivo using MRI. Magnetic Resonance in Medicine, 2001. **46**(5): p. 923-931.

72. Balafar, M.A., et al., *Review of brain MRI image segmentation methods.* Artificial Intelligence Review, 2010. **33**(3): p. 261-274.
73. Iglesias, J.E. and M.R. Sabuncu, *Multi-Atlas Segmentation of Biomedical Images: A Survey*. arXiv preprint arXiv:1412.3421, 2014.
74. Barrett, W.A. and E.N. Mortensen, *Interactive live-wire boundary extraction.* Medical image analysis, 1997. **1**(4): p. 331-341.
75. Mortensen, E.N. and W.A. Barrett, *Interactive segmentation with intelligent scissors.* Graphical models and image processing, 1998. **60**(5): p. 349-384.
76. Bezdek, J.C., L. Hall, and L.P. Clarke, *Review of MR image segmentation techniques using pattern recognition.* Medical physics, 1992. **20**(4): p. 1033-1048.
77. Pal, N.R. and S.K. Pal, *A review on image segmentation techniques.* Pattern recognition, 1993. **26**(9): p. 1277-1294.
78. Van Leemput, K., et al., *Automated model-based tissue classification of MR images of the brain.* Medical Imaging, IEEE Transactions on, 1999. **18**(10): p. 897-908.
79. Pham, D.L., C. Xu, and J.L. Prince, *Current methods in medical image segmentation 1*. Annual review of biomedical engineering, 2000. **2**(1): p. 315-337.
80. Bertsekas, D.P., *Nonlinear programming*. 1999.
81. Nocedal, J. and S.J. Wright, *Conjugate gradient methods*. 2006: Springer.
82. Gill, P.E. and W. Murray, *Conjugate-Gradient Methods for Large-Scale Nonlinear Optimization*. 1979, DTIC Document.
83. Criminisi, A., et al., *Regression forests for efficient anatomy detection and localization in CT studies*, in *Medical Computer Vision. Recognition Techniques and Applications in Medical Imaging*. 2011, Springer. p. 106-117.
84. Lempitsky, V., et al., *Random forest classification for automatic delineation of myocardium in real-time 3D echocardiography*, in *Functional Imaging and Modeling of the Heart*. 2009, Springer. p.

447-456.

85. Breiman, L., et al., *Classification and regression trees*. 1984: CRC press.
86. Harrigan, R.L., et al., *Robust optic nerve segmentation on clinically acquired computed tomography.* Journal of Medical Imaging, 2014. **1**(3): p. 034006-034006.
87. Harrigan, R.L., et al., *Disambiguating the optic nerve from the surrounding cerebrospinal fluid: Application to MS‐related atrophy.* Magnetic Resonance in Medicine, 2015.
88. Harrigan, R.L., et al. *Constructing a statistical atlas of the radii of the optic nerve and cerebrospinal fluid sheath in young healthy adults*. in *SPIE Medical Imaging*. 2015. International Society for Optics and Photonics.
89. Harrigan, R.L., et al. *Short term reproducibility of a high contrast 3-D isotropic optic nerve imaging sequence in healthy controls*. in *SPIE Medical Imaging*. 2016. International Society for Optics and Photonics.
90. Harrigan, R.L., et al. *Improved Automatic Optic Nerve Radius Estimation from High Resolution MRI*. in *SPIE Medical Imaging*. 2017. Orlando, Florida: International Society for Optics and Photonics.
91. Harrigan, R.L., et al., *Quantitative Characterization of Optic Nerve Atrophy in Patients with Multiple Sclerosis.* Multiple Sclerosis, 2017. **Submitted**.
92. Yao, X., et al. *Structural-Functional Relationships Between Eye Orbital Imaging Biomarkers and Clinical Visual Assessments*. in *SPIE Medical Imaging*. 2017. Oralndo, FL.
93. Harrigan, R.L., et al., *Characterization of Short- and Long-Term Stability of Non-Invasive Optic Nerve Imaging.* NeuroImage, 2017. **Submitted**.
94. Chan, L.L., et al., *Graves ophthalmopathy: the bony orbit in optic neuropathy, its apical angular capacity, and impact on prediction of risk.* AJNR Am J Neuroradiol, 2009. **30**(3): p. 597-602.
95. Weis, E., et al., *Clinical and soft-tissue computed tomographic predictors of dysthyroid optic neuropathy: refinement of the constellation of findings at presentation.* Arch Ophthalmol, 2011.

129(10): p. 1332-6.

96. Bijlsma, W.R. and M.P. Mourits, *Radiologic measurement of extraocular muscle volumes in patients with Graves' orbitopathy: a review and guideline.* Orbit, 2006. **25**(2): p. 83-91.
97. Bekes, G., et al., *Geometrical model-based segmentation of the organs of sight on CT images.* Medical Physics, 2008. **35**: p. 735.
98. Warfield, S.K., K.H. Zou, and W.M. Wells, *Simultaneous truth and performance level estimation (STAPLE): an algorithm for the validation of image segmentation.* Medical Imaging, IEEE Transactions on, 2004. **23**(7): p. 903-921.
99. Noble, J.H. and B.M. Dawant, *An atlas-navigated optimal medial axis and deformable model algorithm (NOMAD) for the segmentation of the optic nerves and chiasm in MR and CT images.* Medical image analysis, 2011. **15**(6): p. 877-884.
100. Dice, L.R., *Measures of the Amount of Ecologic Association Between Species.* Ecology, 1945. **26**(3): p. 297–302.
101. D'Haese, P.-F.D., et al. *Automatic segmentation of brain structures for radiation therapy planning*. in *Medical Imaging 2003*. 2003. International Society for Optics and Photonics.
102. Gensheimer, M., et al. *Automatic delineation of the optic nerves and chiasm on CT images*. in *Medical Imaging*. 2007. International Society for Optics and Photonics.
103. Isambert, A., et al., *Evaluation of an atlas-based automatic segmentation software for the delineation of brain organs at risk in a radiation therapy clinical context.* Radiotherapy and oncology, 2008. **87**(1): p. 93-99.
104. Heckemann, R.A., et al., *Automatic anatomical brain MRI segmentation combining label propagation and decision fusion.* Neuroimage, 2006. **33**(1): p. 115-126.
105. Rohlfing, T., D.B. Russakoff, and C.R. Maurer, *Performance-based classifier combination in atlas-based image segmentation using expectation-maximization parameter estimation.* Medical Imaging, IEEE Transactions on, 2004. **23**(8): p. 983-994.
106. McAuliffe, M.J., et al. *Medical Image Processing, Analysis and Visualization in clinical research* in

14th IEEE Symposium on Computer-Based Medical Systems. 2001. Bethesda, MD, USA.

107. Ourselin, S., et al., *Reconstructing a 3D structure from serial histological sections.* Image and vision computing, 2001. **19**(1): p. 25-31.
108. Ourselin, S., R. Stefanescu, and X. Pennec, *Robust registration of multi-modal images: towards real-time clinical applications*, in *Medical Image Computing and Computer-Assisted Intervention—MICCAI 2002*. 2002, Springer. p. 140-147.
109. Ardekani, B.A., et al., *A fully automatic multimodality image registration algorithm.* Journal of computer assisted tomography, 1995. **19**(4): p. 615.
110. Avants, B.B., M. Grossman, and J.C. Gee, *Symmetric diffeomorphic image registration: Evaluating automated labeling of elderly and neurodegenerative cortex and frontal lobe*, in *Biomedical Image Registration*. 2006, Springer. p. 50-57.
111. Arno Klein, S.S.G., Brian Avants, B.T.T Yeo, Bruce Fischl, Babak Ardekani, James C. Gee, J.J. Mann, Ramin V. Parsey, *Evaluation of volume-based and surface-based brain image registration methods.* Neuroimage, 2010. **51**: p. 214-220.
112. Aljabar, P., et al., *Multi-atlas based segmentation of brain images: Atlas selection and its effect on accuracy*. Neuroimage, 2009. **46**(3): p. 726-738.
113. Sabuncu, M.R., et al., *A generative model for image segmentation based on label fusion.* Medical Imaging, IEEE Transactions on, 2010. **29**(10): p. 1714-1729.
114. Asman, A.J. and B.A. Landman, *Formulating Spatially Varying Performance in the Statistical Fusion Framework.* Medical Imaging, IEEE Transactions on, 2012. **31**(6): p. 1326-1336.
115. Huttenlocher, D.P., G.A. Klanderman, and W.J. Rucklidge, *Comparing images using the Hausdorff distance.* Pattern Analysis and Machine Intelligence, IEEE Transactions on, 1993. **15**(9): p. 850-863.
116. Li, B., F. Bryan, and B. Landman, *Next Generation of the JAVA Image Science Toolkit (JIST) Visualization and Validation.* InSight Journal, 2012(874).
117. Lucas, B.C., et al., *The Java Image Science Toolkit (JIST) for Rapid Prototyping and Publishing of*

Neuroimaging Software. Neuroinformatics, 2010. **8**(1): p. 5-17.

118. Marcus, D.S., et al., *XNAT: A Software Framework for Manging Neuroimaging Laboratory Data*, in *Organization of Human Brain Mapping*. 2005: Toronto, Ontario, Canada.
119. Turk, M. and A. Pentland, *Eigenfaces for recognition.* Journal of cognitive neuroscience, 1991. **3**(1): p. 71-86.
120. Lötjönen, J.M., et al., *Fast and robust multi-atlas segmentation of brain magnetic resonance images.* Neuroimage, 2010. **49**(3): p. 2352-2365.
121. Wang, H., et al., *A learning-based wrapper method to correct systematic errors in automatic image segmentation: Consistently improved performance in hippocampus, cortex and brain segmentation.* Neuroimage, 2011. **55**(3): p. 968-985.
122. Richa, C., *The Neuro-Ophthalmology Survival Guide.* Optometry-Journal of the American Optometric Association, 2010. **81**(9): p. 423-424.
123. Beck, R.W., et al., *A randomized, controlled trial of corticosteroids in the treatment of acute optic neuritis. The Optic Neuritis Study Group.* N Engl J Med, 1992. **326**(9): p. 581-8.
124. Minen, M.T. and S. Karceski, *Multiple sclerosis and disease-modifying therapies.* Neurology, 2011. **77**(4): p. e26.
125. Medeiros, F.A., et al., *Evaluation of retinal nerve fiber layer, optic nerve head, and macular thickness measurements for glaucoma detection using optical coherence tomography.* Am J Ophthalmol, 2005. **139**(1): p. 44-55.
126. Trip, S.A., et al., *Retinal nerve fiber layer axonal loss and visual dysfunction in optic neuritis.* Annals of neurology, 2005. **58**(3): p. 383-391.
127. Costello, F., et al., *Quantifying axonal loss after optic neuritis with optical coherence tomography.* Annals of neurology, 2006. **59**(6): p. 963-969.
128. Costello, F., *Evaluating the Use of Optical Coherence Tomography in Optic Neuritis.* Multiple Sclerosis International, 2011. **2011**.
129. Inglese, M., et al., *Irreversible disability and tissue loss in multiple sclerosis: a conventional and*

magnetization transfer magnetic resonance imaging study of the optic nerves. Arch Neurol, 2002. **59**(2): p. 250-5.

130. Shen, S., et al., *Normative measurements of the Chinese extraocular musculature by high-field magnetic resonance imaging.* Invest Ophthalmol Vis Sci, 2010. **51**(2): p. 631-6.
131. D'Haese, P.-F., et al. *Automatic segmentation of brain structures for radiation therapy planning*. in *SPIE Medical Imaging*. 2003.
132. Isambert, A., et al., *Evaluation of an atlas-based automatic segmentation software for the delineation of brain organs at risk in a radiation therapy clinical context.* Radiother Oncol, 2008. **87**(1): p. 93-9.
133. Bekes, G., et al., *Geometrical model-based segmentation of the organs of sight on CT images.* Med Phys, 2008. **35**(2): p. 735-43.
134. Steinborn, M., et al., *High resolution ultrasound and magnetic resonance imaging of the optic nerve and the optic nerve sheath: anatomic correlation and clinical importance.* Ultraschall in der Medizin-European Journal of Ultrasound, 2011. **32**(06): p. 608-613.
135. Yiannakas, M.C., et al., *MRI Acquisition and Analysis Protocol for In Vivo Intraorbital Optic Nerve Segmentation at 3T.* Investigative ophthalmology & visual science, 2013. **54**(6): p. 4235-4240.
136. Panda, S., et al. *Robust optic nerve segmentation on clinically acquired CT*. in *SPIE Medical Imaging*. 2014. International Society for Optics and Photonics.
137. Panda, S., et al., *Evaluation of multiatlas label fusion for in vivo magnetic resonance imaging orbital segmentation.* Journal of Medical Imaging, 2014. **1**(2): p. 024002-024002.
138. Cherry, S.R., J.A. Sorenson, and M.E. Phelps, *Physics in nuclear medicine*. 2012: Elsevier Health Sciences.
139. Gudbjartsson, H. and S. Patz, *The Rician distribution of noisy MRI data.* Magnetic Resonance in Medicine, 1995. **34**(6): p. 910-914.
140. Repka, M.X. and H.A. Quigley, *The effect of age on normal human optic nerve fiber number and diameter*. Ophthalmology, 1989. **96**(1): p. 26-32.

141. Newman, W., et al., *Measurement of optic nerve sheath diameter by ultrasound: a means of detecting acute raised intracranial pressure in hydrocephalus.* British journal of ophthalmology, 2002. **86**(10): p. 1109-1113.

142. Gerling, J., et al., *Diameter of the optic nerve in idiopathic optic neuritis and in anterior ischemic optic neuropathy.* International ophthalmology, 1997. **21**(3): p. 131-135.

143. Avants, B.B., et al., *A reproducible evaluation of ANTs similarity metric performance in brain image registration.* Neuroimage, 2011. **54**(3): p. 2033-2044.

144. Asman, A.J. and B.A. Landman, *Non-local statistical label fusion for multi-atlas segmentation.* Med Image Anal, 2013. **17**(2): p. 194-208.

145. Harrigan, R.L., et al., *Disambiguating the Optic Nerve from the Surrounding Cerebrospinal Fluid Sheath in MS-related Atrophy.* Magnetic Resonance in Medicine, 2014 in press.

146. Hickman, S., et al., *The optic nerve sheath on MRI in acute optic neuritis.* Neuroradiology, 2005. **47**(1): p. 51-55.

147. Geeraerts, T., et al., *Use of T2-weighted magnetic resonance imaging of the optic nerve sheath to detect raised intracranial pressure.* Critical Care, 2008. **12**(5): p. R114.

148. Wang, H., et al., *Multi-atlas segmentation with joint label fusion.* IEEE transactions on pattern analysis and machine intelligence, 2013. **35**(3): p. 611-623.

149. Johnson, B.M., M. Miao, and A.A. Sadun, *Age-related decline of human optic nerve axon populations.* Age, 1987. **10**(1): p. 5-9.

150. Mikelberg, F.S., et al., *The normal human optic nerve: axon count and axon diameter distribution.* Ophthalmology, 1989. **96**(9): p. 1325-1328.

151. Balazsi, A., et al., *The effect of age on the nerve fiber population of the human optic nerve.* American journal of ophthalmology, 1984. **97**(6): p. 760-766.

152. Bowd, C., et al., *Imaging of the optic disc and retinal nerve fiber layer: the effects of age, optic disc area, refractive error, and gender.* JOSA A, 2002. **19**(1): p. 197-207.

153. Moya, F.J., L. Brigatti, and J. Caprioli, *Effect of aging on optic nerve appearance: a longitudinal*

study. British journal of ophthalmology, 1999. **83**(5): p. 567-572.

154. Varma, R., et al., *Race-, age-, gender-, and refractive error—related differences in the normal optic disc.* Archives of Ophthalmology, 1994. **112**(8): p. 1068-1076.
155. Jonas, J.B., et al., *Human optic nerve fiber count and optic disc size.* Investigative ophthalmology & visual science, 1992. **33**(6): p. 2012-2018.
156. Gao, Y., et al., *Integration of XNAT/PACS, DICOM, and Research Software for Automated Multi-modal Image Analysis.* Proc SPIE, 2013. **8674**.
157. Schwartz, Y., et al., *PyXNAT: XNAT in Python.* Front Neuroinform, 2012. **6**: p. 12.
158. Harrigan, R.L., et al., *Vanderbilt University Institute of Imaging Science Center for Computational Imaging XNAT: A multimodal data archive and processing environment.* NeuroImage, 2016. **124**: p. 1097-1101.
159. Marcus, D.S., et al., *The Extensible Neuroimaging Archive Toolkit: an informatics platform for managing, exploring, and sharing neuroimaging data.* Neuroinformatics, 2007. **5**(1): p. 11-34.
160. Beck, R.W., et al., *A randomized, controlled trial of corticosteroids in the treatment of acute optic neuritis.* New England Journal of Medicine, 1992. **326**(9): p. 581-588.
161. Group, O.N.S., *Visual function 15 years after optic neuritis: a final follow-up report from the Optic Neuritis Treatment Trial.* Ophthalmology, 2008. **115**(6): p. 1079.
162. Abalo-Lojo, J.M., et al., *Retinal nerve fiber layer thickness, brain atrophy, and disability in multiple sclerosis patients.* Journal of Neuro-ophthalmology, 2014. **34**(1): p. 23-28.
163. Hickman, S., et al., *Serial magnetization transfer imaging in acute optic neuritis.* Brain, 2004. **127**(3): p. 692-700.
164. Lagreze, W.A., et al., *Retrobulbar optic nerve diameter measured by high-speed magnetic resonance imaging as a biomarker for axonal loss in glaucomatous optic atrophy.* Investigative ophthalmology & visual science, 2009. **50**(9): p. 4223-4228.
165. Lenhart, P.D., et al., *The role of magnetic resonance imaging in diagnosing optic nerve hypoplasia.* American journal of ophthalmology, 2014. **158**(6): p. 1164-1171. e2.

166. Bilaniuk, L., et al., *Ocular and orbital lesions: surface coil MR imaging.* Radiology, 1985. **156**(3): p. 669-674.

167. Cummings, T.J., et al., *Gliomas of the optic nerve: histological, immunohistochemical (MIB-1 and p53), and MRI analysis.* Acta neuropathologica, 2000. **99**(5): p. 563-570.

168. Jack, C.R., et al., *The Alzheimer's disease neuroimaging initiative (ADNI): MRI methods.* Journal of magnetic resonance imaging, 2008. **27**(4): p. 685-691.

169. Marcus, D.S., et al., *Open Access Series of Imaging Studies (OASIS): cross-sectional MRI data in young, middle aged, nondemented, and demented older adults.* Journal of cognitive neuroscience, 2007. **19**(9): p. 1498-1507.

170. Poldrack, R.A., et al., *Toward open sharing of task-based fMRI data: the OpenfMRI project.* Frontiers in neuroinformatics, 2013. **7**: p. 12.

171. Labus, J.S., et al., *Pain and Interoception Imaging Network (PAIN): A multimodal, multisite, brain-imaging repository for chronic somatic and visceral pain disorders.* Neuroimage, 2016. **124**: p. 1232-1237.

172. Mugler, J.P. and J.R. Brookeman, *Three‐dimensional magnetization‐prepared rapid gradient‐echo imaging (3D MP RAGE).* Magnetic Resonance in Medicine, 1990. **15**(1): p. 152-157.

173. Hajnal, J.V., et al., *Use of fluid attenuated inversion recovery (FLAIR) pulse sequences in MRI of the brain.* Journal of computer assisted tomography, 1992. **16**(6): p. 841-844.

174. Schmierer, K., et al., *Magnetization transfer ratio and myelin in postmortem multiple sclerosis brain.* Annals of neurology, 2004. **56**(3): p. 407-415.

175. Smith, A.K., et al., *Incorporating dixon multi‐echo fat water separation for novel quantitative magnetization transfer of the human optic nerve in vivo.* Magnetic resonance in medicine, 2016.

176. Skinner, T.E. and G.H. Glover, *An extended two‐point dixon algorithm for calculating separate water, fat, and B0 images.* Magnetic resonance in medicine, 1997. **37**(4): p. 628-630.

177. Yarnykh, V.L., *Actual flip‐angle imaging in the pulsed steady state: a method for rapid three‐*

dimensional mapping of the transmitted radiofrequency field. Magnetic resonance in Medicine, 2007. **57**(1): p. 192-200.

178. Panda, S., et al., *Evaluation of Multi-Atlas Label Fusion for Orbital Segmentation on In Vivo MRI.* Journal of Medical Imaging, 2014.
179. Holmes, C.J., et al., *Enhancement of MR images using registration for signal averaging.* Journal of computer assisted tomography, 1998. **22**(2): p. 324-333.
180. Tustison, N.J., et al., *N4ITK: improved N3 bias correction.* IEEE transactions on medical imaging, 2010. **29**(6): p. 1310-1320.
181. Avants, B.B., N. Tustison, and G. Song, *Advanced normalization tools (ANTS).* Insight J, 2009. **2**: p. 1-35.
182. Avants, B.B., et al., *Symmetric diffeomorphic image registration with cross-correlation: evaluating automated labeling of elderly and neurodegenerative brain.* Medical image analysis, 2008. **12**(1): p. 26-41.
183. Asman, A.J. and B.A. Landman, *Formulating spatially varying performance in the statistical fusion framework.* IEEE transactions on medical imaging, 2012. **31**(6): p. 1326-1336.
184. Asman, A.J. and B.A. Landman, *Non-local statistical label fusion for multi-atlas segmentation.* Medical image analysis, 2013. **17**(2): p. 194-208.
185. Freund, Y. and R.E. Schapire. *A desicion-theoretic generalization of on-line learning and an application to boosting.* in *European conference on computational learning theory*. 1995. Springer.
186. Klein, A., et al. *Open labels: online feedback for a public resource of manually labeled brain images*. in *16th Annual Meeting for the Organization of Human Brain Mapping*. 2010.
187. Lauzon, C.B., et al., *Assessment of bias in experimentally measured diffusion tensor imaging parameters using SIMEX.* Magnetic resonance in medicine, 2013. **69**(3): p. 891-902.
188. Lauzon, C.B. and B.A. Landman, *Correcting power and p-value calculations for bias in diffusion tensor imaging.* Magnetic resonance imaging, 2013. **31**(6): p. 857-864.
189. Papadakis, N.G., et al., *A measure of curve fitting error for noise filtering diffusion tensor MRI data.*

Journal of Magnetic Resonance, 2003. **164**(1): p. 1-9.

190. Whitcher, B., et al., *Using the wild bootstrap to quantify uncertainty in diffusion tensor imaging.* Human brain mapping, 2008. **29**(3): p. 346-362.
191. Lang, A., et al., *Retinal layer segmentation of macular OCT images using boundary classification.* Biomedical optics express, 2013. **4**(7): p. 1133-1152.
192. Group, E.T.D.R.S.R., *Photocoagulation for diabetic macular edema. Early Treatment Diabetic Retinopathy Study report number 1.* Arch ophthalmol, 1985. **103**: p. 1796-1806.
193. Szucs-Farkas, Z., et al., *Using morphologic parameters of extraocular muscles for diagnosis and follow-up of Graves' ophthalmopathy: diameters, areas, or volumes?* AJR. American journal of roentgenology, 2002. **179**(4): p. 1005-1010.
194. Tian, S., et al., *MRI measurements of normal extraocular muscles and other orbital structures.* Graefe's Archive for Clinical and Experimental Ophthalmology, 2000. **238**(5): p. 393-404.
195. Pearce, E. and H. Bridge, *Is orbital volume associated with eyeball and visual cortex volume in humans?* Annals of Human Biology, 2013. **40**(6): p. 531-540.
196. Weis, E., et al., *Quantitative Computed Tomographic Predictors of Compressive Optic Neuropathy in Patients with Thyroid Orbitopathy: A Volumetric Analysis.* Ophthalmology, 2012. **119**(10): p. 2174-2178.
197. Rubin, P.A.D., et al., *Orbital computed tomographic characteristics of globe subluxation in thyroid orbitopathy.* Ophthalmology, 1998. **105**(11): p. 2061-2064.
198. Peyster, R.G., et al., *High-resolution CT of lesions of the optic nerve.* AJR. American journal of roentgenology, 1983. **140**(5): p. 869-874.
199. Monteiro, M.L.R., et al., *Diagnostic ability of barrett's index to detect dysthyroid optic neuropathy using multidetector computed tomography.* Clinics, 2008. **63**: p. 301-306.
200. Gonçalves, A.C.P., et al., *Quantification of orbital apex crowding for screening of dysthyroid optic neuropathy using multidetector CT.* AJNR. American journal of neuroradiology, 2012. **33**(8): p. 1602-1607.

201. Mossahebi, P., et al., *Removal of cerebrospinal fluid partial volume effects in quantitative magnetization transfer imaging using a three‐pool model with nonexchanging water component.* Magnetic Resonance in Medicine, 2014.

202. Yarnykh, V.L. and C. Yuan, *Cross-relaxation imaging reveals detailed anatomy of white matter fiber tracts in the human brain.* Neuroimage, 2004. **23**(1): p. 409-424.

203. Levesque, I.R., J.G. Sled, and G.B. Pike, *Iterative optimization method for design of quantitative magnetization transfer imaging experiments.* Magnetic resonance in medicine, 2011. **66**(3): p. 635-643.

204. Eich, G., G. Bodenhausen, and R. Ernst, *Exploring nuclear spin systems by relayed magnetization transfer.* J. Am. Chem. Soc.;(United States), 1982. **104**(13).

205. Yarnykh, V.L., *Pulsed Z‐spectroscopic imaging of cross‐relaxation parameters in tissues for human MRI: Theory and clinical applications.* Magnetic resonance in medicine, 2002. **47**(5): p. 929-939.

206. Quesson, B., et al., *Magnetization transfer imaging in vivo of the rat brain at 4.7 T: Interpretation using a binary spin‐bath model with a superlorentzian lineshape.* Magnetic resonance in medicine, 1997. **38**(6): p. 974-980.

207. Morrison, C. and R. Mark Henkelman, *A model for magnetization transfer in tissues.* Magnetic resonance in medicine, 1995. **33**(4): p. 475-482.

208. Li, J.G., S.J. Graham, and R.M. Henkelman, *A flexible magnetization transfer line shape derived from tissue experimental data.* Magnetic resonance in medicine, 1997. **37**(6): p. 866-871.

209. Listerud, J., *Off‐resonance pulsed magnetization transfer in clinical MR imaging: Optimization by an analysis of transients.* Magnetic resonance in medicine, 1997. **37**(5): p. 693-705.

210. Henkelman, R.M., et al., *Quantitative interpretation of magnetization transfer.* Magnetic resonance in medicine, 1993. **29**(6): p. 759-766.

211. Smith, A.K., et al., *Rapid, high-resolution quantitative magnetization transfer MRI of the human*

spinal cord. NeuroImage, 2014. **95**: p. 106-116.

212. Asman, A.J., et al., *Multi-atlas Learner Fusion: An efficient segmentation approach for large-scale data.* Medical Image Analysis, 2015. **26**(1): p. 82-91.